Computational Modeling of Cardiac Hypertrophy, Injury, and Therapy

A Dissertation

Presented to
the faculty of the School of Engineering and Applied Science
University of Virginia

in partial fulfillment
of the requirements for the degree

Doctor of Philosophy

by

Ana Cristina Estrada Durán

May 2020

APPROVAL SHEET

This Dissertation
is submitted in partial fulfillment of the requirements
for the degree of
Doctor of Philosophy

Author Signature: Ana C. Estrada D

This Dissertation has been read and approved by the examining committee:

Advisor: Jeffrey Holmes, MD, PhD

Committee Member: Jeffrey Saucerman, PhD

Committee Member: Silvia Blemker, PhD

Committee Member: Zhen Yan, PhD

Committee Member: Matthew Wolf, MD, PhD

Committee Member: ______________________

Accepted for the School of Engineering and Applied Science:

Craig H. Benson, School of Engineering and Applied Science

May 2020

ABSTRACT

The heart is one of the greatest examples of engineering principles manifested in biology. Through coordinated electrical and mechanical signals, the heart continually pumps vital blood and nutrients to the entire body. However, the heart is susceptible to injury through disruptions of its own blood supply, which causes myocardial infarction, and through severe alterations of hemodynamics, such as hypertension and aortic stenosis, among other perturbations. These conditions can lead to a progressive deterioration of cardiac function and overall increased demand on the heart to pump sufficient blood. The heart can compensate for the effects of injury through a process of growth and remodeling, which can cause cardiac muscle hypertrophy as an adaptation to increase pump function and efficiency. However, hypertrophy can also become maladaptive in the long term and contribute to the development of heart failure.

Cardiovascular disease (CVD), which encompasses the initial perturbations and eventual heart failure, is a critical health problem, responsible for the majority of all deaths worldwide. Given current trends of increasing incidence of CVD, it is imperative to develop and optimize new therapies to treat CVD. For this purpose, computational modeling offers the unique advantage of allowing us to not only better understand disease, from the effects of acute injury to the development of subsequent hypertrophy, but to also test and design different therapeutic approaches for treating CVD. The overall objective of my work, presented in this dissertation, has been to create computational models of the heart that can help us better understand how different manifestations of CVD affect the heart and how various therapies can lead to improvements in cardiac function and attenuation of the long-term effects of hypertrophy. I have focused on two specific projects: 1) constructing a finite-element model of local, anisotropic mechanical reinforcement of acute myocardial infarction, to understand how this therapy leads to increased pump function by altering mechanics; and 2) constructing a multiscale computational model of cardiac concentric hypertrophy – as is caused by hypertension and aortic stenosis – that incorporates realistic organ-level mechanics and intracellular signaling and captures how changes to both the mechanical and hormonal environments can induce growth and how specific genetic and pharmacologic interventions can attenuate this hypertrophy.

TABLE OF CONTENTS

CHAPTER 1

CHAPTER 2

CHAPTER 3

CHAPTER 4

ACKNOWLEDGEMENTS

My dissertation has been a journey of growth for me as a scientist, engineer, teacher, and person. My interest in biomedical engineering began with my love of math and fascination with physiology, and I am so thankful that it led me to the world of biomechanics. The past few years have been an opportunity to not only work on really interesting problems but also to push myself to do things I never thought possible – like learning C++. I have many people to thank for their support, encouragement, and mentorship throughout this entire process.

First, I must thank Dr. Jeff Holmes, my thesis advisor, for his mentorship and guidance over the past few years. Not only have you taught me so much about cardiac mechanics and physiology, but you have believed in my potential to do computational work, even when I didn't believe it myself. Without working with you, I may never have discovered how much I enjoy continuum mechanics or how approachable coding can really be. Thanks to your support, I have been able to work on fascinating science and develop models that I thought were completely beyond my reach. Working with you has been an incredible experience, and I am so thankful to have had the opportunity.

Next, I would like to thank my thesis committee: Dr. Jeff Saucerman, thank you for being a great chair and teaching me about network modeling. I have really enjoyed collaborating with you and learning from you. Dr. Silvia Salinas Blemker, thank you for encouraging me to try out computational modeling – your reassurance was a major reason why I came to UVA. I really appreciate being able to talk about our mutual love of math and mechanics. You have been a great role model and mentor, and I have especially appreciated the opportunity to have worked with you on the faculty search committee. Dr. Zhen Yan, your enthusiasm for science is contagious and has inspired me to continue asking questions and to find new ways to understand science. Dr. Matt Wolf, your positivity and appreciation for my projects have made me feel like my work really is worthwhile, even when I have had doubts. Thank you all for your guidance throughout my PhD journey and your continued enthusiasm about my work. It's been a real pleasure having such a supportive committee – you have made the entire process much less scary than it could have been. I have really enjoyed my conversations with each of you, and it has been so encouraging to see you be excited about my work. It has made me feel like I can succeed.

I would like to thank Dr. Brian Helmke for being an amazing mentor in my teaching endeavors. You have helped me learn so much about being a thoughtful and dedicated teacher and about designing classes truly focused on the students' learning. Thank you for your patience and constructive feedback throughout my attempts at leading lectures and writing problems, for being my mentor in the Tomorrow's Professor Today program, for all your advice on life and running, and for always believing in me. Thank you also to my friend and teaching mentor Dr. Lindsey Brinton, for encouraging me to be involved in engineering education and for always being a positive role model.

Thank you to all my mentors and colleagues who have helped me learn and troubleshoot along the way, and without whom my PhD journey would have been so much more difficult: Dr. Kyoko Yoshida, my mentor and friend, you inspire me to pursue science and have been invaluable in helping me run FEBio models. Thanks to Dr. Steve Maas, from the SCI Institute at the University of Utah, for all his patience and dedicated help as I learned how to write FEBio plugins. I also want to thank my mentors from my undergraduate days at Rice

University, especially Dr. Jane Grande-Allen and Dr. Ann Saterbak, for introducing me to the field of biomedical engineering and biomechanics, and Dr. Anthony Varilly-Alvarado, who encouraged me to take more math classes and continues to cheer me on in my science endeavors.

I want to thank all the wonderful people who have made my time at UVA and in Charlottesville so enjoyable, particularly through sports, trivia, and volunteering. Thank you to my lab mates in the Cardiac Biomechanics Group, especially to TK Phung and Derek Bivona. The two of you have made every day in lab so much happier with your laughter and shenanigans. Thank you to my former mentees for helping me learn to be a better mentor, especially Devrick Thomas, whose cheerfulness in lab was so contagious that I couldn’t help but be happy around him. Thank you for all my friends in the BME department and in the Raven Society for the community you have given me at UVA. A very special thank you goes to Christopher Waters. Your kindness and endless positivity have helped through my most difficult days and have made the good days better. Thank you for believing in me even when I don’t think anyone can.

Finally and most importantly, thank you to my family for your continued love, support, and encouragement throughout my entire life. To my parents, Ricardo Estrada and Ana Lía Durán, thank you for always being my biggest fans, for instilling in me a love and appreciation for math from the moment I could begin to understand numbers, and for teaching me to always be kind. Thank you to my brothers, Tomás and Rolando, for being so supportive and caring and for teaching me to never stop learning and to always strive to be my best. Thank you to my aunts Aurora and Cecilia, who are always cheering me on and sending love from Costa Rica; and to my aunts Rosy and Cristina, even though you are not with us anymore, I know that you would be so proud of me right now.

Lastly, to my dear niece Melissa, I hope that one day you might read this dissertation and think that biomechanics is the coolest and most amazing thing, just as I do.

And as we say in Costa Rica: ¡Pura vida! ¡Sí se pudo!

LIST OF FIGURES

LIST OF TABLES

CHAPTER 1:

INTRODUCTION

PHYSIOLOGY OF THE HEART

The heart is the engine of the body. It pumps life-sustaining blood, full of oxygen and nutrients, to the entire body through precisely coordinated mechanical and electrical signals. The heart is simultaneously simple and beautifully complex in its function as a biological pump, and it is the quintessential example of the interplay between engineering and biology. There are four chambers in the heart: the right and left atria, which receive blood from the body and the lungs, respectively; and the right and left ventricles, which pump blood to the lungs and the body, respectively. Deoxygenated blood from the body enters the right atrium, passes to the right ventricle through the tricuspid valve, and is then pumped through the pulmonary valve into the lungs for oxygenation. The newly oxygenated blood then flows into the left atrium, which pumps it into the left ventricle through the mitral valve. When the mitral valve closes, the left ventricle contracts and generates enough pressure to open the aortic valve and pump the oxygenated blood to the rest of the body; afterwards, the muscle relaxes so that the ventricle can fill again, completing a full cardiac cycle. The cardiac cycle includes two main phases: diastole, or relaxation and filling; and systole, the contraction of the heart and ejection of blood. End diastole corresponds to the closing of the mitral valve and maximum filling of the left ventricle. End systole occurs at the end of ejection, when the aortic valve closes. Blood flow into each chamber is controlled by the pressure gradient across each valve, which is, in turn, controlled by the contraction and relaxation of the cardiac muscle fibers in each chamber and by coupling to the circulatory system. The overall function of the heart can thus be described by tracking the pressure-volume behavior throughout a cardiac cycle, similar to how the performance of an engine is represented in thermodynamics.

The heart is composed primarily of myocardium, cardiac muscle fibers composed of cells called cardiomyocytes, but also includes collagen-rich extra-cellular matrix, which gives structure and support to the myocardium, and a dense network of coronary blood vessels responsible for supplying oxygen and nutrients to the highly metabolically demanding myocardium. The cardiomyocytes that constitute cardiac muscle fibers are striated muscle cells containing repeating contractile units called sarcomeres. These sarcomeres, in turn, contain thin actin filaments that overlap the ends of central, thick myosin filaments with protruding myosin heads that form cross bridges by binding to actin. Contraction of a sarcomere occurs when an adenosine triphosphate (ATP) molecule bound to a cross bridge is cleaved into an adenosine diphosphate (ADP) molecule and a phosphate ion (Pi) and the myosin head of the cross bridge binds to the actin thin filament. The cross bridge is then dephosphorylated, meaning it loses the Pi, and undergoes a conformational change that pulls the actin filament towards the center of the sarcomere. The ADP is then released, allowing for a new ATP to bind to the myosin head and release the actin filament. The force generated by this contraction depends on the length of the sarcomere and how far apart the actin filaments, on either side of the myosin filament, are from each other. Longer sarcomeres are able to contract more and generate more force. At a macroscopic level, this translates to greater force of muscle fiber contraction and cardiac pumping when the fibers are stretched more, such as when a greater volume of blood enters the heart; this behavior is the primary contributor of the Frank-Starling mechanism and serves as a way for the heart to adapt to increases in hemodynamic load.

Sarcomere contraction is triggered by excitation from an action potential, a behavior known as excitation-contraction coupling. Action potentials travel rapidly through the heart via a system of conductive Purkinje fibers that excite the cardiomyocytes at specific locations, and then more slowly through the cardiomyocytes via gap junctions that connect each of the cells together. The initial excitation occurs in the atria and then travels to the ventricles in a coordinated fashion, allowing for the rhythmic contraction of the heart. The action potentials themselves initiate an influx of calcium ions (Ca^{2+}) into the cell, which induce the subsequent release of a greater store of Ca^{2+} from the sarcoplasmic reticulum into the cytoplasm. Through their interaction with troponin and tropomyosin on actin filaments, Ca^{2+} ions are key for enabling the cross bridges to attach to actin filaments. In the relaxed state, tropomyosin covers the binding sites on actin filaments, preventing cross bridges from attaching. Tropomyosin is locked in place by troponin, but when Ca^{2+} ions bind to troponin, this causes the tropomyosin to move and reveal the binding sites for cross bridges. At the end of excitation, the Ca^{2+} ions are pumped back into the sarcoplasmic reticulum through specialized Ca^{2+} ion channels, which work through additional hydrolysis of ATP. Once the Ca^{2+} ions are depleted, troponin and tropomyosin return to their original conformations and the muscle relaxes. Thus, contraction and relaxation of cardiac muscle are coordinated through cycling of Ca^{2+} ions within the cardiomyocytes. Sarcomere length also impacts the calcium sensitivity and subsequent force generation of cardiomyocytes – longer sarcomeres are more sensitive – as an additional contributor of the Frank-Starling mechanism, described above.

The availability of ATP is necessary for contraction and relaxation, given this molecule's role in both cross bridge and Ca^{2+} ion cycling. ATP in the heart is generated mainly through the processes of fatty acid oxidation and glycolysis within the mitochondria of cardiomyocytes. The high metabolic demand of the heart requires a constant supply of sufficient oxygen and nutrient sources to operate properly. Any disruption in coronary blood flow or insufficient oxygen and nutrient availability can cause severe damage to the myocardium and reduce the contractile function of the heart.

The heart is part of the greater cardiovascular system, along with the network of blood vessels, and is therefore subject to changes in function in response to altered behavior in other parts of the system. Various signals, such as increased mechanical load or specific hormones, can directly or indirectly lead to adaptations in cardiomyocyte structure and function. For example, an acute drop in blood pressure can trigger reflex compensations that cause an increase in heart rate and contractility. A chronic increase in the resistance of the downstream arteries can cause the cardiomyocytes to grow in size and add more sarcomeres, allowing the heart to pump harder and keep up with the oxygen demand in the rest of the body. These compensations provide a way to maintain homeostasis in the presence of cardiovascular perturbations; however, there are many forms of cardiovascular disease that either disrupt these mechanisms or exhaust the ability of the heart to compensate. In the following section, we will discuss specific examples of cardiovascular disease and how we can study them to better understand how they affect the heart long-term.

Further detailed reading on heart physiology can be found in *Textbook of Medical Physiology* (11th Edition) by Arthur C. Guyton and John E. Hall [1]; and *Human Physiology* (12th Edition) by Stuart Ira Fox [2].

CARDIOVASCULAR DISEASE

Cardiovascular disease (CVD) is a critical health issue worldwide and is responsible for the majority of deaths in the United States. CVD encompasses a wide range of diseases affecting the cardiovascular system, ranging from acute myocardial infarction (MI) and stroke to chronic diseases such as hypertension, atherosclerosis, and valve disease. Over one third of adults in the United States currently suffer from a form of CVD, and over 130 million US adults are expected to suffer from at least one form of CVD by 2035. CVD is associated with a number of co-morbidities, including higher incidence of diabetes, obesity, and metabolic syndrome, which are also influenced by socioeconomic status. These co-morbidities further increase the likelihood of mortality and lead to a decrease in the quality of life of the individuals [3]. Given the current trends, it is imperative to develop and optimize new therapies for the treatment of CVD. This work aims to advance the use of computational modeling to better understand how the heart responds to different manifestations of CVD and how different therapies can support the heart and reduce the effect of CVD in long-term cardiac adaptation, particularly in growth and remodeling.

Growth and Remodeling in Soft Tissues

A common consequence of CVD is the development of cardiac hypertrophy, or an increase in cardiac mass, through a process of growth and remodeling (G&R). While present in pathology, G&R is universal in biology. In animals, G&R drives embryonic development and growth into adulthood. G&R is also responsible for structural adaptations, such as the growth of seashells and antlers [4], [5]. G&R also occurs at the tissue level in adults. For example, bones increase in thickness and density in response to increased mechanical loads. Similarly, soft tissues such as arteries and muscles demonstrate increases in mass in response to changes in hemodynamic and mechanical load [6]. The heart, in particular, responds to changes in mechanical load by increasing the mass of cardiomyocytes and adding sarcomeres, but without the proliferation of cardiomyocytes. Hypertrophy, the process of increasing mass through growth of already existing structures, is distinct from hyperplasia, an increase in mass through addition of new cells that occurs in the heart only during development. Cardiac hypertrophy takes two main forms: eccentric hypertrophy, which is characterized by addition of sarcomeres in series and subsequent lengthening of the muscle fibers; and concentric hypertrophy, characterized by addition of sarcomeres in parallel and an overall thickening of the myocardial walls [7], [8]. These two forms of hypertrophy manifest themselves as a result of different pathological insults. Eccentric hypertrophy is associated with volume overload of the heart, which can happen due to mitral regurgitation or after a myocardial infarction. Concentric hypertrophy instead occurs due to pressure overload, which can arise due increased resistance downstream of the left ventricle, such as hypertension or aortic stenosis. Examples of how some of these pathologies lead to hypertrophy are given in the following sections.

Eccentric Hypertrophy Following Myocardial Infarction

Myocardial infarction is a growing health problem, with the incidence of MI exceeding 1 million people each year in the United States alone [3]. MI occurs when a portion of the heart is deprived of blood flow, causing the affected cardiomyocytes to quickly die. This is likely to occur after progression of coronary artery disease, which causes blockages in the coronary arteries that directly perfuse the myocardium. The loss of a region of myocardium leads to a decrease in pump function and cardiac output, which in turn causes the heart to compensate by increasing heart rate, contractility, and diastolic pressure and volume. After the MI, damaged cardiomyocytes are replaced with a stiff collagen scar, while the cardiomyocytes in undamaged, or remote, regions undergo G&R that leads to enlargement of the left ventricle via eccentric hypertrophy and increases the likelihood of heart failure. The eccentric hypertrophy causes a lengthening of individual myocytes and cavity volume increase, without significant changes to myocyte or heart wall thickness. Overall, MI is the most common cause of heart failure, which now affects more than 5.1 million people in the United States and has a very poor prognosis [3], [9]–[11]. Thus, there is a need to develop better therapies to prevent post-infarction heart failure. Unfortunately, this effort remains hampered by an incomplete understanding of underlying mechanisms, and a lack of predictive models that can be used to design potential therapies to modulate post-infarction hypertrophy. However, it is clear that at least three important factors play a role: 1) neurohormonal stimulation helps preserve blood pressure and cardiac output immediately after infarction, but also drives adverse left-ventricular remodeling; 2) changes in mechanical environment directly stimulate eccentric hypertrophy in surviving myocardium; and 3) replacement of the damaged myocardium with a stiff collagen scar affects both beat-to-beat pump function and hypertrophy in the remote myocardium [12]–[21].

Experimental Models of Myocardial Infarction

Several *in vivo* experimental models exist for studying the effect of myocardial infarction and ischemia [12],[13], including large animal models, such as canines [24]–[26] and pigs [27]–[29], and small animal models, such as rats [30],[21] and mice [31],[32]. Broadly, these models can be classified in the following categories: 1) Ligation of coronary vessels; 2) Ablation; and 3) Ischemia-reperfusion. In the first type of model, a coronary artery is permanently ligated with a suture, cutting off blood flow to all muscle downstream of the ligation. The coronary artery of choice will yield infarction in different locations. For example, left anterior descending artery ligation will create a large anteroapical infarct, while ligating the left circumflex artery creates infarcts towards the later and posterior walls [33]. The severity of infarction depends on the extent of collateral vessels [34], adding potentially unwanted variability to these models. Ligation models have been used to understand disease progression into heart failure, the process of infarct healing, and the effectiveness of therapeutic interventions in preventing heart failure.

Another form of inducing MI is through ablation techniques, including cryoinfarction and thermal ablation [12],[21]. These techniques create an infarction by inducing an injury of predefined size and shape using liquid nitrogen or heated probes. Ablation techniques have the advantage of creating consistently reproducible infarcts across animals, unlike ligation methods. Additionally, they allow for studying the effects of infarcts in different regions of the heart. Controlling the infarct location yields insight into how the mechanical behavior of the heart will change in response to infarction and how infarct location influences scar structure during the healing [21].

Finally, ischemia-reperfusion (I/R) models are frequently used to mimic the damage seen in clinical settings where patients reach the hospital fairly quickly. When a patient suffers an acute MI, the first intervention is clearing the blockage and reperfusing the affected myocardium. While the initial ischemia initiates damage of the myocardium by disrupting blood flow, the reperfusion of the muscle can lead to substantial damage through myocardial stunning, adverse changes in cardiac metabolism, Ca^{2+} overload in the cardiomyocytes, and an increase in reactive oxygen species (ROS), all factors that contribute to cardiomyocyte injury and eventual necrosis [35]. I/R MI are often created by initial ligation of the coronary arteries to induce ischemia, followed by removal of the ligation to allow reperfusion, or by noninvasively using a balloon catheter to temporarily block a coronary artery. The time of occlusion determines whether the overall injury is mild and reversible or severe and permanent [22]. I/R MI models can be useful for understanding how therapeutic interventions may affect both the primary ischemic injury and the subsequent damage after reperfusion.

Mechanical Reinforcement Experimental Models

The characteristic mechanical disadvantage induced by MI suggests that mechanically supporting or reinforcing the heart could help improve cardiac function and/or remodeling post-MI. Based on this idea, a number of promising mechanical reinforcement interventions have been developed to slow or prevent eccentric hypertrophy and the progression from MI to heart failure. Mechanical reinforcement approaches include a wide range of strategies, including global restraint of the heart and local reinforcement of the infarct. Each of these approaches has advantages and limitations [36]. Global restraint methods have been shown to effectively reduce eccentric hypertrophy and improve heart failure outcomes without significant changes to LV function [36]–[42]. These methods also impair end-diastolic filling by restricting the size of the heart.

Local reinforcement methods aim at improving cardiac function and reducing eccentric hypertrophy by mechanically reinforcing only the affected infarct region. Numerous strategies have been used to for local reinforcement, from surgical reinforcement with synthetic meshes to injection and epicardial delivery of biomaterials [43]–[48]. However, the effectiveness of local reinforcement methods is highly variable. Given that only the infarcted region is reinforced, improvements in function and reductions in hypertrophy can depend on infarct location [49], [50] or scar remodeling [25], [26]. For example, Fomovsky et al. developed a promising method of local reinforcement using an anisotropic Dacron patch that markedly improved LV function acutely post-MI [25]. However, the functional improvement provided by the patch faded over time as scar remodeling led to compaction and unloading of the patch [26]. Optimizing local reinforcement approaches requires accounting for the impact of infarct reinforcement on remote region mechanics and scar remodeling as well as predicting the development of hypertrophy. Given these requirements, development of new local reinforcement strategies can be aided by computational modeling to predict the strategies' impact on the growth and remodeling of the heart and overall cardiac function.

Concentric Hypertrophy in Hypertension and Aortic Stenosis

Hypertension is an extremely prevalent condition, with over 85 million people living with this disease in the United States alone [3]. Hypertension refers to sustained elevated blood pressure and can be caused by a variety of circumstances, including diabetes, obesity, metabolic syndrome, excessive alcohol consumption, high salt intake, and genetic factors [51]. The recently updated American Heart Association guidelines categorize patients as hypertensive if they present with systolic blood pressure ≥ 130mmHg or diastolic blood pressure ≥ 80mmHg [52]. Hypertension develops over several decades and increases the risk of CVD, end-stage renal disease, and stroke, among other conditions [3]. One of the complications of hypertension is the chronic pressure overload experienced by the heart due to the increased downstream resistance in the arteries. Sustained pressure overload is known to induce concentric hypertrophy in the left ventricle, a thickening of the heart walls that is adaptive, in the sense that it increases the ability of the heart to generate pressure, but also carries long-term risks [53]. Left ventricular hypertrophy is further clinically associated with greater morbidity and mortality in hypertensive patients [54], [55], increasing the need for the development of therapies to prevent hypertension-induced hypertrophy.

Another example of increased afterload is aortic stenosis, a chronic condition where there is impaired ejection of blood from the left ventricle into the aorta. Aortic stenosis can occur due the aortic valves becoming calcified and stiff or due to congenital bicuspid aortic valve defects. In the United States, aortic stenosis affects an estimated 0.4% of the population, with calcific aortic stenosis present in nearly 3% of the population over the age of 75 [3]. As with hypertension, the increase in afterload caused by aortic stenosis can lead to concentric hypertrophy of the left ventricle. Aortic stenosis is treated through surgical repair or replacement of the stenotic valves, which can lead to improved cardiac function and even reversal of hypertrophy. However, the risk of surgical complications must be weighed against the potential for disease regression on a patient-by-patient basis [56]–[59]. For both hypertension and aortic stenosis, in order to improve treatment of the diseases, it is necessary to understand the mechanisms that drive concentric hypertrophy and to properly predict how different treatments will alter this pattern of growth in the heart.

Experimental Models of Pressure Overload

In vivo experimental models of pressure overload induced hypertrophy generally use constriction of the aorta to increase resistance to ejection of blood from the heart. The constriction can be created in a variety of ways, including banding using a metal clip [60]–[62] and surgical constriction using a suture [63], [64], commonly termed transverse aortic constriction (TAC). These pressure overload models have been used in both large animals, such as canines [60], [65]–[67], and small animals, such as rats or mice [61]–[64]. Of particular interest is TAC in mice, first validated by Rockman et al. (1991) [64]. TAC in mice serves as a particularly useful application of the technique, as it can be used to study pressure overload in genetically modified mice. The use of genetic modifications allows for overexpression or knock-out of genes that encode for different TAC-associated proteins, allowing for better understanding of the role of specific proteins and for testing of different therapeutic targets [68]–[73]. Aortic stenosis can be modeled experimentally by plication of the aortic valves [74] in order to prevent proper ejection. In general, these techniques are performed in young animals so that the banding and aortic valve stenosis will worsen as they age, mimicking the progression of disease in humans.

Other experimental approaches can be used to study hypertension more directly. The general methods for inducing hypertension can be classified in the following way: 1) genetically-modified animals; 2) pharmacological induction; 3) surgical interventions. An example of a genetically modified model is the spontaneously hypertensive rat (SHR), a mutant of the common Wistar rat that develops hypertension without additional external stimulation. Other models include the Dahl salt-sensitive rat, bred from Sprague-Dawley rats that developed hypertension under a high-salt diet, and transgenic models that specifically induce salt-sensitivity or hypertension directly. Examples of pharmacologically-induced hypertension include long-term infusion of angiotensin II, to overstimulate the renin-angiotensin system, and inhibition of nitric oxide, to increase the effect of vasoconstrictors. Finally, hypertension can be induced surgically by reducing renal blood flow [75]–[77].

COMPUTATIONAL MODELING FOR CARDIOVASCULAR DISEASE

Computational modeling is a particularly useful tool for understanding disease and developing new therapeutic strategies. By integrating experimental data and our understanding of physiology, computational models can bridge across scales and extend the number of hypotheses that we can feasibly generate and screen. Several groups have focused specifically on computational modeling for cardiac disease and have used models to aid in diagnosis, understand pathophysiology, and screen therapeutic approaches [78]–[80]. The level of complexity used in cardiac computational modeling varies depending on the problem being studied. At the simplest level, the heart can be modeled as a series of thin-walled compartments with specific volumes and pressures [81], which is particularly helpful for understand the function of the heart as a pump. Compartmental models have very fast computation times and also allow for the heart to be easily connected to a circulation model, so that changes in hemodynamics can be captured [82], [83]. A higher level of complexity can be obtained using thick-walled cylinders to simulate the heart [84], [85]. Cylinder models are useful for understanding the effect of transmural differences and for simulating active contraction in a simple fashion. Finite-element models again increase complexity but allow for greater spatial detail than the simple models. These models solve for the mechanics of individual elements, which can exhibit different material properties or sizes. Finite-element models are particularly useful when trying to understand how geometry and material heterogeneity impact cardiac function; for example, MI and local mechanical reinforcement can be simulated in finite-element models [78], [86], [87]. In Chapter 3 of this dissertation, we will discuss how a finite-element model of an average canine left ventricle was used to understand the acute improvement in function obtained with local, anisotropic reinforcement of an infarct.

Another especially promising use of computational models in biomechanics is simulating cardiac growth. This area has been advancing rapidly and is critical to developing therapies for modulating hypertrophy in CVD. The most common current approach – particularly in the heart – is to employ a phenomenological law that can predict the growth a particular tissue will undergo given specific mechanical inputs, such as stress or strain [85], [88]–[90]. The true growth stimulus remains a subject of debate, with laws proposed that depend either on stress or on strain at a particular point in the cardiac cycle. Most growth models for eccentric hypertrophy use a stimulus related to maximum fiber stretch, which occurs at or near end-diastole, while models of concentric hypertrophy tend to use fiber stress as the driver for growth [53]. One of the most promising growth laws was developed by Kerckhoffs et al. and is based on strain in the fiber and cross-fiber directions. This growth law successfully predicts patterns of hypertrophy in both pressure overload and volume overload [88]. However, these phenomenological growth laws depend solely on the mechanical environment of tissue and do not account for the effect of biochemical signals on hypertrophy. In the setting of CVD, mechanical perturbations are also accompanied by changes in hormonal signaling and inflammatory responses. Additionally, pharmacologic treatments for CVD also introduce changes in intracellular signaling. Modeling mechanics alone is clearly insufficient for predicting long-term hypertrophy in the presence of different drugs. Other modeling strategies exist to account for complex intracellular signaling. For example, a network model of intracellular hypertrophic signaling in cardiomyocytes was built by Ryall et al. [91], but this model does not account for tissue- or organ-level mechanical changes. In Chapter 4 of this dissertation, we will discuss a multiscale computational model of cardiac concentric hypertrophy that couples a cell-level signaling network model to a finite-element model of the left ventricle and is capable of predicting the effect of genetic and pharmacologic interventions for transverse aortic constriction.

REFERENCES

[1] A. C. Guyton and J. E. (John E. Hall, *Textbook of medical physiology*. Elsevier Saunders, 2006.

[2] S. I. Fox and McGraw-Hill Companies., *Human physiology*. McGraw-Hill, 2011.

[3] E. J. Benjamin *et al.*, *Heart Disease and Stroke Statistics—2018 Update: A Report From the American Heart Association*. 2018.

[4] R. Skalak, “Growth as A Finite Displacement Field,” in *Proceedings of the IUTAM Symposium on Finite Elasticity*, Dordrecht: Springer Netherlands, 1981, pp. 347–355.

[5] R. Skalak, G. Dasgupta, M. Moss, E. Otten, P. Dullemeijer, and H. Vilmann, “Analytical description of growth,” *J. Theor. Biol.*, vol. 94, no. 3, pp. 555–577, Feb. 1982.

[6] E. K. Rodriguez, a Hoger, and a D. McCulloch, “Stress-dependent finite-growth in soft elastic tissues,” *J. Biomech.*, vol. 27, no. 4, pp. 455–467, 1994.

[7] J. W. Holmes, “Candidate mechanical stimuli for hypertrophy during volume overload,” *J. Appl. Physiol.*, vol. 97, no. 4, pp. 1453–1460, Oct. 2004.

[8] J. Heineke and J. D. Molkentin, “Regulation of cardiac hypertrophy by intracellular signalling pathways,” *Nat. Rev. Mol. Cell Biol.*, vol. 7, no. 8, pp. 589–600, 2006.

[9] W. M. Smith, “Epidemiology of congestive heart failure,” *Am. J. Cardiol.*, vol. 55, no. 2, pp. A3–A8, Jan. 1985.

[10] W. B. Kannel and A. J. Belanger, “Epidemiology of heart failure,” *Am. Heart J.*, vol. 121, no. 3, pp. 951–957, Mar. 1991.

[11] M. Gheorghiade and R. O. Bonow, “Chronic heart failure in the United States: a manifestation of coronary artery disease.,” *Circulation*, vol. 97, no. 3, pp. 282–9, Jan. 1998.

[12] M. A. Pfeffer and E. Braunwald, “Ventricular Remodeling After Myocardial Infarction Experimental Observations and Clinical Implications,” *Circulation*, vol. 81, no. 4, pp. 1161–1172, 1990.

[13] P. Gaudron, C. Eilles, I. Kugler, and G. Ertl, “Progressive left ventricular dysfunction and remodeling after myocardial infarction. Potential mechanisms and early predictors.,” *Circulation*, vol. 87, no. 3, pp. 755–63, Mar. 1993.

[14] G. S. Francis and C. Chu, "Post-infarction myocardial remodelling: Why does it happen?," *Eur. Heart J.*, vol. 16, no. suppl N, pp. 31–36, Dec. 1995.

[15] J. N. Cohn, "Structural Basis for Heart Failure," *Circulation*, vol. 91, no. 10, pp. 2504–2507, May 1995.

[16] G. S. Francis and W. C. Carlyle, "Hypothetical pathways of cardiac myocyte hypertrophy: response to myocardial injury.," *Eur. Heart J.*, vol. 14 Suppl J, pp. 49–56, Nov. 1993.

[17] A. M. Gerdes *et al.*, "Structural remodeling of cardiac myocytes in patients with ischemic cardiomyopathy.," *Circulation*, vol. 86, no. 2, pp. 426–30, Aug. 1992.

[18] C. A. Beltrami *et al.*, "The cellular basis of dilated cardiomyopathy in humans.," *J. Mol. Cell. Cardiol.*, vol. 27, no. 1, pp. 291–305, Jan. 1995.

[19] A. J. Linzbach, "Heart failure from the point of view of quantitative anatomy∗," *Am. J. Cardiol.*, vol. 5, no. 3, pp. 370–382, Mar. 1960.

[20] P. A. Watson, "Mechanical activation of signaling pathways in the cardiovascular system," *Trends Cardiovasc. Med.*, vol. 6, no. 3, pp. 73–79, Apr. 1996.

[21] G. M. Fomovsky and J. W. Holmes, "Evolution of scar structure, mechanics, and ventricular function after myocardial infarction in the rat.," *Am. J. Physiol. Heart Circ. Physiol.*, vol. 298, pp. H221–H228, 2010.

[22] M. L. Lindsey *et al.*, "Guidelines for experimental models of myocardial ischemia and infarction," *Am. J. Physiol. Circ. Physiol.*, vol. 314, no. 4, pp. H812–H838, Apr. 2018.

[23] R. Klocke, W. Tian, M. Kuhlmann, and S. Nikol, "Surgical animal models of heart failure related to coronary heart disease," *Cardiovasc. Res.*, vol. 74, no. 1, pp. 29–38, Apr. 2007.

[24] W. B. Hood, B. McCarthy, and B. Lown, "Myocardial Infarction Following Coronary Ligation in Dogs," *Circ. Res.*, vol. 21, no. 2, pp. 191–200, Aug. 1967.

[25] G. M. Fomovsky, S. A. Clark, K. M. Parker, G. Ailawadi, and J. W. Holmes, "Anisotropic reinforcement of acute anteroapical infarcts improves pump function," *Circ. Hear. Fail.*, vol. 5, no. 4, pp. 515–522, 2012.

[26] S. A. Clarke, N. C. Goodman, G. Ailawadi, and J. W. Holmes, "Effect of Scar Compaction on the Therapeutic Efficacy of Anisotropic Reinforcement Following Myocardial Infarction in the Dog," *J. Cardiovasc. Transl. Res.*, vol.

8, no. 6, pp. 353–361, 2015.

[27] K. Iwanaga *et al.*, “Effects of G-CSF on cardiac remodeling after acute myocardial infarction in swine,” *Biochem. Biophys. Res. Commun.*, vol. 325, no. 4, pp. 1353–1359, Dec. 2004.

[28] J. W. Holmes, J. A. Nunez, and J. W. Covell, “Functional implications of myocardial scar structure,” *Am. J. Physiol. Circ. Physiol.*, vol. 272, no. 5, pp. H2123–H2130, May 1997.

[29] D. Lopez *et al.*, “Multiparametric CMR imaging of infarct remodeling in a percutaneous reperfused Yucatan mini-pig model,” *NMR Biomed.*, vol. 30, no. 5, p. e3693, May 2017.

[30] M. A. Pfeffer *et al.*, “Myocardial infarct size and ventricular function in rats.,” *Circ. Res.*, vol. 44, no. 4, pp. 503–12, Apr. 1979.

[31] X. M. Gao, A. M. Dart, E. Dewar, G. Jennings, and X. J. Du, “Serial echocardiographic assessment of left ventricular dimensions and function after myocardial infarction in mice.,” *Cardiovasc. Res.*, vol. 45, no. 2, pp. 330–8, Jan. 2000.

[32] E. Salimova *et al.*, “Variable outcomes of human heart attack recapitulated in genetically diverse mice.,” *NPJ Regen. Med.*, vol. 4, p. 5, 2019.

[33] L. C. Becker, E. H. Schuster, B. I. Jugdutt, G. M. Hutchins, and B. H. Bulkley, “Relationship between myocardial infarct size and occluded bed size in the dog: difference between left anterior descending and circumflex coronary artery occlusions.,” *Circulation*, vol. 67, no. 3, pp. 549–57, Mar. 1983.

[34] T. Miura, D. M. Yellon, D. J. Hearse, and J. M. Downey, “Determinants of infarct size during permanent occlusion of a coronary artery in the closed chest dog,” *J. Am. Coll. Cardiol.*, vol. 9, no. 3, pp. 647–654, Mar. 1987.

[35] A. Frank, M. Bonney, S. Bonney, L. Weitzel, M. Koeppen, and T. Eckle, “Myocardial ischemia reperfusion injury: from basic science to clinical bedside.,” *Semin. Cardiothorac. Vasc. Anesth.*, vol. 16, no. 3, pp. 123–32, Sep. 2012.

[36] S. A. Clarke, R. K. Ghanta, G. Ailawadi, and J. W. Holmes, “Cardiac Restraint and Support Following Myocardial Infarction,” Springer, Berlin, Heidelberg, 2013, pp. 169–206.

[37] M. C. Oz *et al.*, “Global surgical experience with the Acorn cardiac support device.,” *J. Thorac. Cardiovasc. Surg.*, vol. 126, no. 4, pp. 983–91, Oct. 2003.

[38] J. M. Power *et al.*, “Passive ventricular constraint amends the course of heart failure: a study in an ovine model of dilated cardiomyopathy.,” *Cardiovasc. Res.*, vol. 44, no. 3, pp. 549–55, Dec. 1999.

[39] P. A. Chaudhry *et al.*, “Passive epicardial containment prevents ventricular remodeling in heart failure.,” *Ann. Thorac. Surg.*, vol. 70, no. 4, pp. 1275–80, Oct. 2000.

[40] J. J. Pilla *et al.*, “Early Postinfarction Ventricular Restraint Improves Borderzone Wall Thickening Dynamics During Remodeling,” *Ann. Thorac. Surg.*, vol. 80, no. 6, pp. 2257–2262, Dec. 2005.

[41] A. S. Blom *et al.*, “Cardiac Support Device Modifies Left Ventricular Geometry and Myocardial Structure After Myocardial Infarction,” *Circulation*, vol. 112, no. 9, pp. 1274–1283, Aug. 2005.

[42] A. S. Blom *et al.*, “Ventricular Restraint Prevents Infarct Expansion and Improves Borderzone Function After Myocardial Infarction: A Study Using Magnetic Resonance Imaging, Three-Dimensional Surface Modeling, and Myocardial Tagging,” *Ann. Thorac. Surg.*, vol. 84, no. 6, pp. 2004–2010, Dec. 2007.

[43] J. L. Ifkovits *et al.*, “Injectable hydrogel properties influence infarct expansion and extent of postinfarction left ventricular remodeling in an ovine model,” *Proc. Natl. Acad. Sci.*, vol. 107, no. 25, pp. 11507–11512, 2010.

[44] R. Mukherjee *et al.*, “Targeted Myocardial Microinjections of a Biocomposite Material Reduces Infarct Expansion in Pigs,” *Ann. Thorac. Surg.*, vol. 86, no. 4, pp. 1268–1276, 2008.

[45] K. L. Fujimoto *et al.*, “Synthesis, characterization and therapeutic efficacy of a biodegradable, thermoresponsive hydrogel designed for application in chronic infarcted myocardium,” *Biomaterials*, vol. 30, no. 26, pp. 4357–4368, 2009.

[46] J. Leor *et al.*, “Intracoronary Injection of In Situ Forming Alginate Hydrogel Reverses Left Ventricular Remodeling After Myocardial Infarction in Swine,” *J. Am. Coll. Cardiol.*, vol. 54, no. 11, pp. 1014–1023, 2009.

[47] J. R. Garcia *et al.*, “A Minimally Invasive, Translational Method to Deliver Hydrogels to the Heart Through the Pericardial Space,” *JACC Basic to Transl. Sci.*, vol. 2, no. 5, pp. 601–609, 2017.

[48] W. Whyte *et al.*, “Sustained release of targeted cardiac therapy with a replenishable implanted epicardial reservoir,” *Nat. Biomed. Eng.*, vol. 2, no. 6, pp. 416–428, 2018.

[49] S. T. Kelley *et al.*, “Restraining infarct expansion preserves left ventricular geometry and function after acute anteroapical infarction.,” *Circulation*, vol. 99, no. 1, pp. 135–42.

[50] S. L. Moainie *et al.*, “Infarct restraint attenuates remodeling and reduces chronic ischemic mitral regurgitation after postero-lateral infarction.,” *Ann. Thorac. Surg.*, vol. 74, no. 2, pp. 444–9; discussion 449, Aug. 2002.

[51] O. A. Carretero and S. Oparil, “Essential Hypertension,” *Circulation*, vol. 101, no. 3, pp. 329–335, Jan. 2000.

[52] P. K. Whelton *et al.*, “2017 ACC/AHA/AAPA/ABC/ACPM/AGS/APhA/ASH/ASPC/NMA/PCNA Guideline for the Prevention, Detection, Evaluation, and Management of High Blood Pressure in Adults: Executive Summary: A Report of the American College of Cardiology/American Heart Association Task Force on Clinical Practice Guidelines,” *Hypertension*, vol. 71, no. 6, pp. 1269–1324, Jun. 2018.

[53] W. Grossman, D. Jones, and L. P. McLaurin, “Wall stress and patterns of hypertrophy in the human left ventricle,” *J. Clin. Invest.*, vol. 56, no. 1, pp. 56–64, 1975.

[54] R. M. Bruno and S. Taddei, “Renal denervation and regression of left ventricular hypertrophy,” *Eur. Heart J.*, vol. 35, no. 33, pp. 2205–2207, Sep. 2014.

[55] C. Cuspidi, A. Vaccarella, F. Negri, and C. Sala, “Resistant hypertension and left ventricular hypertrophy: an overview,” *J. Am. Soc. Hypertens.*, vol. 4, no. 6, pp. 319–324, Nov. 2010.

[56] E. S. Monrad, O. M. Hess, T. Murakami, H. Nonogi, W. J. Corin, and H. P. Krayenbuehl, “Time course of regression of left ventricular hypertrophy after aortic valve replacement.,” *Circulation*, vol. 77, no. 6, pp. 1345–55, Jun. 1988.

[57] S. Gelsomino *et al.*, “Time course of left ventricular remodeling after stentless aortic valve replacement,” *Am. Heart J.*, vol. 142, no. 3, pp. 556–562, 2001.

[58] C. M. Otto, “Valvular Aortic Stenosis. Disease Severity and Timing of Intervention,” *J. Am. Coll. Cardiol.*, vol. 47, no. 11, pp. 2141–2151, 2006.

[59] R. A. Nishimura *et al.*, “2014 AHA/ACC guideline for the management of patients with valvular heart disease: Executive summary: A report of the American college of cardiology/American heart association task force on

practice guidelines," *J. Am. Coll. Cardiol.*, vol. 63, no. 22, pp. 2438–2488, 2014.

[60] M. Koide *et al.*, "Premorbid determinants of left ventricular dysfunction in a novel model of gradually induced pressure overload in the adult canine.," *Circulation*, vol. 95, no. 6, pp. 1601–10, Mar. 1997.

[61] A. M. Feldman, E. O. Weinberg, P. E. Ray, and B. H. Lorell, "Selective changes in cardiac gene expression during compensated hypertrophy and the transition to cardiac decompensation in rats with chronic aortic banding.," *Circ. Res.*, vol. 73, no. 1, pp. 184–92, Jul. 1993.

[62] E. O. Weinberg *et al.*, "Angiotensin-converting enzyme inhibition prolongs survival and modifies the transition to heart failure in rats with pressure overload hypertrophy due to ascending aortic stenosis.," *Circulation*, vol. 90, no. 3, pp. 1410–1422, Sep. 1994.

[63] N. T. Songstad, D. Johansen, O.-J. How, P. I. Kaaresen, K. Ytrehus, and G. Acharya, "Effect of Transverse Aortic Constriction on Cardiac Structure, Function and Gene Expression in Pregnant Rats," *PLoS One*, vol. 9, no. 2, p. e89559, Feb. 2014.

[64] H. A. Rockman *et al.*, "Segregation of atrial-specific and inducible expression of an atrial natriuretic factor transgene in an in vivo murine model of cardiac hypertrophy.," *Proc. Natl. Acad. Sci.*, vol. 88, no. 18, pp. 8277–8281, Sep. 1991.

[65] W. H. Gaasch, M. R. Zile, P. K. Hoshino, E. O. Weinberg, D. R. Rhodes, and C. S. Apstein, "Tolerance of the hypertrophic heart to ischemia. Studies in compensated and failing dog hearts with pressure overload hypertrophy.," *Circulation*, vol. 81, no. 5, pp. 1644–53, May 1990.

[66] T. Nakamura, T. Nakajima, N. Suzuki, S. Arai, and N. Suwa, "Left Ventricular Stiffness and Chamber Geometry in the Pressure-Overloaded Hypertrophied Heart," *Tohoku J. Exp. Med.*, vol. 119, no. 3, pp. 245–256, Jul. 1976.

[67] S. Sasayama, J. Ross, D. Franklin, C. M. Bloor, S. Bishop, and R. B. Dilley, "Adaptations of the left ventricle to chronic pressure overload.," *Circ. Res.*, vol. 38, no. 3, pp. 172–178, Mar. 1976.

[68] S. A. Akhter, L. M. Luttrell, H. A. Rockman, G. Iaccarino, R. J. Lefkowitz, and W. J. Koch, "Targeting the receptor-G(q) interface to inhibit in vivo pressure overload myocardial hypertrophy," *Science (80-.).*, vol. 280, no. 5363, pp. 574–577, 1998.

[69] A. Rapacciuolo, G. Esposito, K. Caron, L. Mao, S. A. Thomas, and H. A. Rockman, “Important role of endogenous norepinephrine and epinephrine in the development of in vivo pressure-overload cardiac hypertrophy,” *J. Am. Coll. Cardiol.*, vol. 38, no. 3, pp. 876–882, 2001.

[70] H. A. Rockman, S. P. Wachhorst, L. Mao, and J. Ross, “ANG II receptor blockade prevents ventricular hypertrophy and ANF gene expression with pressure overload in mice.,” *Am. J. Physiol.*, vol. 266, no. 6 Pt 2, pp. H2468-75, Jun. 1994.

[71] L. Li *et al.*, “Comparison of angiotensin II type 1-receptor blockers to regress pressure overload-induced cardiac hypertrophy in mice,” *Hypertens. Res.*, vol. 33, no. 12, pp. 1289–1297, Dec. 2010.

[72] X. Wang *et al.*, “The effects of different angiotensin II type 1 receptor blockers on the regulation of the ACE-AngII-AT1 and ACE2-Ang(1–7)-Mas axes in pressure overload-induced cardiac remodeling in male mice,” *J. Mol. Cell. Cardiol.*, vol. 97, pp. 180–190, Aug. 2016.

[73] M. Patrizio *et al.*, “Propranolol causes a paradoxical enhancement of cardiomyocyte foetal gene response to hypertrophic stimuli,” *Br. J. Pharmacol.*, vol. 152, no. 2, pp. 216–222, 2007.

[74] A. Roitstein, B. V. Cheinberg, J. Kedem, J. Tse, H. R. Weiss, and P. M. Scholz, “Reduced effect of phenylephrine on regional myocardial function and O2 consumption in experimental LVH,” *Am. J. Physiol. Circ. Physiol.*, vol. 268, no. 3, pp. H1202–H1207, Mar. 1995.

[75] L. O. Lerman *et al.*, “Animal Models of Hypertension: A Scientific Statement From the American Heart Association,” *Hypertension*, vol. 73, no. 6, Jun. 2019.

[76] H. Y. Lin, Y. T. Lee, Y. W. Chan, and G. Tse, “Animal models for the study of primary and secondary hypertension in humans.,” *Biomed. reports*, vol. 5, no. 6, pp. 653–659, Dec. 2016.

[77] X.-F. Leong, C.-Y. Ng, and K. Jaarin, “Animal Models in Cardiovascular Research: Hypertension and Atherosclerosis,” *Biomed Res. Int.*, vol. 2015, pp. 1–11, May 2015.

[78] G. M. Fomovsky, J. R. MacAdangdang, G. Ailawadi, and J. W. Holmes, “Model-based design of mechanical therapies for myocardial infarction,” *J. Cardiovasc. Transl. Res.*, vol. 4, no. 1, pp. 82–91, 2011.

[79] T. K. N. Phung, C. B. Moyer, P. T. Norton, J. D. Ferguson, and J. W. Holmes, “Effect of ablation pattern on mechanical function in the atrium,”

PACE - Pacing Clin. Electrophysiol., vol. 40, no. 6, pp. 648–654, 2017.

[80] S. Zahid *et al.*, “Feasibility of using patient-specific models and the ‘minimum cut’ algorithm to predict optimal ablation targets for left atrial flutter,” *Hear. Rhythm*, vol. 13, no. 8, pp. 1687–1698, Aug. 2016.

[81] K. Sunagawa, W. L. Maughan, and K. Sagawa, “Effect of regional ischemia on the left ventricular end-systolic pressure-volume relationship of isolated canine hearts.,” *Circ. Res.*, vol. 52, no. 2, pp. 170–178, 1983.

[82] W. P. Santamore and D. Burkhoff, “Hemodynamic consequences of ventricular interaction as assessed by model analysis,” *Am. J. Physiol. Circ. Physiol.*, vol. 260, no. 1, pp. H146–H157, Jan. 1991.

[83] C. M. Witzenburg and J. W. Holmes, “Predicting the time course of ventricular dilation and thickening using a rapid compartmental model,” *J. Cardiovasc. Transl. Res.*, vol. 11, no. 2, pp. 109–122, 2018.

[84] J. M. Guccione, L. K. Waldman, and A. D. McCulloch, “Mechanics of Active Contraction in Cardiac Muscle: Part II—Cylindrical Models of the Systolic Left Ventricle,” *J. Biomech. Eng.*, vol. 115, no. 1, pp. 82–90, Feb. 1993.

[85] I. E. Lin and L. a Taber, “A model for stress-induced growth in the developing heart.,” *J. Biomech. Eng.*, vol. 117, no. 3, pp. 343–349, 1995.

[86] D. K. Bogen, S. A. Rabinowitz, A. Needleman, T. A. McMahon, and W. H. Abelmannj, “An analysis of the mechanical disadvantage of myocardial infarction in the canine left ventricle,” *Circ Res*, vol. 47, no. 5, pp. 728–741, 1980.

[87] S. T. Wall, J. C. Walker, K. E. Healy, M. B. Ratcliffe, and J. M. Guccione, “Theoretical impact of the injection of material into the myocardium: A finite element model simulation,” *Circulation*, vol. 114, no. 24, pp. 2627–2635, 2006.

[88] R. C. P. Kerckhoffs, J. H. Omens, and A. D. McCulloch, “A single strain-based growth law predicts concentric and eccentric cardiac growth during pressure and volume overload,” *Mech. Res. Commun.*, vol. 42, pp. 40–50, 2012.

[89] R. C. P. Kerckhoffs, “Computational modeling of cardiac growth in the post-natal rat with a strain-based growth law,” *J. Biomech.*, vol. 45, no. 5, pp. 865–871, 2012.

[90] S. Göktepe, O. J. Abilez, K. K. Parker, and E. Kuhl, “A multiscale model for

eccentric and concentric cardiac growth through sarcomerogenesis," *J. Theor. Biol.*, vol. 265, no. 3, pp. 433–442, 2010.

[91] K. A. Ryall, D. O. Holland, K. A. Delaney, M. J. Kraeutler, A. J. Parker, and J. J. Saucerman, "Network reconstruction and systems analysis of cardiac myocyte hypertrophy signaling.," *J. Biol. Chem.*, vol. 287, no. 50, pp. 42259–68, Dec. 2012.

CHAPTER 2:

CONTINUUM MECHANICS

AND FEBIO

CONTINUUM MECHANICS BASICS

In order to best describe the role of mechanics in computational modeling of the heart, we should first cover some of the basic principles of continuum mechanics that govern the mechanical behavior we study.

In Chapter 1, we discussed how the function of the heart can be studied by looking at the change in volumes at different pressures. We also learned that this function is also influenced by the amount of stretch individual fibers experience and the amount of force they can generate, termed the Frank-Starling mechanism. The force generated is of course critical for proper ejection, and it can help us understand how well the heart can pump in response to different conditions. While the force per fiber is useful, we can get a better idea of the function of the entire heart by tracking the stress and the strain experienced and generated by the muscle throughout the cardiac cycle. The stress-strain behavior can also be used to measure the amount of work per unit mass done by the heart, which correlates closely to oxygen consumption. We can calculate the stress-strain behavior of the heart by representing the myocardium as a continuum and then using finite-element analysis to solve for the mechanical behavior.

First, we should cover how stress and strain are related in a continuum mechanics context. Continuum mechanics is a representation that assumes materials behave as a continuum rather than as individual particles. The material is assumed to have uniform stress-strain behavior at a macroscale level. For example, the behavior of myocardium would be described as a single material rather than as a set of cardiomyocytes and collagen fibers, or even as the contribution of individual cross-bridges. For the purpose of this dissertation, we will describe myocardium as an anisotropic, hyperelastic material, the basic concepts of which we describe in the following section.

Deformation, strain, and stress

Mechanical behavior in continuum mechanics is described through specific tensors that describe how deforming a material will impact its stress response. As a first step, let's consider a body whose points correspond to the coordinates X = [X1 X2] in the coordinate basis e_1-e_2 (Figure 2.1). We now apply a deformation, **F**, to the body so that its new coordinates correspond to x = [x1 x2]. The new and original coordinates of the material points are related by a displacement u(X) (Equation 2.1). The deformation gradient **F** of the material is then defined according to Equation 2.2.

$$x = X + u(X) \tag{2.1}$$

$$\boldsymbol{F} = \frac{dx}{dX} = \frac{d\big(X + u(X)\big)}{dX} \tag{2.2}$$

The deformation tensor **F** can be used to define other characteristic tensors of materials, such as the right and left Cauchy-Green deformation tensors **C** and **B**, respectively (Equation 2.3). The Green-Lagrange strain tensor **E** can then be calculated from **C** and the identity tensor **I** (Equation 2.4).

$$\begin{gathered} \boldsymbol{C} = \boldsymbol{F}^T\boldsymbol{F} \\ \boldsymbol{B} = \boldsymbol{F}\boldsymbol{F}^T \end{gathered} \tag{2.3}$$

$$\boldsymbol{E} = \frac{1}{2}(\boldsymbol{C} - \boldsymbol{I}) \tag{2.4}$$

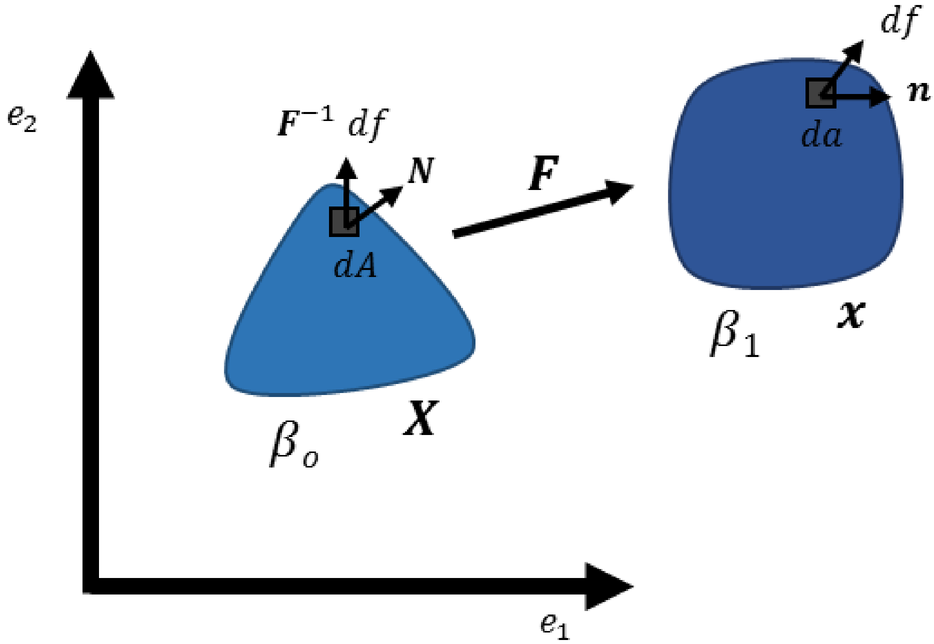

Figure 2.1 Deformation in body β_o, with coordinates **X**, into β_1, with coordinates **x**, due to deformation **F**. Tractions are obtained from force df acting on surface da with normal vector **n** in the deformed configuration and on surface dA with normal vector **N** in the undeformed configuration.

The Cauchy stress $\boldsymbol{\sigma}$ of a material is the force per deformed area of that material, and it defined based on the traction **t** experienced by the material on a surface with a normal vector **n** (Figure 2.1, Equation 2.5). The Cauchy stress depends on both the current traction in the deformed configuration and the deformed area, but additional stress tensors are used to describe stress in terms of the undeformed configuration. The first Piola-Kirchhoff stress is calculated from the current traction in the deformed configuration and the undeformed area (Equation 2.6). The second Piola-Kirchhoff stress is calculated from the traction if it was applied on the surface in the undeformed configuration (**t***) and the undeformed area (Equation 2.7). The deformation tensor **F** can be used to convert between these three stress tensors (Equation 2.8). In a generalized form of Hooke's law, the stress of linearly elastic materials can be defined as a function of the infinitesimal strain and a stiffness coefficient (Equation 2.9, 2.10). For myocardium, however, we will calculate stress assuming that it behaves as a hyperelastic material.

$$\boldsymbol{t} = \boldsymbol{\sigma} \cdot \boldsymbol{n} = \frac{df}{da} \tag{2.5}$$

$$\boldsymbol{t} = \boldsymbol{N} \cdot \boldsymbol{P} = \frac{df}{dA} \tag{2.6}$$

$$\boldsymbol{t}^{*} = \boldsymbol{N} \cdot \boldsymbol{S} = \frac{\boldsymbol{F}^{-1} df}{dA} \tag{2.7}$$

$$\boldsymbol{\sigma} = \frac{1}{J} \boldsymbol{F} \boldsymbol{P} = \frac{1}{J} \boldsymbol{F} \boldsymbol{S} \boldsymbol{F}^{T} \tag{2.8}$$

$$\sigma_{ij} = c_{ijkl} \varepsilon_{kl} \tag{2.9}$$

$$\boldsymbol{\varepsilon} = \frac{1}{2}(\boldsymbol{F} + \boldsymbol{F}^T) - \boldsymbol{I} \qquad (2.10)$$

A material is defined to be hyperelastic when its stress response due to a deformation is dependent only on its initial and final states. This is a special case of elasticity, which only depends on the current deformation to determine the stress response, and is distinct from viscoelasticity, where the stress response is time-dependent. For a hyperelastic material, the work done on the material is path-independent, only depending on the initial and final points, and can be described using a strain energy density function, a measure of the stored potential energy in the material (Equation 2.11).

$$W(\boldsymbol{F}(X), X) = \int_{t0}^{t} \boldsymbol{P}(\boldsymbol{F}(X), X) : \dot{\boldsymbol{F}} dt \qquad (2.11)$$

As a simple example, we can see how this principle applies to a spring. When a string is stretched, it gains potential energy proportional to the distance it is stretched. By Hooke's law, we know that the force required to stretch the spring a distance x is equal to kx, where k is the spring constant, or stiffness of the spring (Equation 2.12). This force is also the derivative of the potential energy of that spring (Equation 2.13). The potential energy is the strain energy function for the spring, and it helps us understand the relationship between force and strain energy. More generally, strain energy functions define the stiffness of the material, and their derivative with respect to strain corresponds to the stress response of that material.

$$force = kx = \frac{dU}{dx} \tag{2.12}$$

$$U = \frac{1}{2}kx^2 \tag{2.13}$$

The 2nd Piola-Kirchhoff stress of a hyperelastic material is defined as the derivative of the strain energy function W with respect to the Green-Lagrange strain **E**, or commonly with respect to the right Cauchy-Green deformation tensor **C,** as seen in Equation 2.14**.** From Equation 2.7, we then define the Cauchy stress for a hyperelastic material in Equation 2.15.

$$\boldsymbol{S} = \frac{dW}{d\boldsymbol{E}} = 2\frac{dW}{d\boldsymbol{C}} \tag{2.14}$$

$$\boldsymbol{\sigma} = \frac{2}{J}\boldsymbol{F}\frac{\partial W}{\partial \boldsymbol{C}}\boldsymbol{F}^T \tag{2.15}$$

Further reading on the concepts of continuum mechanics can be found in *Introduction to Continuum Mechanics* (4th Edition) by Lai, Rubin, and Krempl [1]; in *Continuum Mechanics* by A. J. M. Spencer [2]; and in the FEBio Theory Manual (version 2.7) (febio.org) [3].

FINITE ELEMENT MODELING OF THE HEART

The FEBio finite element suite

For all the simulations in this dissertation, we use the FEBio finite element software suite to run our models. FEBio is an open-source, nonlinear implicit finite element solver developed specifically for modeling the behavior of biological tissues. It can be used for both quasi-static and dynamic analysis in problems using structural mechanics, fluid mechanics, biphasic and multiphasic conditions, and heat transfer. The software suite includes a variety of nonlinear constitutive models designed to represent behavior under large deformations, as those expected in biological tissues. These models include classic isotropic models, such as the Neo-Hookean and Mooney-Rivlin materials, and a variety of transversely isotropic and orthotropic materials, such as the transversely isotropic Mooney-Rivlin material and Fung-type orthotropic material, which include prescribed fiber directions. Each of these materials is defined by a specific strain energy function, which then determines the stress response, as described in the previous section. FEBio solves for the deformation of each element during a simulation by minimizing the strain energy within each of the elements [3]. We chose to use the transversely isotropic Mooney-Rivlin material to capture the mechanical behavior of myocardium for all the models in this dissertation.

Transversely isotropic Mooney-Rivlin material

The transversely isotropic Mooney-Rivlin (TIMR) material is commonly used to represent the behavior of soft tissues with a preferred fiber direction. TIMR has an isotropic matrix term that follows the rubber-like Mooney-Rivlin behavior, an exponential fiber term, and a dilatational term to account for changes in volume. The isotropic term depends on invariants I_C and II_C of the right Cauchy-Green deformation tensor **C**, while the fiber term depends on invariant IV_C, corresponding to the fiber stretch squared, and the dilatational term depends on III_C, the determinant *J*. The TIMR strain energy function *W* and its derivatives with respect to the invariants of **C** are shown in Equation 2.16 [4]. Thus, the material coefficients C_1 and C_2 determine the isotropic stiffness, C_3 scales the fiber behavior, C_4 determines the curvature of the fiber behavior, and K corresponds to the bulk modulus. To further simplify the model, we often choose to set $C_2 = 0$ when simulating myocardium, reducing the isotropic contribution to that of a Neo-Hookean rather than Mooney-Rivlin material. An example of the uniaxial TIMR stress-strain behavior is shown in Figure 2.2.

$$W = C_1(I_C - 3) + C_2(II_C - 3) + \mathrm{F}\left(\sqrt{IV_C}\right) + \frac{K}{2}[\ln(J)]^2$$

$$\frac{\partial W}{\partial I_C} = C_1 \qquad \frac{\partial W}{\partial II_C} = C_2 \qquad \frac{\partial W}{\partial IV_C} = \frac{1}{\lambda_1}C_3\left(e^{C_4(\lambda_1 - 1)} - 1\right) \tag{2.16}$$

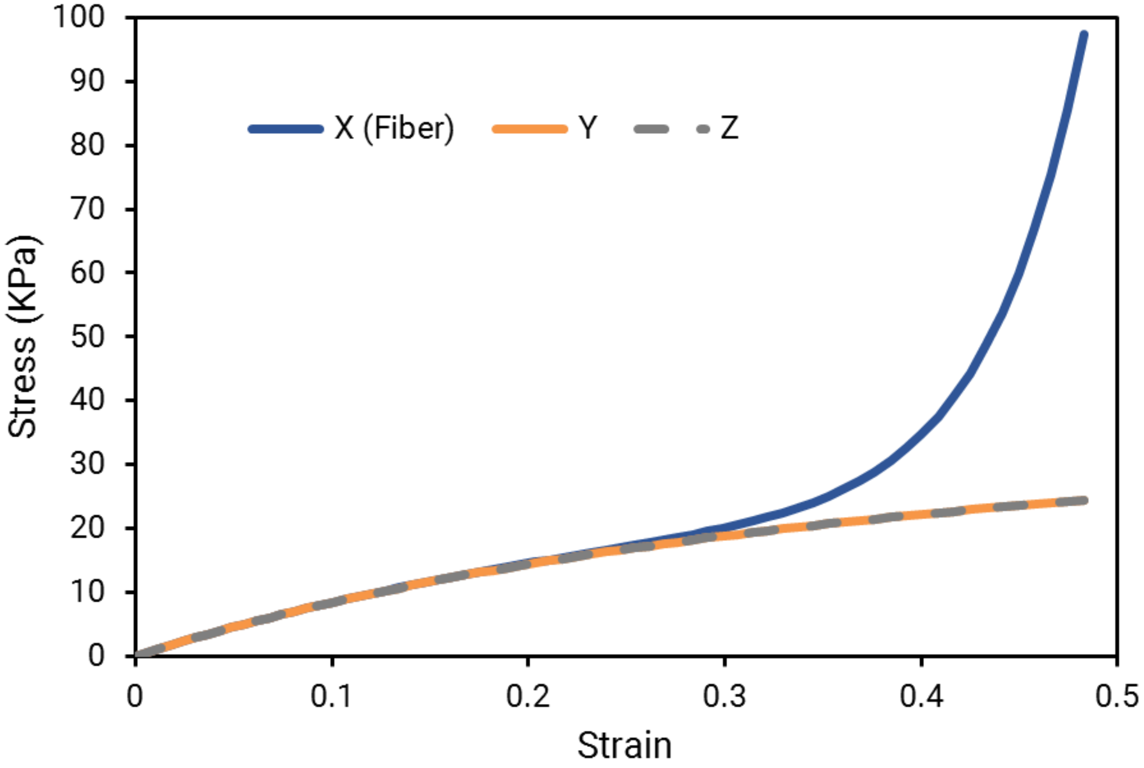

Figure 2.2 Stress-strain relationships in the fiber and transverse directions of the transversely isotropic Mooney-Rivlin material under uniaxial stretch along each direction. Fibers are oriented in the X direction (blue), which shows exponential behavior. The Y (orange) and Z (grey) directions correspond to the isotropic Mooney-Rivlin matrix.

Extending FEBio using custom-built plugins

The capabilities of FEBio can be extended through the use of custom-built plugins [5]. By writing plugins, users can implement new materials, outputs, or tasks, to name a few examples. The plugins are self-contained dynamic libraries, meaning that they can be compiled individually without the need to recompile a new version of FEBio in order to use them. Once compiled, a plugin can be loaded into FEBio at the beginning of a simulation. This aspect is particularly useful for sharing the plugins with the broader FEBio community. Detailed instructions for writing different types of plugins are found in the FEBio Developer's Manual [6].

FEBio and its plugins are written in C++, so we will give a brief overview of the structure of FEBio files and the method for writing a plugin. With C++ being an object-oriented programming language, the bulk of plugin development centers on writing new classes that inherit properties from the built-in FEBio classes. We will focus specifically on plugins that implement new material models; although, similar principles can be used to develop other capabilities. Each material in FEBio derives its general properties from a governing material type, such as a solid material, fluid, or a biphasic material; the governing material is then further subdivided based on specific properties, such as a material being an elastic solid. Hyperelastic materials, like TIMR, derive their general properties from the Elastic Material class and then define their strain energy functions in order to calculate stress. FEBio hyperelastic material files include user-defined parameters and two required functions: the Cauchy stress calculation and the spatial elasticity tensor, or tangent, calculation. They can also include calculations of the strain energy density, but these are not critical for solving a model. Creating a new material plugin thus requires identifying the general material from which properties are inherited, defining parameters, and writing the stress and tangent calculation functions. An example of a FEBio material file is shown in Figure 2.3.

FEBio plugins can be compiled for Linux, Mac OS, or Windows operating systems. The work shown here uses the Ubuntu 14.04 Linux build, FEBio version 2.6.4 Software Development Kit, and the g++ gnu compiler. The plugins can also be built using XCode for Mac OS and Visual Studio for Windows. The source code for each material does not change between operating systems, only the compiling method. Once compiled, the plugins are then available for any user within the specific operating system. Each version of the plugins has the following extensions once compiled: .so for Linux, .dylib for MacOS, and .dll for Windows. In the sections below, we will discuss two new material plugins: TIMR with force-velocity capabilities and TIMR with growth capabilities.

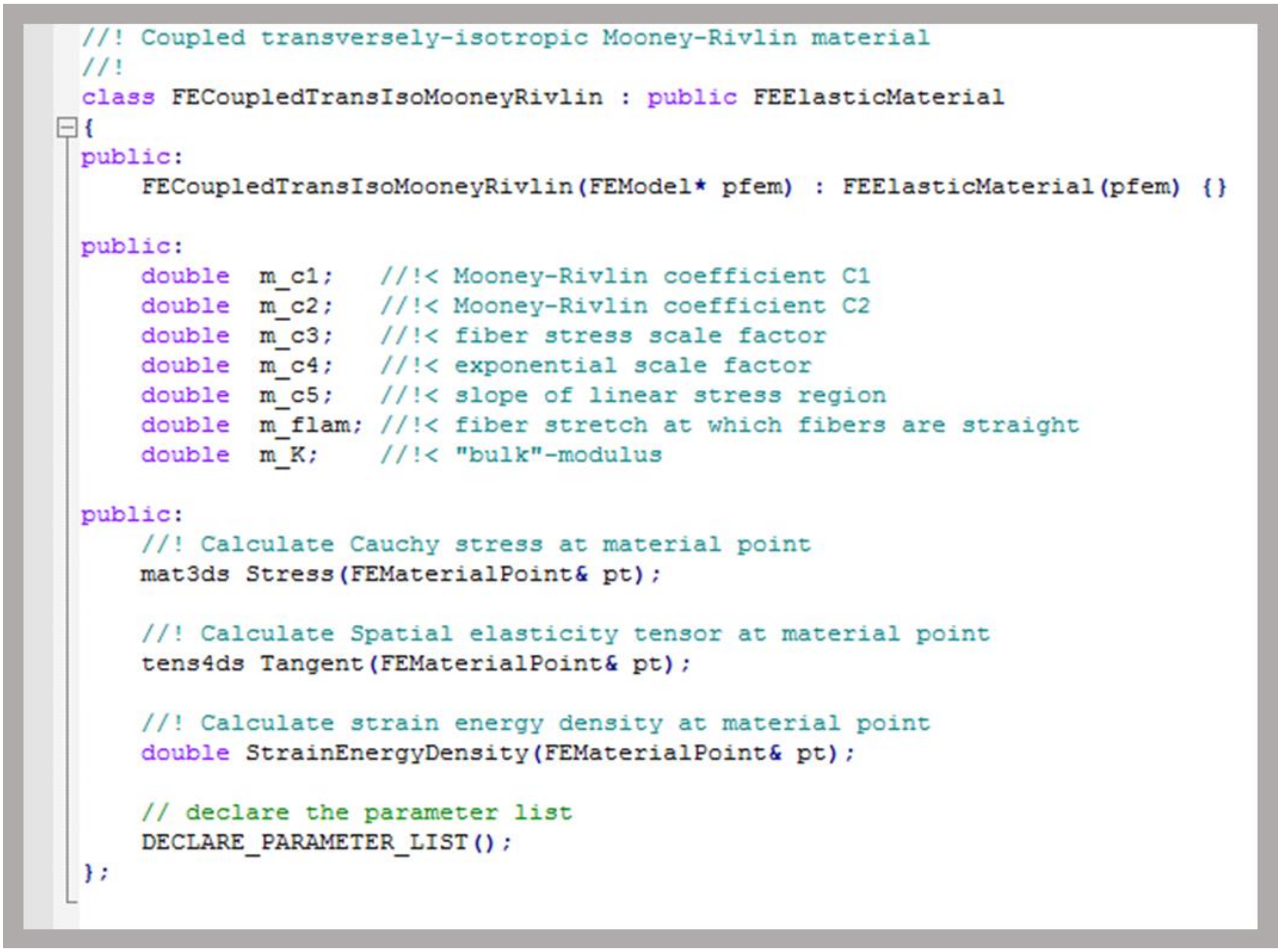

```
//! Coupled transversely-isotropic Mooney-Rivlin material
//!
class FECoupledTransIsoMooneyRivlin : public FEElasticMaterial
{
public:
    FECoupledTransIsoMooneyRivlin(FEModel* pfem) : FEElasticMaterial(pfem) {}

public:
    double  m_c1;   //!< Mooney-Rivlin coefficient C1
    double  m_c2;   //!< Mooney-Rivlin coefficient C2
    double  m_c3;   //!< fiber stress scale factor
    double  m_c4;   //!< exponential scale factor
    double  m_c5;   //!< slope of linear stress region
    double  m_flam; //!< fiber stretch at which fibers are straight
    double  m_K;    //!< "bulk"-modulus

public:
    //! Calculate Cauchy stress at material point
    mat3ds Stress(FEMaterialPoint& pt);

    //! Calculate Spatial elasticity tensor at material point
    tens4ds Tangent(FEMaterialPoint& pt);

    //! Calculate strain energy density at material point
    double StrainEnergyDensity(FEMaterialPoint& pt);

    // declare the parameter list
    DECLARE_PARAMETER_LIST();
};
```

Figure 2.3 Example header file for a material in FEBio. This file defines the key functions for the Cauchy stress and the spatial elasticity tensor (tangent), the input parameters, and the class from which the material derives its properties (FEElasticMaterial).

Force-velocity plugin

The transversely isotropic Mooney-Rivlin material in FEBio by default includes the capability of active contraction in the fiber direction. The active contraction model used in TIMR, first presented by Guccione et al. [7], calculates active tension, T, based on intracellular calcium cycling and the current length of a fiber (Equation 2.17), where: Ca_0 refers to the initial calcium concentration, $Ca_{0,max}$ refers to the maximum calcium concentration, T_{max} is the maximum isometric tension, β is the length-dependence coefficient, l_r is the sarcomere reference length, l_0 is the sarcomere unloaded length, λ is the fiber stretch, and e(t) is a time-varying normalized activation loadcurve that defines the time course of force generation throughout a simulation. The total fiber stress is then the sum of the passive stress from TIMR and the active tension (Equation 2.18).

$$T(t) = T_{max} \frac{Ca_o^2}{Ca_o^2 + ECa_{50}^2(t)} e(t)$$

$$ECa_{50}(t) = \frac{Ca_{o\,max}}{\sqrt{\exp(\beta(\lambda(t) l_r - l_o) - 1}} \tag{2.17}$$

$$\sigma_{fiber,\ total}\big(t, \lambda(t)\big) = \sigma_{fiber,passive}\big(\lambda(t)\big) + T\big(t, \lambda(t)\big) \tag{2.18}$$

While this length-dependent active contraction can serve as an approximation of myocardial behavior, it does not fully capture the muscle shortening mechanics that occur during muscle contraction. When contracting, muscles also exhibit a force-velocity relationship, described by Hill in 1938 [8] and further examined by Huxley in 1957 [9]. During isotonic contraction, the velocity of shortening is inversely proportional to the relative tension applied, with the maximum velocity V_{max} reached when unloaded and zero velocity at the maximum tension T_{max}. When taken together with the length-dependence of contraction, the force-velocity relationship serves as a dampening term for tension generated and is important for simulating the active contraction of myocardium during a cardiac cycle. Hunter, McCulloch, and ter Keurs [10] proposed a fading-memory formulation for the force-velocity relationship of muscle specifically for modeling the contraction of myocardium.

In order to better capture the active behavior of myocardium, we implemented a custom active contraction plugin that combines the length-dependent behavior currently used for TIMR in FEBio [4], [7] and a modified force-velocity relationship based on the fading-memory formulation [10]. The tension generated in our active contraction module (Equation 2.19) is now the product of three distinct components: the time-varying normalized activation, e(t), that defines the time course of force generation throughout the cardiac cycle; the instantaneous length-dependent term, from Equation 2.17, that scales the peak possible isometric tension based on the current fiber stretch; and a force-velocity term that dampens the instantaneous force generation based on the rate of shortening of the fibers. In Equation 2.19, the constant a is the force-velocity curvature parameter, A_1 is slow tension weighting coefficient, and α_1 is the slow tension recovery rate constant.

$$T\big(t,\lambda(t)\big) = e(t)\left[T_{max}\frac{Ca_o^2}{Ca_o^2 + ECa_{50}^2\big(\lambda(t)\big)}\right]\left[\frac{1 + aQ\big(t,\lambda(t)\big)}{1 - Q\big(t,\lambda(t)\big)}\right]$$

$$Q\big(t,\lambda(t)\big) = A_1\int_{-\infty}^{t} e^{-\alpha_1(t-\tau)}\dot{\lambda}(\tau)d\tau \qquad (2.19)$$

We implemented the time-dependent force-velocity relationship in FEBio by adapting a method used for modeling viscoelastic materials, namely introducing a stretch history term (Equation 2.20) to calculate the integral Q(t, λ(t)). In our force-velocity plugin, the material file defines an additional class specific to the force-velocity material and allows for a "force-velocity material point" to be created. This new material point stores the deformation information for the previous time step, as well as the values of the functions within the integral. Using these stored terms and accessing the time interval for each step, FEBio can then calculate the velocity of contraction during the simulation. The implementation also includes a flag to turn force-velocity on or off, allowing the user the option of using the same material with only the length-dependent active contraction term. In Figure 2.4A we show an example of the twitch response for an element at different velocities and then show the velocity-tension relationship using a single-element FE simulation with the plugin compared to the relationship reported by Huxley [9] in Figure 2.4B-C. Finally, Figure 2.5 shows the dampening of contraction that occurs when force-velocity is used compared to the default length-dependent active contraction model.

$$Q(t) = A_1 H_{ac}(t)$$

$$\begin{aligned} H_{ac}(t+\Delta t) &= \exp(-\Delta t \times \alpha_1)\, H_{ac}(t) \\ &\quad + \frac{1-\exp(-\Delta t \times \alpha_1)}{\Delta t \times \alpha_1}\big(\lambda(t+\mathit{\Delta} t) - \lambda(t)\big) \end{aligned} \tag{2.20}$$

In Chapter 3, we use the force-velocity plugin in a finite-element model of an average canine left ventricle. Because the model does not have valves, contraction is simulated by optimizing the e(t) loadcurve so that it completely offsets the increase in applied cavity pressure during the isovolumic phase and then leads to shortening during the ejection phase. The force-velocity relationship improves the stability of the model by dampening muscle shortening and allowing greater control of contraction during systole.

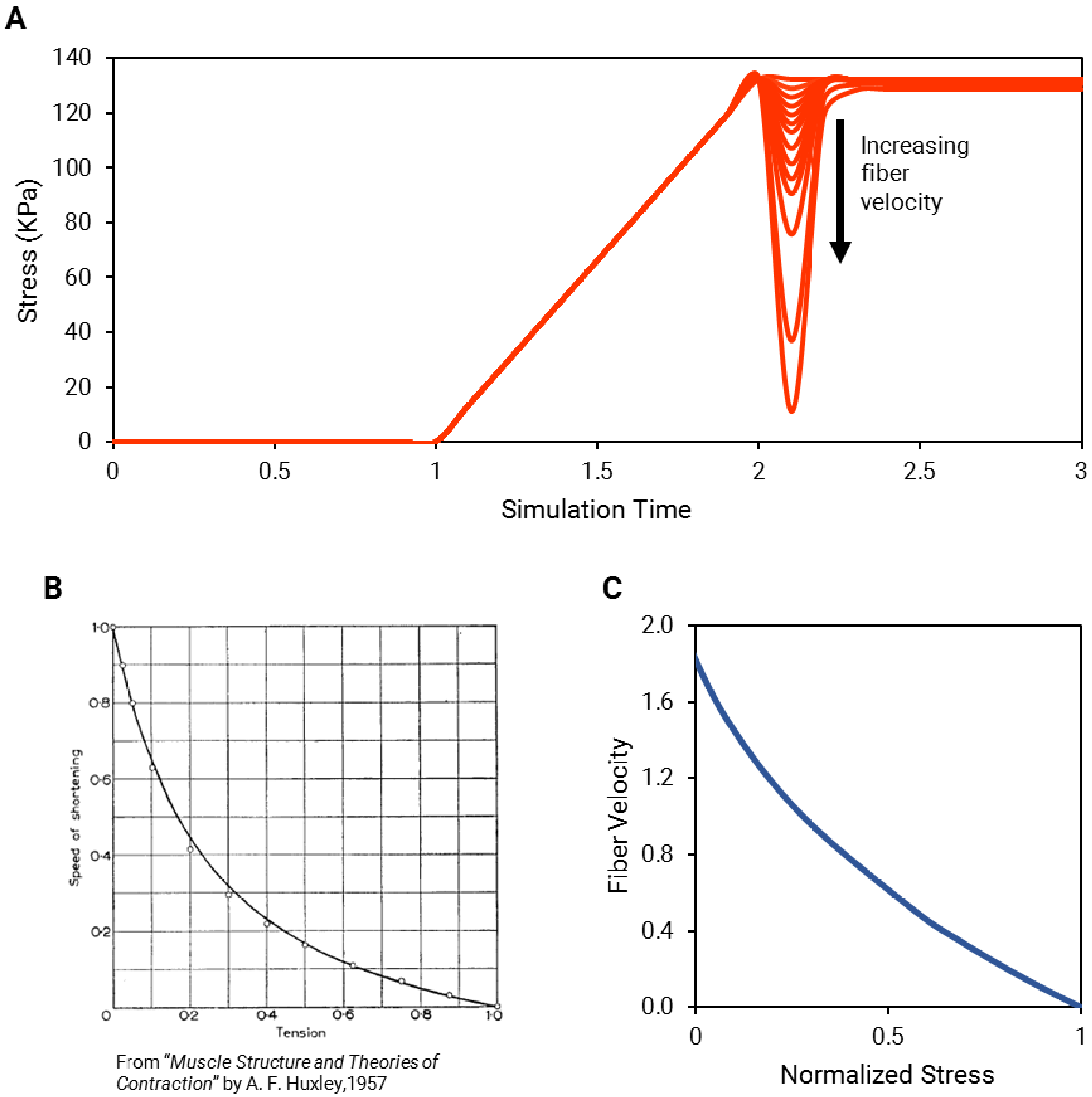

From *"Muscle Structure and Theories of Contraction"* by A. F. Huxley,1957

Figure 2.4 Force-velocity implemented through FEBio plugin. A) Stress response for a single element at increasing fiber shortening velocities. The element is initially held while it contracts and then allowed to shorten after reaching maximum isometric tension. B) Speed of shortening versus tension as reported by Huxley [9]. The speed of contraction decreases as tension increases. C) Simulated fiber velocity versus normalized stress curve, obtained from the simulation shown in A. The simulated curve shows an inverse relationship between tension and velocity, albeit with slightly less curvature than in Huxley's data shown in B.

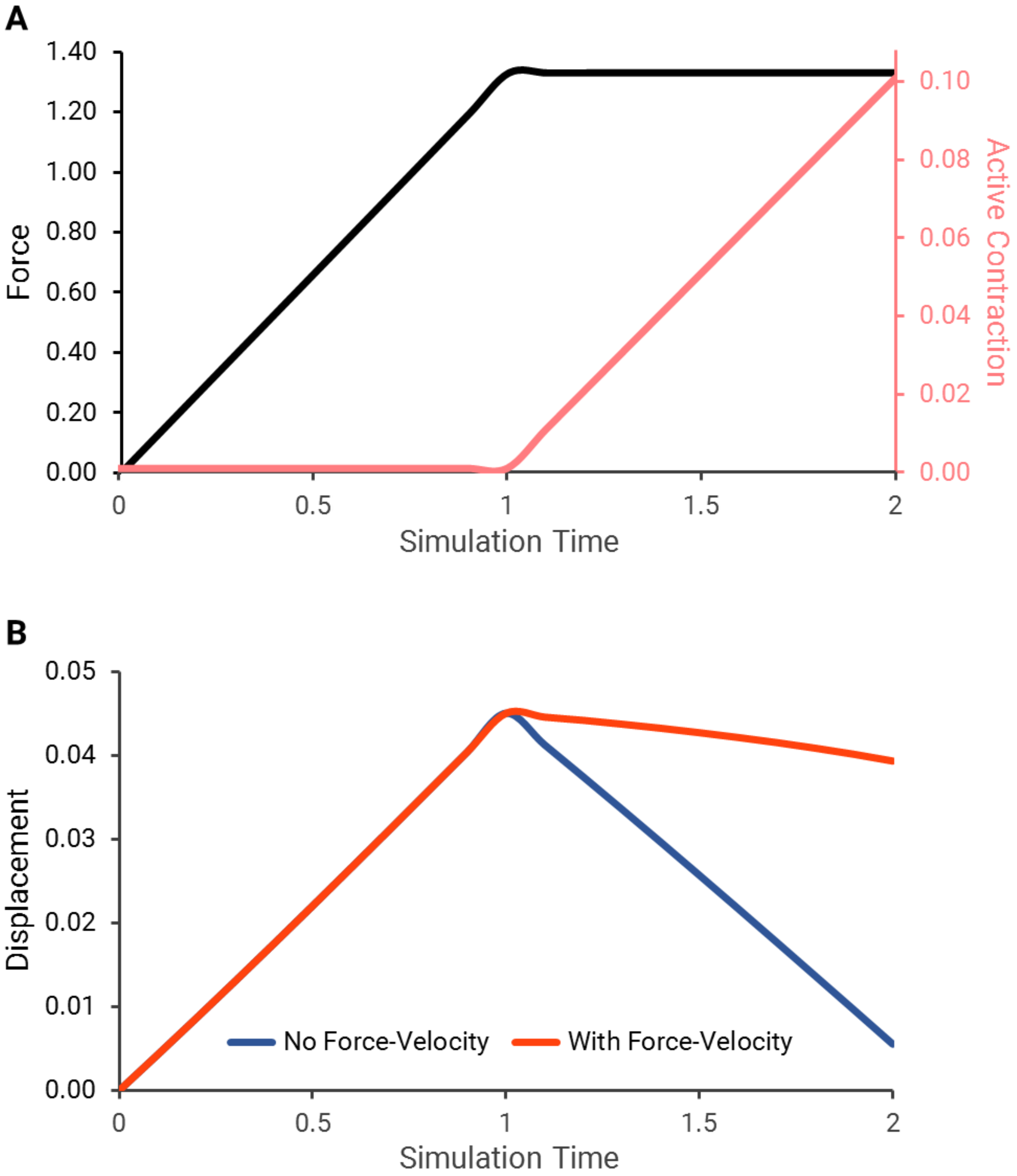

Figure 2.5 Attenuation of shortening by the force-velocity plugin can be seen in a force-controlled single-element simulation. A) The force applied to the element (black) first increases linearly in the absence of contraction and is then held constant as active contraction increases (pink). B) Contraction without force velocity leads to substantial shortening (blue), while force-velocity attenuates the shortening (orange).

Volumetric growth plugin

Growth and remodeling (G&R) are natural processes of biological tissues, as we discussed in Chapter 1. G&R are among the key aspects of adaptation to the external environment and to pathological insults. They are often triggered by direct changes in the mechanical environment, and they in turn alter the mechanical behavior of the material in response to these changes. However, despite how common and critical these processes are, capturing the effect of G&R from a mathematical perspective is challenging.

One particularly useful strategy for mathematically representing G&R is through the use of a volumetric growth framework to redefine stress in response to growth. The concept of volumetric growth for biological G&R was introduced by Skalak (1981) [11] and Skalak et al. (1982) [12]. Subsequently, Rodriguez et al. (1994) [13] adapted the method for use specifically in soft tissues. To illustrate the volumetric growth framework, we can consider the deformation that occurs as a body, β_o, grows to a new state β_1, as seen in Figure 2.6. In order to grow, β_o splits into infinitesimally small components, which are allowed to grow as much as they require in a completely stress-free state, β_g. Once all components grow, they must return together to obtain the final state β_1; however, the grown components will no longer occupy the same spatial locations as before, causing gaps or overlaps between components. In order to ensure spatial compatibility of the grown material, an elastic deformation reconfigures β_g into the final state β_1. The deformation due to growth, $\mathbf{F}_{\text{growth}}$, and the elastic deformation, $\mathbf{F}_{\text{elastic}}$, are defined as the multiplicative decomposition of the total observable deformation, $\mathbf{F}_{\text{total}}$ (Equation 2.21). Because $\mathbf{F}_{\text{growth}}$ occurs in a stress-free state, the elastic deformation is responsible for all the stress introduced by the growth process (Equation 2.22). In the case where the initial and final states are unloaded, the growth introduces residual stress into the material. The presence of residual stresses is evidenced by the opening angle of tissues, such as arteries [14] or myocardium [15], when they are cut open.

$$\boldsymbol{F}_{total} = \boldsymbol{F}_{elastic}\boldsymbol{F}_{growth} \tag{2.21}$$

$$\boldsymbol{\sigma} = \boldsymbol{\sigma}(\boldsymbol{F}_{elastic}) \tag{2.22}$$

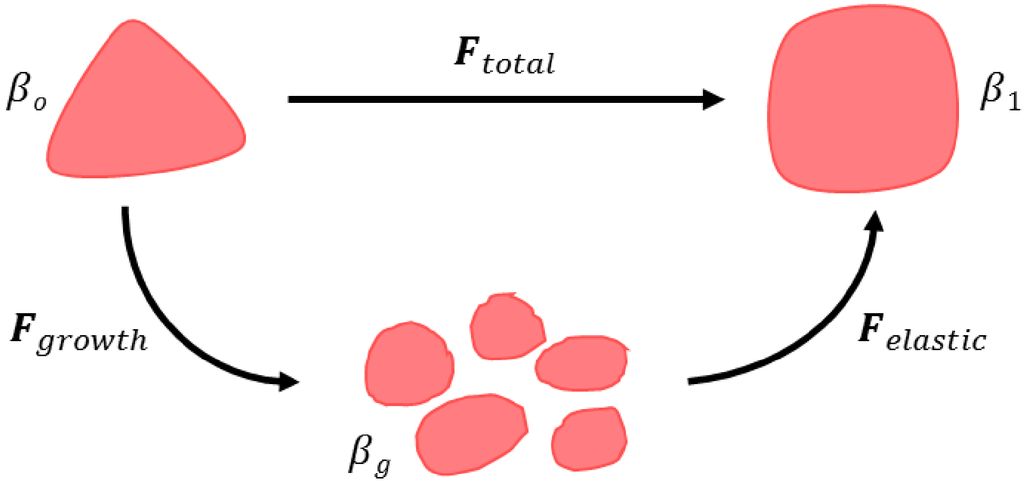

$$\boxed{\begin{gathered}\boldsymbol{F}_{total} = \boldsymbol{F}_{elastic}\boldsymbol{F}_{growth} \\ \boldsymbol{\sigma} = \boldsymbol{\sigma}(\boldsymbol{F}_{elastic})\end{gathered}}$$

Figure 2.6 Volumetric growth framework: To mathematically model the growth process from β_o to β_1, the total deformation $\mathbf{F}_{total}$ is decomposed into a stress-free growth deformation $\mathbf{F}_{growth}$, which takes β_o to β_g, and an elastic deformation $\mathbf{F}_{elastic}$ that then takes β_g to β_1. The stress that occurs during this process is a function of the elastic deformation only.

We incorporated the volumetric growth framework in FEBio using a new material plugin. Our growth plugin redefines the stress components of the compressible transversely isotropic Mooney-Rivlin material to be a function of the elastic deformation rather than the total deformation. The plugin allows users to input a diagonal growth deformation tensor with fiber, cross-fiber, and radial components (Equation 2.23) and requires a user-specified radial vector, in addition to the fiber vector already included in the TIMR material, to define these orthogonal directions. Figure 2.7 shows the displacement induced by growth in each direction for an unloaded, single-element simulation. Using the multiplicative decomposition, we calculate the elastic deformation within the plugin from the total deformation applied to the finite-element model and the user-defined growth deformation tensor (Equation 2.24). Within the plugin material file, we redefined the matrix, fiber, and dilatational components of the stress (Equations 2.25-27) to depend on our calculated elastic deformation. Specifically, we calculate the elastic forms of the left Cauchy-Green deformation tensor **B**, the fiber stretch λ, the deformed fiber direction tensor **A**, the first invariant I_1, and the determinant J. Thus, all calculated stress reflects the applied growth. The effect of growth on the material stress is shown in Figure 2.8, where a single element is stretched to induce stress and then allowed to grow while the total length is held constant. The stress decreases as growth increases despite the fact that length remains constant.

$$\boldsymbol{F}_{growth} = \begin{bmatrix} F_{growth,ff} & 0 & 0 \\ 0 & F_{growth,cc} & 0 \\ 0 & 0 & F_{growth,rr} \end{bmatrix} \tag{2.23}$$

$$\boldsymbol{F}_{elastic} = \boldsymbol{F}_{growth}{}^{-1}\boldsymbol{F}_{total} \tag{2.24}$$

$$\boldsymbol{\sigma}_{Matrix} = \frac{2}{J_{elastic}}\left(\boldsymbol{B}_{elastic}(c_1 + I_{elastic1}c_2) - \boldsymbol{B}_{elastic}{}^2 c_2 - \boldsymbol{I}(c_1 + 2c_2)\right) \tag{2.25}$$

$$\boldsymbol{\sigma}_{Fiber} = \boldsymbol{A}_{elastic}\frac{1}{J_{elastic}}c_3\left(e^{c_4(\lambda_{elastic}-1)} - 1\right) \tag{2.26}$$

$$\boldsymbol{\sigma}_{Dilatational} = K\frac{\ln(J_{elastic})}{J_{elastic}}\boldsymbol{I} \tag{2.27}$$

In Chapter 4, we use the volumetric growth plugin to simulate concentric cardiac hypertrophy in a multiscale model. A cardiomyocyte signaling network model predicts changes in cell area, which are then used to calculate the growth stretch applied to a full finite-element model of the left ventricle. The elastic stretch from the finite-element model is then used as an input to the network model, allowing us the simulate hypertrophy over time.

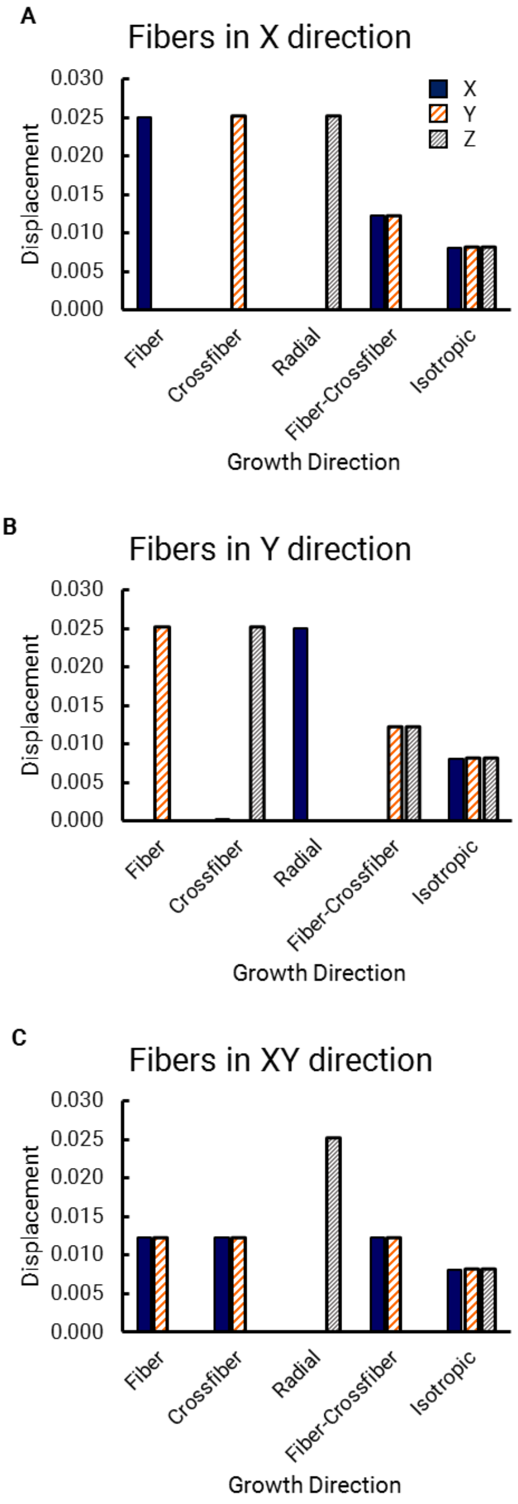

Figure 2.7 Displacement in the X, Y, and Z directions in response to growth in the fiber direction, cross-fiber direction, radial direction, fiber and cross-fiber directions, and isotropically with different fiber directions: A) Fibers in the X direction; B) Fibers in the Y direction; C) Fibers at 45° between the X and Y directions.

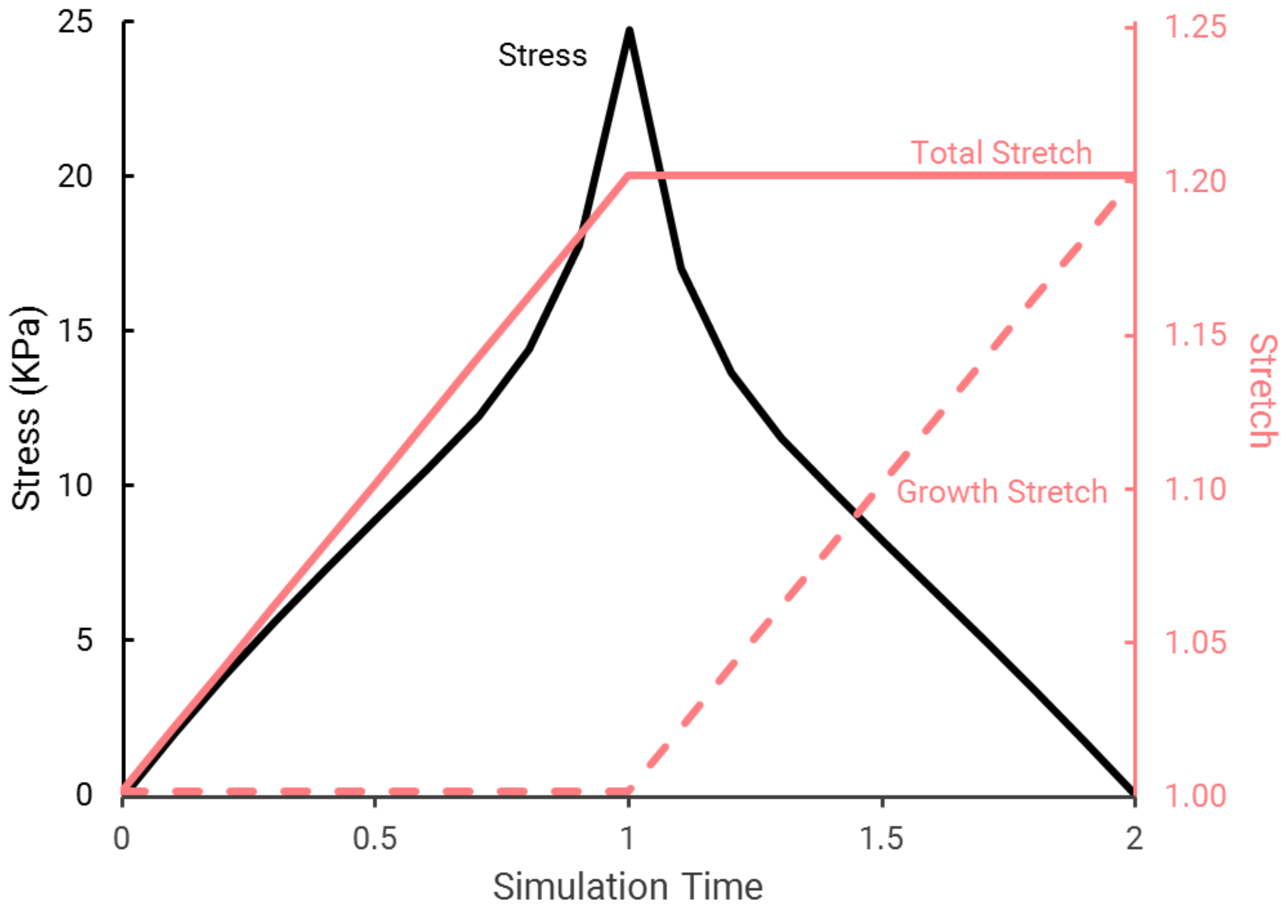

Figure 2.8 Growth reduces stress in a single-element simulation of constant applied stretch. A single finite element is initially stretched (solid pink line), causing an increase in stress (solid black line), and this stretch remains constant during the rest of the simulation. After the increase in stretch, the element is allowed to grow in the fiber direction (dashed pink line). The growth subsequently results in a decrease in stress, in spite of the constant total stretch.

REFERENCES

[1] W. M. Lai, D. Rubin, and E. Krempl, *Introduction to continuum mechanics*. Butterworth-Heinemann/Elsevier, 2010.

[2] A. J. M. Spencer, *Continuum mechanics*. Dover Publications, 2004.

[3] S. Maas, D. Rawlins, J. Weiss, and G. Ateshian, "Theory Manual Version 2.7." [Online]. Available: https://help.febio.org/FEBio/FEBio_tm_2_7/FEBio_tm_2-7.html#.

[4] S. Maas, D. Rawlins, J. Weiss, and G. Ateshian, "FEBio User's Manual Version 2.8." [Online]. Available: https://help.febio.org/FEBio/FEBio_um_2_8/FEBio_um_2-8.html#.

[5] S. A. Maas, S. A. LaBelle, G. A. Ateshian, and J. A. Weiss, "A Plugin Framework for Extending the Simulation Capabilities of FEBio," *Biophys. J.*, vol. 115, no. 9, pp. 1630–1637, Nov. 2018.

[6] "FEBio: FEBio Plugins." [Online]. Available: https://help.febio.org/doxygen/html/plugins.html.

[7] J. M. Guccione, L. K. Waldman, and A. D. McCulloch, "Mechanics of Active Contraction in Cardiac Muscle: Part II—Cylindrical Models of the Systolic Left Ventricle," *J. Biomech. Eng.*, vol. 115, no. 1, pp. 82–90, Feb. 1993.

[8] A. V. Hill, "The heat of shortening and the dynamic constants of muscle," *Proc. R. Soc. London. Ser. B - Biol. Sci.*, vol. 126, no. 843, pp. 136–195, Oct. 1938.

[9] A. F. Huxley, "Muscle structure and theories of contraction.," *Prog. Biophys. Biophys. Chem.*, vol. 7, pp. 255–318, 1957.

[10] P. J. Hunter, A. D. McCulloch, and H. E. ter Keurs, "Modelling the mechanical properties of cardiac muscle.," *Prog. Biophys. Mol. Biol.*, vol. 69, no. 2–3, pp. 289–331, 1998.

[11] R. Skalak, "Growth as A Finite Displacement Field," in *Proceedings of the IUTAM Symposium on Finite Elasticity*, Dordrecht: Springer Netherlands, 1981, pp. 347–355.

[12] R. Skalak, G. Dasgupta, M. Moss, E. Otten, P. Dullemeijer, and H. Vilmann, "Analytical description of growth," *J. Theor. Biol.*, vol. 94, no. 3, pp. 555–577, Feb. 1982.

[13] E. K. Rodriguez, a Hoger, and a D. McCulloch, "Stress-dependent finite-

growth in soft elastic tissues," *J. Biomech.*, vol. 27, no. 4, pp. 455–467, 1994.

[14] Y. C. Fung and S. Q. Liu, "Change of residual strains in arteries due to hypertrophy caused by aortic constriction," *Circ. Res.*, vol. 65, no. 5, pp. 1340–1349, 1989.

[15] E. K. Rodriguez, J. H. Omens, L. K. Waldman, and a D. McCulloch, "Effect of residual stress on transmural sarcomere length distributions in rat left ventricle.," *Am. J. Physiol.*, vol. 264, no. 4 Pt 2, pp. H1048–H1056, 1993.

CHAPTER 3:

MODELING LONGITUDINAL REINFORCEMENT OF ACUTE MYOCARDIAL INFARCTS

INTRODUCTION

Myocardial infarction (MI), commonly known as a heart attack, affects over 1 million Americans each year [1]. Myocardial infarctions occur when blood flow to a region of the heart is interrupted, leading to cardiomyocyte death and loss of regional contractile function. Infarction alters local and global mechanics, initiating a process of adverse growth and remodeling in the surviving myocardium. Here, we define growth as an increase in mass and remodeling as a change in shape or material properties, with the understanding that in the heart these processes often occur in tandem. Over time, the mechanics of the heart are further altered as a stiff collagen scar replaces dead myocytes during the post-MI healing process. Adverse growth and remodeling lead to progressive dilation of the left ventricle (LV) through eccentric hypertrophy, continued deterioration of pump function, and eventually the development of heart failure. Restoring or at least improving cardiac function early in the healing process could help promote long-term survival and deter the development of heart failure. Accordingly, a wide range of therapies that aim to improve function or limit LV remodeling have been proposed, ranging from surgical reinforcement or restraint to augmentation with tissue-engineered patches to injection of various biomaterials [2]–[5].

Mechanical reinforcement approaches can be broadly classified into two groups: global ventricular restraint, including bi-ventricular methods, and local reinforcement, applied directly to the infarct region. Global restraint devices prevent the development of eccentric hypertrophy by physically limiting the size of the entire LV or heart. However, this also leads to impaired filling during diastole. For example, in animal studies the Acorn CorCap reduced LV cross-sectional area, indicating a reversal of eccentric hypertrophy, and preserved shortening compared to sham, but no differences in stroke volume, cardiac output, or contractility were reported [6]–[11]. Other global restraint devices, such as the Paracor HeartNet, Myocor Coapsys, and Cardio-Clasp performed similarly when used in end-stage heart failure, although not all have been tested for the prevention of post-infarction eccentric remodeling [2].

A number of emerging treatments – including injection of stiff biomaterials into the infarct – attempt to achieve a similar reduction in eccentric hypertrophy without restraining the entire heart; for simplicity we focus here on local surgical reinforcement with synthetic meshes as a prototypical example. In contrast to the consistent reduction of eccentric hypertrophy seen with the global restraint methods, there is marked variability in the effectiveness of local reinforcement. For example, one group reported that local reinforcement with a polypropylene patch of infarcts induced by occlusion of the left anterior descending coronary reduced end-diastolic and end-systolic volumes and improved cardiac output, stroke volume and ejection fraction relative to untreated controls [12]; yet the same group found that reinforcement of infarcts caused by occlusion of the left circumflex coronary artery in the same animal model yielded no significant improvement [13]. Our group recently reviewed these studies of both global and local reinforcement [2], [14], and found a striking difference in the efficacy of local vs. global restraint. Among the goals of our lab has been to understand the mechanisms driving the response to these different therapies and to harness that understanding to develop more effective approaches.

For this purpose, our lab developed a promising approach to improving pump function acutely following a large anteroapical infarction by selectively reinforcing the infarct in the longitudinal direction [15]. We began by conducting a computational screen for how infarct material properties impact pump function [16]. In agreement with prior work by other groups [17], [18], the finite-element model used in that screen predicted that isotropic stiffening of an infarct would improve systolic function at the cost of restricting filling, resulting in no net gain in stroke volume at matched pressures. On the other hand, the model predicted that an anisotropic infarct with high longitudinal stiffness but low circumferential stiffness would maximize stroke volume, primarily by improving filling. We then validated the model prediction in a canine model of MI by acutely sewing a modified Dacron patch onto the surface of the heart. Volumes, pressures, and infarct region segment lengths were measured at baseline pre-MI, acutely post-MI, and after application of the patch. These data were used to compare the cardiac output (CO) at matched pressures between each of the conditions. As expected, acute ischemia shifted the CO-end-diastolic pressure (EDP) curve downward, so that cardiac output was reduced at matched filling pressures. Anisotropic reinforcement shifted the CO-pressure curve upward, closer to baseline, indicating an increase in CO at matched pressures [15].

While our experimental studies validated the overall model prediction that longitudinal infarct reinforcement improved LV function, the mechanisms underlying that improvement in the experiment did not match the original model predictions. In contrast to the model predictions, the primary effect of experimental longitudinal reinforcement was on systolic function, indicated by a leftward shift in the end-systolic pressure-volume relationship (ESPVR) after application of the patch. Another surprise was that local segment lengths tracked by sonomicrometry increased at matched end-diastolic pressures acutely post-MI, indicating apparent softening in the infarct region that was not predicted in the original model but was significantly modified by application of the patch.

Thus, the aim of the current modeling study was to re-examine the mechanisms by which longitudinal reinforcement of acute, anteroapical myocardial infarcts leads to improvement in stroke volume at matched pressures. We tested potential mechanisms by creating a new set of finite-element models of the canine LV tuned to capture the behavior observed in the experiments. Our new models improve upon the previous computational study [16] by allowing differences in passive material behavior between healthy and ischemic myocardium; by carefully fitting geometry, passive material properties, and active material properties to experimental data from our laboratory; and by simulating full pressure-volume loops over a range of loading conditions to map diastolic and systolic pressure-volume relationships. Our results suggest that longitudinal reinforcement reduces peak diastolic fiber stretch and systolic fiber stress in the remote myocardium and shifts those peaks away from the endocardial surface by reshaping the left ventricle. This redistribution shifts the end-systolic pressure-volume relationship (ESPVR) leftward, indicating improved ejection against a given systolic pressure, with little impact on diastolic filling.

METHODS

Model Construction

We built new finite-element models of the acutely ischemic canine LV by creating an average geometry from CINE magnetic resonance imaging (MRI) scans of sixteen different dogs taken 48 hours post-MI (Figure 3.1A) as part of a prior study [19]. For each scan, we segmented the endocardial and epicardial contours in 7-10 short-axis slices acquired at end systole using the open-source software Segment (v1.9 R3767, http://medviso.com/segment/) running in MATLAB (R2014b, Mathworks), and fitted the endocardial and epicardial surfaces in prolate spheroidal coordinates with meshes of 4x4 bicubic Hermite elements (Figure 3.1B) [20]. We exported points at specified angular coordinates from each of the 16 fitted surfaces, then calculated the average endocardial and epicardial points to define an average geometry in prolate spheroidal coordinates (Figure 3.1C). We then used linear interpolation between the endocardial and epicardial points to define mesh nodes across the wall. The nodes were converted to Cartesian coordinates, and a hexahedral element connectivity matrix was defined for a finite-element model implementation in FEBio 2.6.4 (febio.org). We used an additional ring of rigid-body elements adjacent to the basal-most endocardial layer to simulate a valve ring and a ring of pentahedral rigid-body elements to seal the apex. Our final finite-element mesh consisted of 9680 nodes and 7840 linear elements (Figure 3.1E). In each layer of the LV we assigned a fiber direction ranging from -60° on the epicardium to 60° on the endocardium [21]. We simulated loading by applying a specified pressure to the endocardial surface of the LV, using the Pardiso solver in FEBio to solve for the equilibrium configuration at each step.

Because the MRI contours used to make the model were obtained at end systole, we scaled the fitted mesh to better approximate the unloaded geometry of the LV. This unloaded geometry was taken to be stress-free in all simulations. We scaled the unloaded geometry in prolate spheroidal coordinates by multiplying the focus of each layer of nodes across the wall by scaling factors that increased evenly in value from the endocardial to epicardial surface, thus obtaining a smaller cavity volume while maintaining the same wall volume. We iterated through the scaling process until we obtained an unloaded geometry that resulted in simulated end-diastolic volumes similar to the experimental data (Figure 3.1D). The new unloaded model had a cavity volume of 30mL and was used in the optimization scheme described below to obtain passive material parameters.

The mechanics of an acutely ischemic region are typically simulated by turning off active contraction but assuming that the passive material properties are unchanged, since inflammation and wound healing have not yet begun. However, our previous canine study found significant increases in local end-diastolic segment lengths measured by sonomicrometry during acute ischemia at matched end-diastolic pressures (EDP) [15]. This unexpected behavior is particularly interesting because longitudinal reinforcement, which successfully improves pump function, also reverses this diastolic remodeling in the infarct region. While the exact mechanism by which the ischemic region appears to soften is not fully understood, we suspect that the loss of perfusion in that region leads to an immediate thinning of the wall and thus higher stresses and stretches at matched EDP [22]. Alternatively, loss of pressurization of the coronary vessels may reduce passive stiffness directly [23]. For the purpose of our finite-element models, we can capture this apparent softening in the infarct region either by changing the local wall thickness or by changing the passive material properties of the infarct region; here, we chose to alter the passive material properties.

A nearly-incompressible transversely isotropic Mooney-Rivlin (TIMR) material available in FEBio was used to simulate normal myocardium, ischemic myocardium, and the patch used for surgical reinforcement. This material combines the standard strain energy function for an isotropic Mooney-Rivlin material with a term that depends nonlinearly on strain along one defined fiber direction (Equation 3.1). The strain energy function of the TIMR material includes five user-defined parameters: C_1 (isotropic term), C_2 (isotropic term), C_3 (linear fiber term), C_4 (exponential fiber term), and K (bulk modulus). In order to reduce the number of free parameters in our optimization, we fixed the values of two of these parameters for all simulations. Based on prior work [24], [25] showing that functions of the first and fourth invariants of the right Cauchy-Green deformation tensor (I_C and IV_C in Equation 3.1) provide a good description of the passive behavior of myocardium, we set C_2 to 0, eliminating the contribution of the second invariant II_C. In addition, based on a parameter sensitivity analysis that revealed that the value of K had little effect on the material behavior during passive inflation as long as K >> C_1, we set K = 100 for all simulations. The remaining three parameters were optimized for three different cases: normal myocardium (Baseline), acutely ischemic myocardium (Acute Ischemia) and the longitudinally stiff patch (Longitudinal Patch).

$$\begin{gathered} W = C_1(I_C - 3) + C_2(II_C - 3) + \mathrm{F}\left(\sqrt{IV_C}\right) + \frac{K}{2}[\ln(J)]^2 \\ \frac{\partial W}{\partial I_C} = C_1 \qquad \frac{\partial W}{\partial II_C} = C_2 \qquad \frac{\partial W}{\partial IV_C} = \frac{1}{\lambda_1} C_3\left(e^{C_4(\lambda_1 - 1)} - 1\right) \end{gathered} \tag{3.1}$$

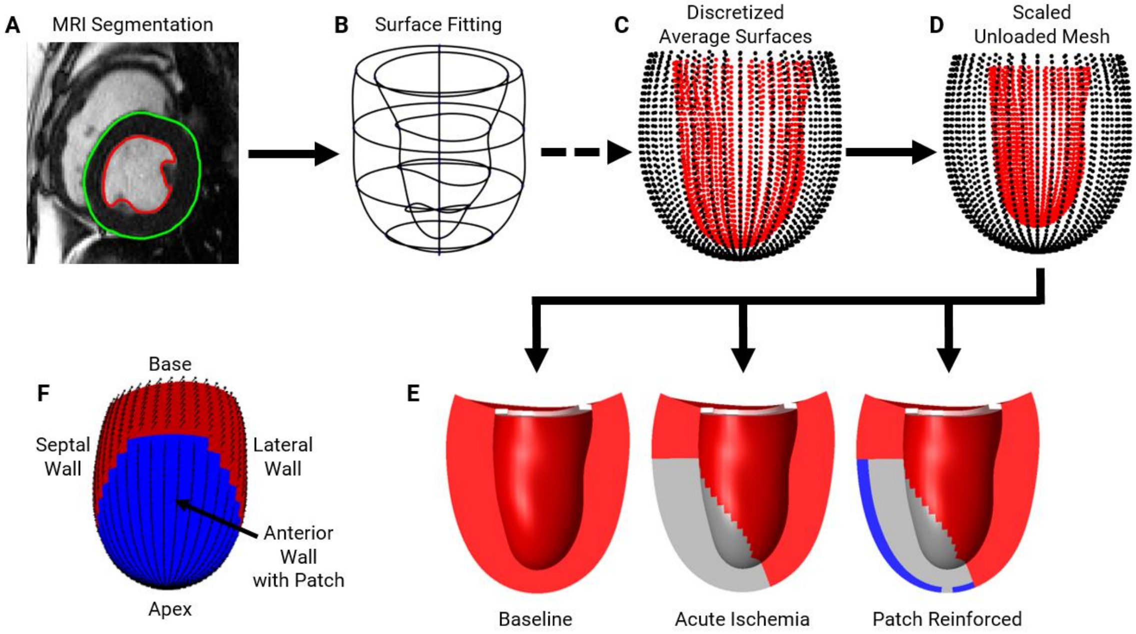

Figure 3.1 Model construction pipeline: **A)** Representative example of MRI segmentation of the endocardium and epicardium in short axis slices of the left ventricle; all MRI data were taken from a previous study by Clarke et al. [19]. **B)** Cubic Hermite surfaces are fitted to the segmented slices for each specimen. **C)** Individual specimen surfaces are discretized into an average surface and **D)** scaled down to create an unloaded mesh that preserves the initial wall volume. **E)** The unloaded mesh is then used to create three distinct finite-element models of the baseline, acutely ischemic, and patch-reinforced left ventricle. **F)** The patch reinforces the ischemic region on the anterior wall of the left ventricle.

Material Property Optimization

The three materials of interest were optimized in two steps: first, normal and ischemic myocardium parameters were fitted together using data from the published experimental results; then, the longitudinally stiff patch was added by modifying the top layer of elements in the infarct region and its material properties were fitted using additional experimental data taken following patch application. We optimized the normal and ischemic myocardium material parameter sets simultaneously by comparing the Baseline and Acute Ischemia model results to six experimental values from our previously published experiments [15]: end-diastolic volumes (EDV_{Base}; EDV_{Isch}) for baseline and acute ischemia at their respective average end-diastolic pressures, which allow us to match the overall compliance of the heart; circumferential (E_{circ}) and longitudinal (E_{long}) remodeling strains in the anterior midwall at a matched pressure of 12mmHg, which capture the apparent softening of the ischemic myocardium; and the changes in base-apex (L_{BA}) and septal-lateral (L_{SL}) cavity dimensions between baseline and ischemia at a matched end-diastolic pressure of 12mmHg, which provide information on the anisotropy of the normal myocardium. Model volumes were calculated using the nodal positions of the second layer of nodes from the endocardium, to match the positions of the sonomicrometry crystals used to measure the experimental volumes. As shown in Equations 3.2-3.3 and diagrammed in Figure 3.2, the remodeling strain reflects the remodeling deformation occurring from Baseline to Acute Ischemia, which we calculated by inflating both the baseline model and the model with acutely ischemic properties in the infarct region from unloaded to 12mmHg. Because both models share a common unloaded state, we can use a multiplicative decomposition to relate the deformation occurring in Acute Ischemia, $F_{Ischemia}$, to the Baseline deformation,

$F_{Baseline}$, through the remodeling deformation, $F_{Remodeling}$. Model strains were averaged across twenty elements in the infarct region that corresponded to the experimental locations of the sonomicrometry crystals. For the patch model, the optimization criteria include three metrics: end-diastolic volume at the experimentally measured end-diastolic pressure (EDV_{patch}) and the circumferential (E_{circ}) and longitudinal (E_{long}) remodeling strains at a matched pressure of 12mmHg, reflecting the diastolic strain differences induced by patch placement relative to ischemia alone.

In order to force outputs from the optimized model to remain within one standard deviation of the experimental means, we selected a nonlinear error measure for use in the optimization. We defined an exponential error function (Equation 3.4) using scaled Z scores. We calculated a traditional Z score by dividing the difference between the model output and the experimental mean by the experimental standard deviation, then subtracted one and multiplied the result by a scaling term to more heavily penalize values beyond one standard deviation. Thus, an output that matched the experimental mean yielded an error of 1/1000, an output one standard deviation from the mean yielded an error of one, and an output two standard deviations from the mean yielded an error value of 1000. This approach allowed us to both heavily penalize model outputs that fell outside one standard deviation of the experimental means and weigh data with different orders of magnitude equally in the fit.

$$\boldsymbol{E}_{Remodeling} = \frac{1}{2}(\boldsymbol{F}_{Remodeling}^{T}\boldsymbol{F}_{Remodeling} - \boldsymbol{I}) \tag{3.2}$$

$$\boldsymbol{F}_{Remodeling} = \boldsymbol{F}_{Ischemia}\boldsymbol{F}_{Baseline}^{-1} \tag{3.3}$$

$$Error_i = e^{\left(\ln(1000)\left(\frac{|Mean_i - Model_i|}{SD_i} - 1\right)\right)}$$

$$Total\ Error = \sum_i Error_i \quad ,where\ i = optimization\ criteria \qquad (3.4)$$

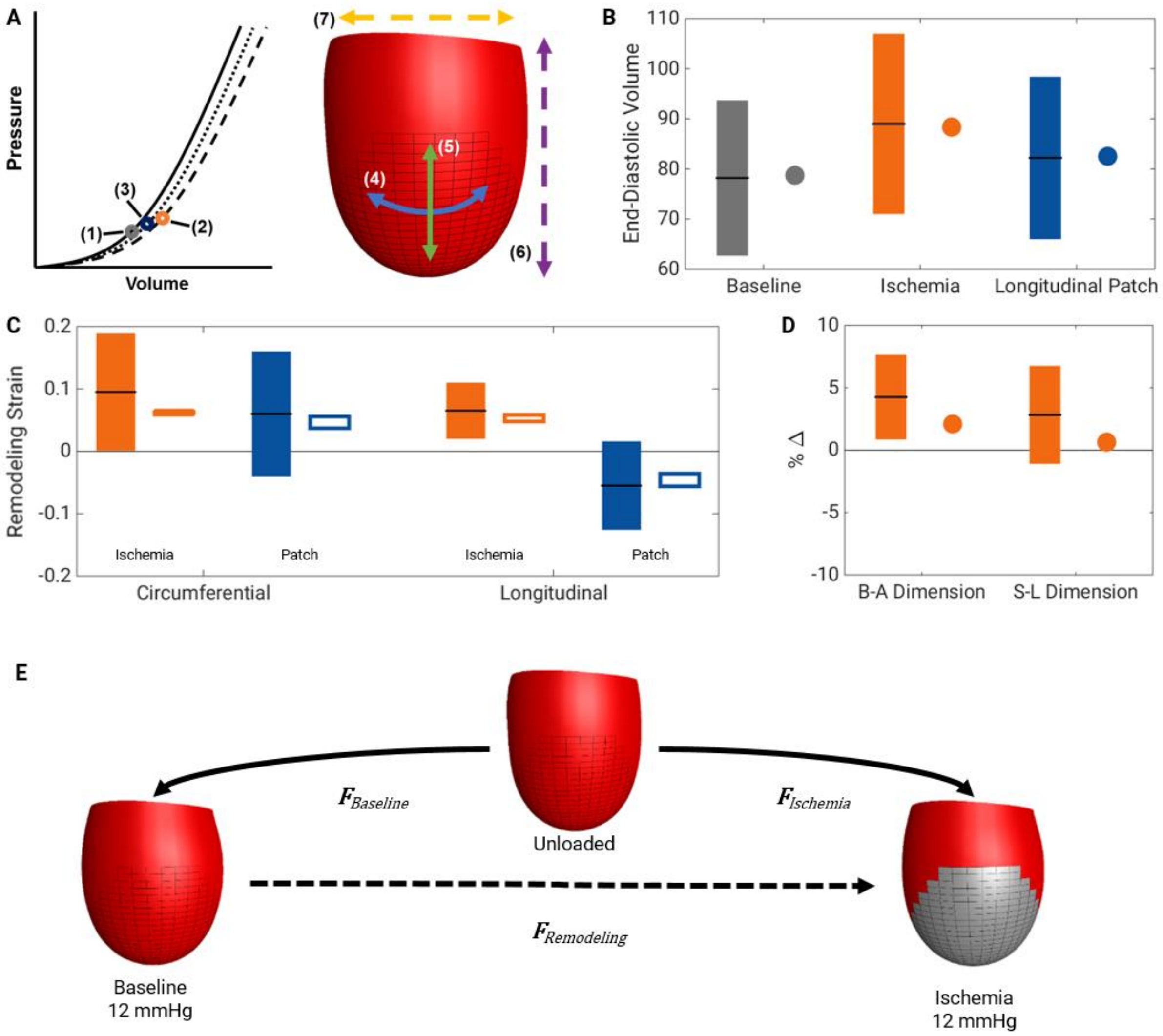

Figure 3.2 Model parameter fitting: **A)** Data used for fitting were taken from a previous study by Fomovsky et al. [15] and included end-diastolic volumes for baseline (1), acute ischemia (2), and longitudinal patch (3); circumferential (4) and longitudinal (5) remodeling strains; and the change in base-apex (6) and septal-lateral (7) dimensions between acute ischemia and baseline. **B)** Mean end-diastolic volume (line) ± 1SD (filled boxes) for baseline, acute ischemia, and longitudinal patch and the corresponding model values (circles) at matched experimental pressures. **C)** Mean remodeling strain (line) ± 1SD range (filled boxes) for acute ischemia and longitudinal patch in the circumferential and longitudinal directions. Model values (open boxes) correspond to the range of values for twenty elements within the center of the infarct area in the midendocardial layer. **D)** Mean percent change (line) ± 1SD range (filled boxes) for base-apex and septal-lateral dimensions between acute ischemia and baseline at end diastole and corresponding model values (circles) at matched experimental pressures. **E)** Schematic showing how the remodeling deformation relates the baseline and ischemic region deformations at a matched pressure.

Active Contraction and Pressure-Volume Loops

We implemented a custom active contraction plugin that combines the length-dependent behavior currently used in FEBio [26] and a modified force-velocity relationship based on the fading-memory formulation proposed by Hunter, McCulloch, and ter Keurs [27]. The tension generated in our active contraction module (Equation 3.5) is the product of three distinct components: a time-varying normalized activation, e(t), that defines the time course of force generation throughout the cardiac cycle; an instantaneous length-dependent term that scales the peak possible isometric tension based on the current fiber stretch; and a force-velocity term that dampens the instantaneous force generation based on the rate of shortening of the fibers. The parameters used in our active contraction module are presented in Table 1. The total fiber stress is the sum of the passive fiber stress, calculated from the strain-energy density function in Equation 3.1, and the tension generated in our active contraction module (Equation 3.6). We simulated full pressure-volume loops by applying the average pressure time course from each experimental case on the endocardial surface and optimizing the normalized contractility loadcurve e(t) to match the measured time course of volume change relative to end diastole (V(t)-EDV) for each experimental case. Because we only measured pressure and volume curves for one patch configuration (longitudinal reinforcement) in our previous experiments, for simulations where we compared different patch configurations we employed the acute ischemia pressure load and normalized contractility curves in our models of longitudinal, circumferential, and isotropic patch reinforcement.

$$T\big(t,\lambda(t)\big) = e(t)\left[T_{max}\frac{Ca_o^2}{Ca_o^2 + ECa_{50}^2\big(\lambda(t)\big)}\right]\left[\frac{1 + aQ\big(t,\lambda(t)\big)}{1 - Q\big(t,\lambda(t)\big)}\right]$$

$$ECa_{50}\big(\lambda(t)\big) = \frac{Ca_{o\,max}}{\sqrt{e^{\beta[\lambda(t)l_r - l_o]} - 1}} \tag{3.5}$$

$$Q\big(t,\lambda(t)\big) = A_1\int_{-\infty}^{t} e^{-\alpha_1(t-\tau)}\dot{\lambda}(\tau)d\tau$$

$$\sigma_{fiber,\ total}\big(t,\lambda(t)\big) = \sigma_{fiber,\,passive}\big(\lambda(t)\big) + T\big(t,\lambda(t)\big) \tag{3.6}$$

A detailed overview of the force-velocity plugin is found in Chapter 2.

RESULTS

Optimized models match measured hemodynamics

Optimized passive material properties for the Baseline, Acute Ischemia, and Patch models are listed in Table 3.2 and optimized model outputs are shown relative to the data in Figure 3.2 and Table 3.3. In order to capture the apparent softening of the acutely ischemic region, the isotropic (C_1), linear fiber (C_3), and exponential fiber (C_4) terms were reduced in the acutely ischemic myocardium by -50%, -30%, and -10%, respectively, relative to baseline. Following optimization of the normalized contractility loadcurves (e(t) in Equation 3.5), model pressure-volume loops matched experimental data for all three conditions very well (Figure 3.3). The optimized curves were quite similar for the ischemia and longitudinal patch cases (Figure 3.3C), but both of these cases required substantially higher peak contractility than the baseline case to match measured volume changes.

End-diastolic and end-systolic pressure volume relationships (EDPVR and ESPVR, respectively) generated using the optimized FE models reproduced the major trends observed in the original experiment: ischemia shifted the ESPVR rightward and longitudinal patch reinforcement partially reversed that shift, with relatively little impact on diastolic properties (Figure 3.4A). Comparing end-diastolic and end-systolic volumes at matched pressures, the FE models matched the experimentally measured changes due to acute ischemia and patch application closely (Figure 3.4B).

Longitudinal reinforcement redistributes fiber stretch and reduces stress

Once we verified that the models matched the experimentally observed behavior during both acute ischemia and longitudinal reinforcement, we used the model to explore potential mechanisms underlying the functional benefit of longitudinal reinforcement. Plotting end-diastolic fiber stretch at matched pressures showed that ischemia increases stretch in the inner half of the wall (Figure 3.5A), and longitudinal reinforcement partially relieves that endocardial stretch. Patch reinforcement also reduces end-systolic fiber stress in large portions of the noninfarcted myocardium relative to the acute ischemia simulation (Figure 3.5B). Overall, the patterns of both end-diastolic fiber stretch and end-systolic fiber stress following patch reinforcement were similar to the baseline case, with the greatest stretch and active stress generation occurring deeper into the wall rather than directly on the endocardium as in the acute ischemia case.

Table 3.1 Active contraction parameters for noninfarcted myocardium.

T_{max}	135.7 KPa
Ca_0	4.35
Ca_{max}	4.35
β	4.75
l_0	1.58
l_{ref}	1.58
α	75
A	50
a	0.5

Table 3.2 Fitted passive material parameters for normal myocardium, ischemic myocardium, and patch materials, along with the percent change in each parameter compared to normal myocardium.

	Normal Myocardium	*Ischemic Myocardium*	*%Δ*	*Patch*	*%Δ*
C_1 [KPa]	0.5	0.25	-50%	3.1	+520%
C_2 [KPa]	0	0	0%	0	0%
C_3 [KPa]	0.0005	0.00035	-30%	10	$+1.9\times10^{6}$ %
C_4 [unitless]	50	45	-10%	70	+40%
K [KPa]	100	100	0%	100	0 %

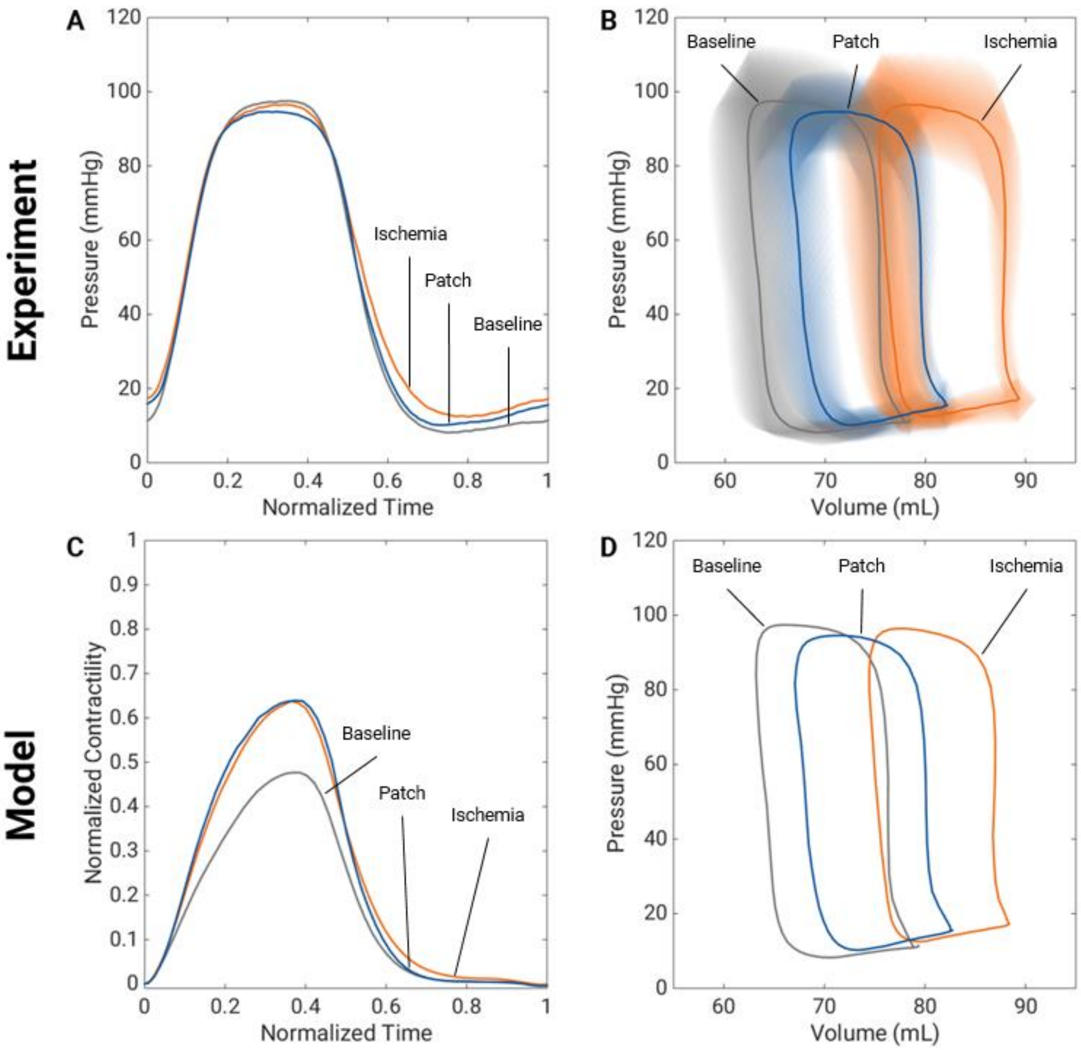

Figure 3.3 Full cardiac cycle simulations: **A)** Average experimental pressure vs. time curves (solid lines) for baseline, acute ischemia, and longitudinal patch. These pressures are used as the loading conditions for the finite-element models. **B)** Average experimental pressure-volume loops (solid lines) ± 1SD (shaded area) for baseline, acute ischemia, and longitudinal patch. The loops show the rightward shift in volume caused by acute ischemia and subsequent leftward shift after longitudinal reinforcement. All experimental curves were generated by averaging raw data from a previous study by Fomovsky et al. [15] **C)** Normalized contractility loadcurves optimized for each finite-element model to match the measured change in volume vs. time curves. With fewer contracting elements, the acute ischemia and longitudinal patch models required higher normalized contractility compared to baseline. **D)** Model pressure-volume loops for baseline, acute ischemia, and longitudinal patch. The simulated loops follow the experimental trends shown in Panel (B).

Table 3.3 Data used to fit the passive material properties for normal myocardium, ischemic myocardium, and patch materials, as well as the respective model values and corresponding error. Data were taken from a previous study by Fomovsky et al. [15]. Experimental data shown as mean ± one standard deviation. Remodeling strain model values shown as average with range in parenthesis, calculated from 20 central elements in the ischemic region.

	Experiment	**Model**	**Error**
$\text{EDV}_{\text{Baseline}}$	78.2 ± 15.5	78.79	0.001302
$\text{EDV}_{\text{Ischemia}}$	89 ± 18	88.33	0.001293
$\text{EDV}_{\text{Patch}}$	82.2 ± 16.2	82.48	0.001126
Remodeling $E_{\text{circ, ischemia}}$	0.095 ± 0.094	0.0621 *(0.05895 to 0.06514)*	0.01122
Remodeling $E_{\text{long, ischemia}}$	0.065 ± 0.045	0.05281 *(0.04788 to 0.05842)*	0.0065
Remodeling $E_{\text{circ, patch}}$	0.06 ± 0.1	0.0474 *(0.0369 to 0.0558)*	0.002387
Remodeling $E_{\text{long, patch}}$	-0.055 ± 0.071	-0.0477 *(-0.0561 to -0.0369)*	0.0004933
B-A $\text{Change}_{\text{ischemia}}$	4.256 ± 3.393	2.1053	0.07972
S-L $\text{Change}_{\text{ischemia}}$	2.827 ± 3.929	0.6273	0.04782
Total Error			**0.1519**

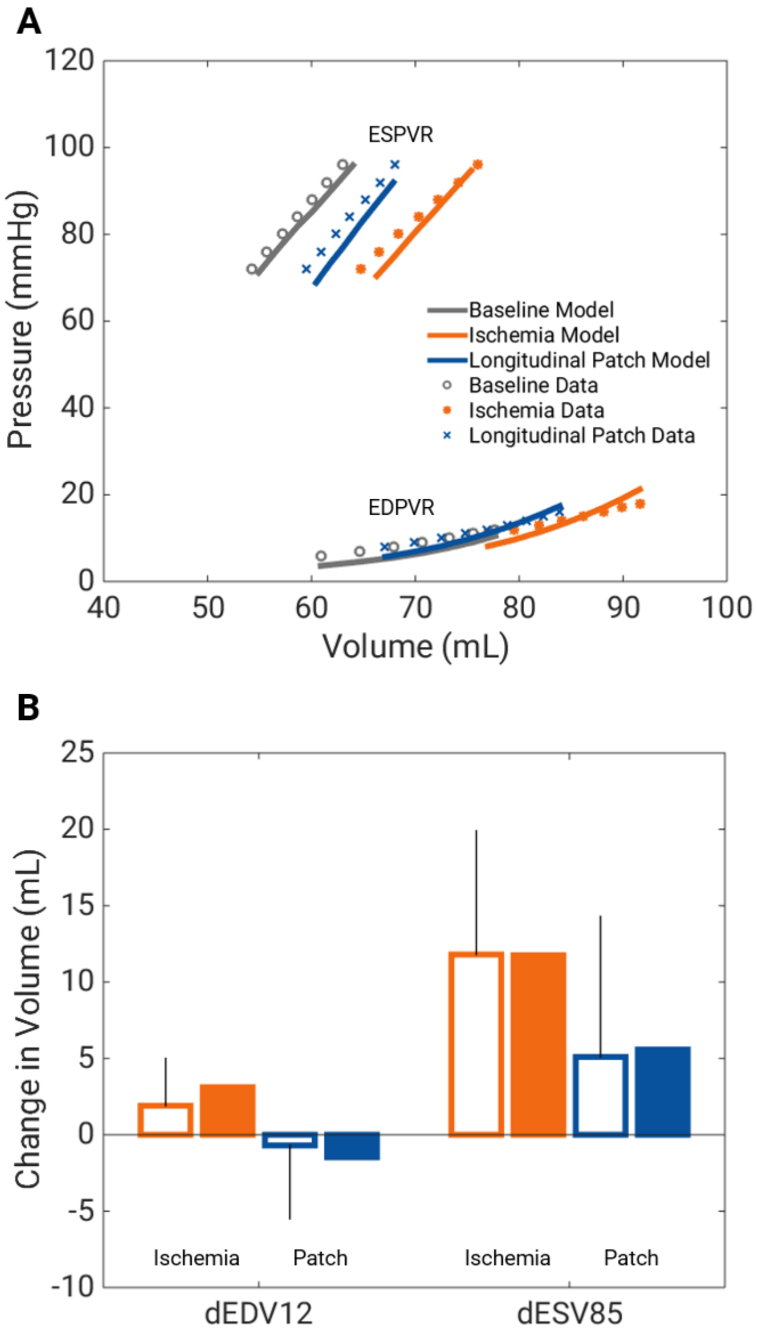

Figure 3.4 Pressure-volume relationships: **A)** End-diastolic and end-systolic pressure-volume relationships (EDPVR and ESPVR, respectively) for experiments (symbols, data from Fomovsky et al. [15]) and model (lines), obtained by performing or simulating IVC occlusions. **B)** Change from baseline in end-diastolic volume at matched pressure of 12mmHg (dEDV12) and end-systolic volume at 85mmHg (dESV85) for acute ischemia (orange) and longitudinal patch (blue). (Experimental mean shown with open boxes ± 1SD and model simulations shown with filled boxes).

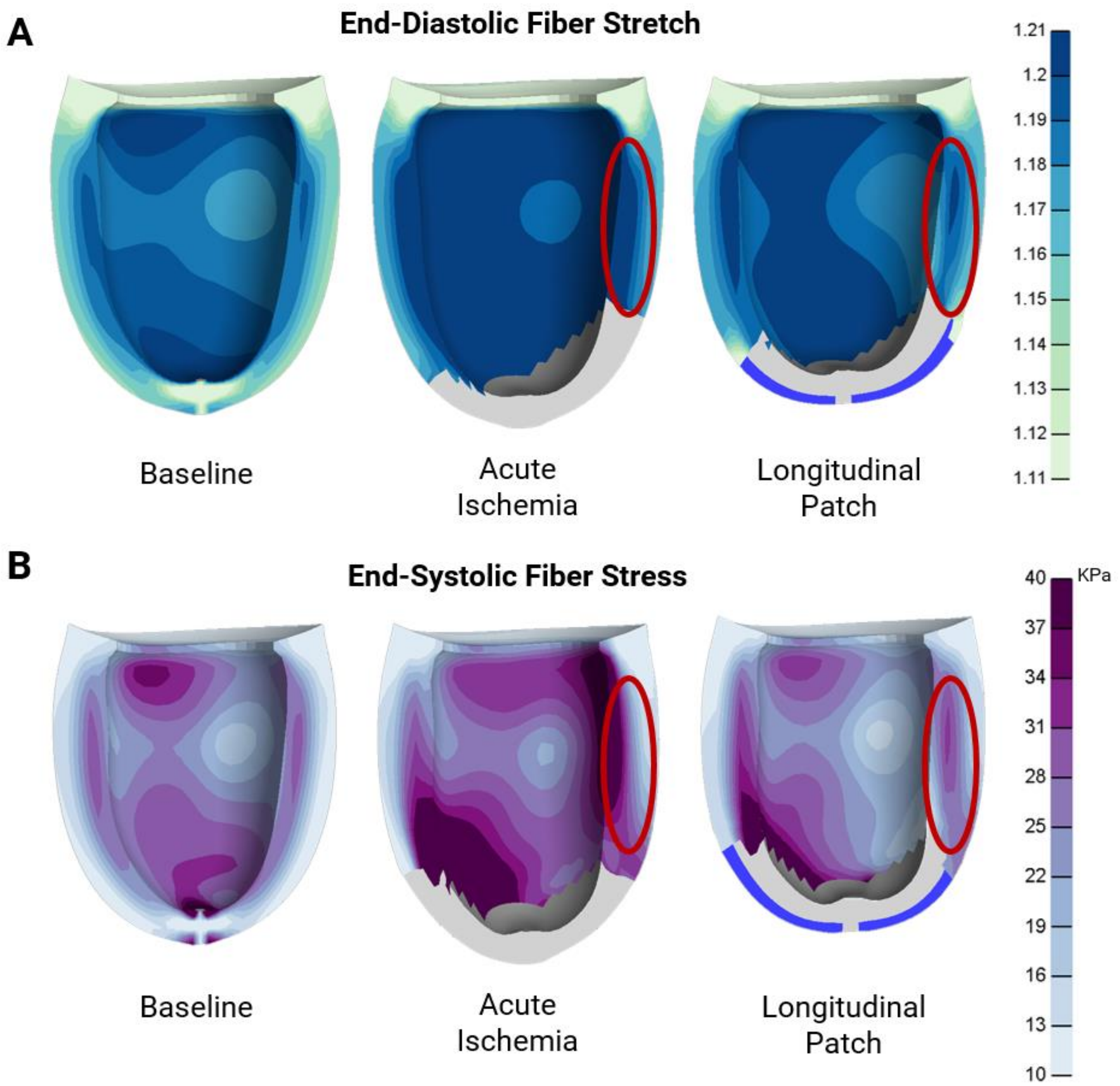

Figure 3.5 Transmural stretch and stress distributions: **A)** End-diastolic fiber stretch in the remote, non-infarcted elements of the baseline, acute ischemia, and longitudinal patch models seen in anterior-facing cross-sections. Fiber stretch increases in the endocardial layer due to acute ischemia, but longitudinal reinforcement redistributes the increased fiber stretch to the midwall layer. **B)** End-systolic fiber stress in the remote, non-infarcted elements of the baseline, acute ischemia, and longitudinal patch models seen in anterior-facing cross-sections. Following a similar pattern to the end-diastolic stretch, acute ischemia leads to increased fiber stress in the endocardial layer, while longitudinal reinforcement leads to reduced fiber stress overall and a transmural redistribution that relieves the stress in the endocardium.

Comparison of different patch configurations

Given the many improvements in the current model relative to our previously published model of patch reinforcement [16], we decided to revisit the conclusion of that earlier paper that longitudinal reinforcement not only improves LV function but does so to a greater degree than either circumferential or isotropic reinforcement. We therefore created two additional FE models of circumferential and isotropic reinforcement by using the same material properties for the patch layer but changing the fiber direction to be circumferential in all elements (circumferential) or radially symmetric about the center of the simulated infarct (isotropic). Comparing PV loops generated with identical pressure and normalized contractility loadcurves confirmed that longitudinal reinforcement is most effective in reducing LV volumes (Figure 3.6A) as well as in increasing stroke volume (Figure 3.6B) relative to acute ischemia. Stroke volume increased by 10.7% with longitudinal reinforcement, by 6.3% with isotropic reinforcement, and by 2.3% with circumferential reinforcement.

Plotting the change in end-systolic fiber stress relative to the acute ischemia case also showed that longitudinal reinforcement decreases fiber stresses throughout much of the LV, particularly in the inner half of the wall, while transferring some stress to the outer half of the wall (Figure 3.7A). Isotropic reinforcement produces a similar pattern but smaller reductions in fiber stress, while circumferential reinforcement increases fiber stresses in most of the wall. These differences appear to result in part from shape changes induced by ischemia and reinforcement. In particular, ischemia increases the length (base-apex dimension) of the LV and longitudinal reinforcement restores this dimension to normal (Figure 3.7B). Because we did not observe substantial changes to the septal-lateral or anterior-posterior dimensions with the different patch configurations (not shown), differences in their effects on the base-apex dimension led to a more spherical shape under longitudinal reinforcement and a more elliptical shape with circumferential reinforcement (Figure 3.7C). This effect on the geometry of the ventricle is also consistent with the increased stretch and contraction observed in circumferentially aligned fibers of the longitudinally reinforced model discussed above.

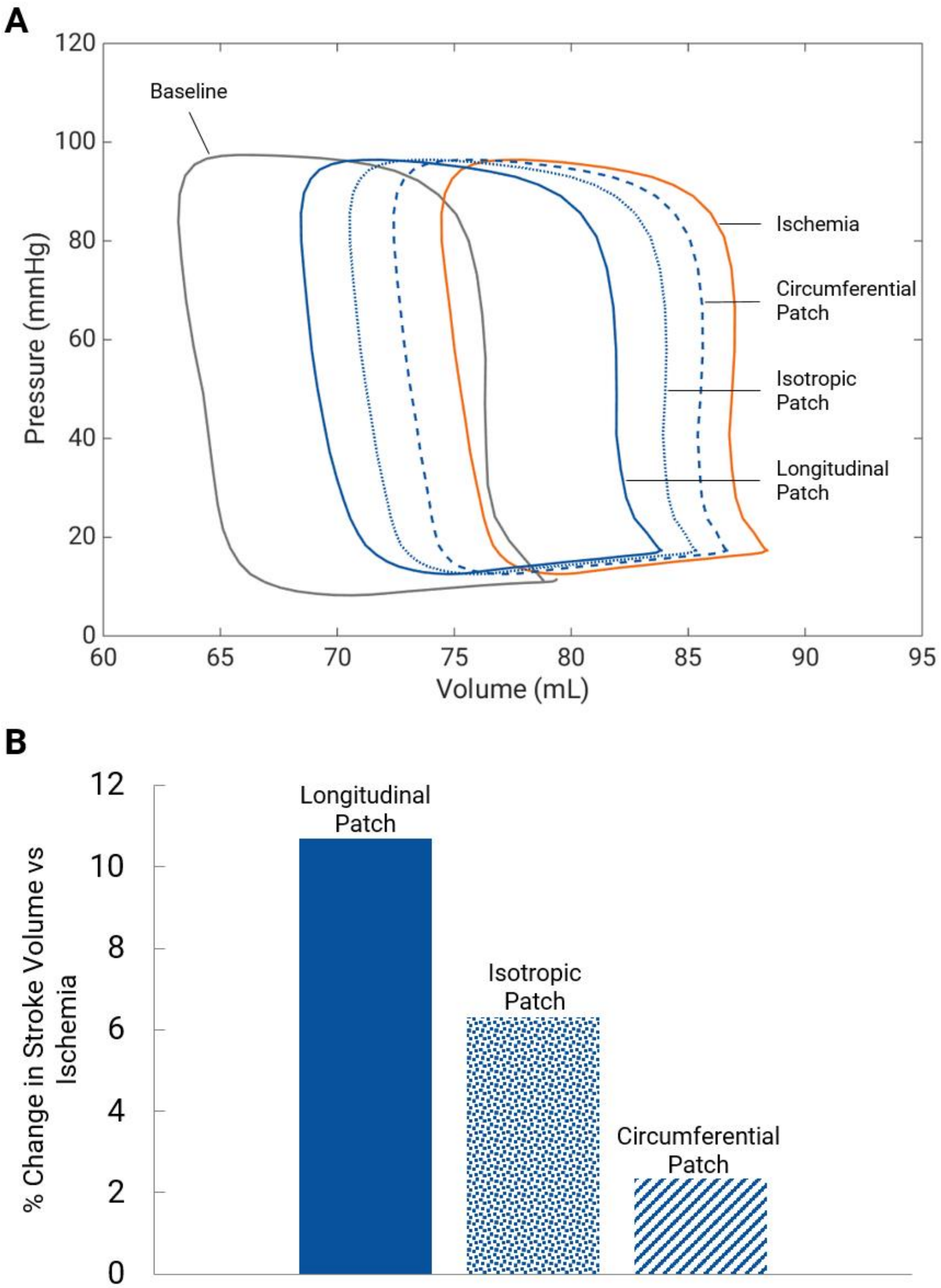

Figure 3.6 Simulations of different patch configurations: **A)** Pressure-volume loops for longitudinal, isotropic, and circumferential patch models, simulated using the same pressure loading and normalized contractility as the acute ischemia model. Baseline loop is shown for comparison. Longitudinal reinforcement leads to the greatest leftward shift in volumes compared to acute ischemia. **B)** Corresponding percent change in stroke volume (EDV-ESV) relative to ischemia for model simulations of longitudinal, isotropic, and circumferential patch reinforcement. Longitudinal reinforcement leads to the greatest increase in stroke volume compared to acute ischemia.

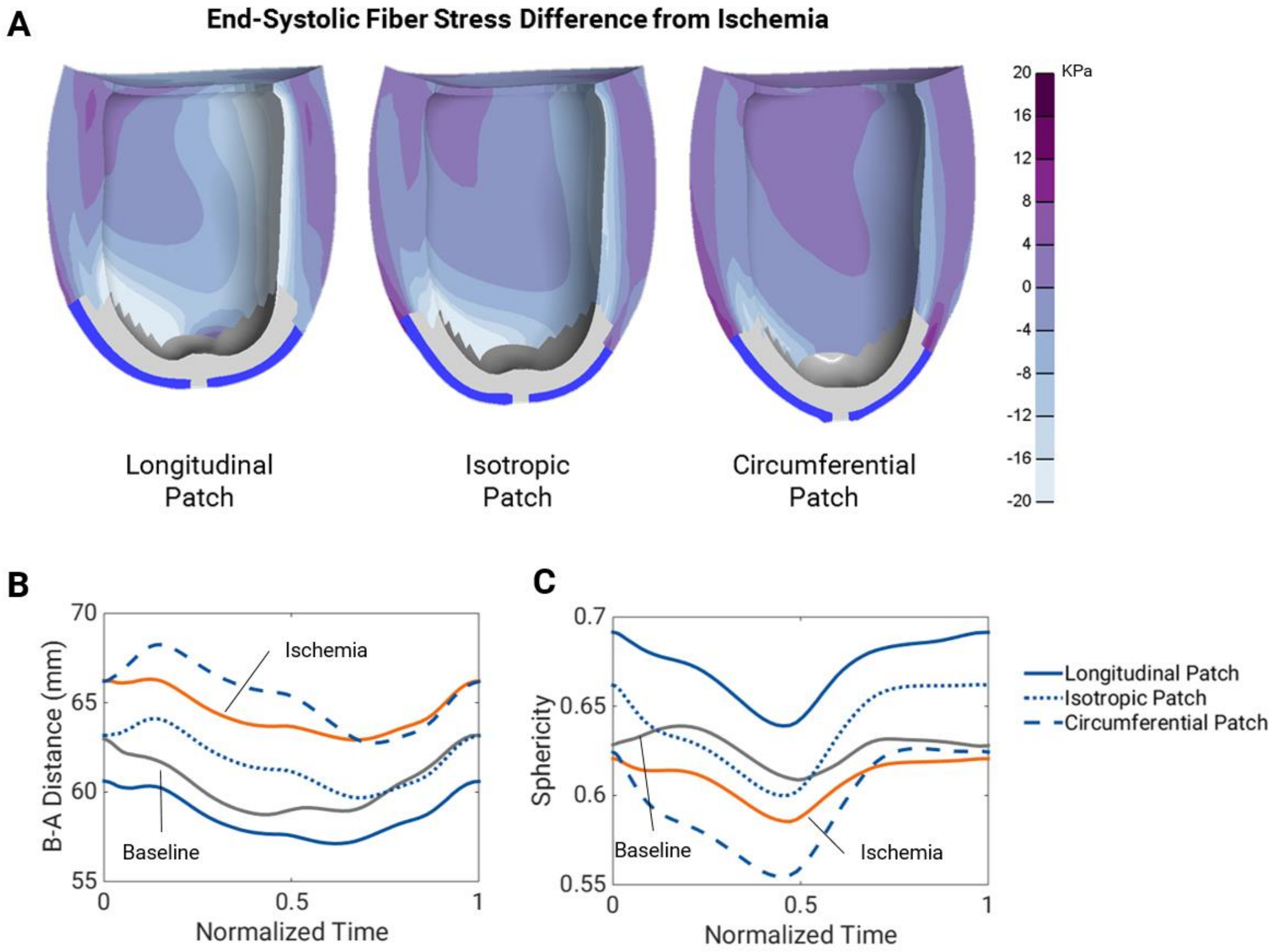

Figure 3.7 Stress and shape changes with different patch configurations: **A)** Longitudinal reinforcement decreases fiber stresses throughout much of the LV, particularly in the inner half of the wall, while transferring some stress to the outer half of the wall. Isotropic reinforcement produces a similar pattern but smaller reductions in fiber stress, while circumferential reinforcement increases fiber stresses in most of the wall. **B)** Acute ischemia increases the base-apex dimension and longitudinal reinforcement restores this dimension to normal. **C)** Longitudinal reinforcement leads to a more spherical shape throughout the cardiac cycle, while circumferential reinforcement produces a more elliptical shape.

DISCUSSION

The goal of this study was to construct a finite-element model that could match our previously published data on changes in regional strains and left ventricular function following longitudinal surgical reinforcement of large anteroapical infarcts in dogs [15], then use the model to explore potential mechanisms for the improvement in systolic function we observed. The model presented here, implemented in FEBio, matches all the key features of our experiments, including diastolic remodeling strains in the ischemic region, small shifts in the end-diastolic pressure-volume relationship (EDPVR), and large changes in the end-systolic pressure-volume relationship (ESPVR) in response to ischemia and to patch application. Detailed examination of model strains and stresses suggests that longitudinal reinforcement reduces peak diastolic fiber stretch and systolic fiber stress in the remote myocardium and shifts those peaks away from the endocardial surface, in part by reshaping the left ventricle (LV).

The most interesting finding of our original experiment was that longitudinal reinforcement had no significant effect on the end-diastolic behavior (as reflected in the EDPVR) but did shift the ESPVR leftward, increasing stroke volume under matched loading conditions (Figure 3.4). Therefore, after building and validating the finite-element model presented here, we next explored detailed plots of strains and stresses at both end diastole (ED) and end systole (ES). We found that while the end-diastolic pressures and volumes for the acute ischemia and patch-reinforcement models were fairly similar, patch reinforcement altered the ED transmural fiber stretch distribution more than we would have expected from the pressures and volumes alone. ED fiber stretch in the acute ischemia model was highest in the endocardial layer, and higher than baseline throughout at least the inner half of the wall, even in regions far from the infarct. By comparison to ischemia, ED fiber stretch in the patch model was lower overall and especially at the endocardium; patch reinforcement transferred the region of highest stretch to the midwall, where the fibers are circumferentially aligned (Figure 3.5). Plots of ES fiber stress showed very similar patterns, with the patch reducing high end-systolic stresses associated with acute ischemia throughout much of the left ventricular wall, particularly near the endocardium (Figures 3.5, 3.7). Based on these observations, we propose that longitudinal reinforcement improves systolic function primarily by reducing systolic fiber stress in the noninfarcted myocardium, allowing greater fiber shortening due to reduced regional afterload. Shifting peak diastolic fiber stretch and active stress generation away from the endocardium towards the midwall may have the added advantage of engaging more circumferentially oriented fibers that have more leverage in generating LV pressure and shortening. Because the endocardium is normally the layer with the highest mechanical work and the lowest blood flow [28], *in vivo* this shift could also improve function by transferring more of the mechanical work to areas with greater coronary perfusion reserve, an effect not captured in the model presented here.

Our model does not explicitly predict long-term effects of longitudinal reinforcement on left ventricular remodeling and the development of heart failure. However, in general we would expect that acute improvements in pump function would reduce sympathetic activation and other compensatory reflexes known to drive the development of post-infarction heart failure. Based on current theories about how regional mechanics drive myocyte remodeling, we would also anticipate that decreasing peak end-diastolic fiber stretch would decrease the direct mechanical stimulus for eccentric hypertrophy that leads to dilation of the ventricle and contributes to heart failure.

Prior models have consistently predicted that isotropic reinforcement of acute infarcts would reduce both diastolic and systolic volumes without improving stroke volume and cardiac output [17], [18]. We therefore performed a second set of simulations where we started with the fitted acute ischemia model presented here, held everything except material properties in the patch layer constant, and compared the effects of isotropic, circumferential, and longitudinal reinforcement (Figures 3.6, 3.7). These simulations showed that circumferential reinforcement produced the smallest predicted improvement in stroke volume and longitudinal reinforcement produced the largest, with isotropic reinforcement falling in the middle. These differences appeared to arise primarily through the effects of the different reinforcements on overall left ventricular shape. In the acute ischemia simulations, the large, relatively compliant anteroapical infarct caused the LV to take a more elliptical shape throughout the cycle. In contrast, the patch-reinforced model maintained a more spherical shape throughout the cycle, which enhances the increased fiber stretch in circumferentially aligned fibers. Interestingly, a more spherical shape is commonly associated with negative long-term outcomes [29]–[32], although the reasons for this are not completely understood. Longer-term simulations of growth and remodeling following each of these reinforcement cases could be an interesting follow-up to the current study.

One novel feature of the model presented here is particularly important for informing future computational models of myocardial ischemia and infarction. Like most if not all prior models of acute ischemia, we have previously assumed that acutely ischemic myocardium has the same passive properties as normal myocardium but lacks the ability to generate active stress [16]. Using this approach, diastolic strains at a matched pressure are by definition identical at baseline and during ischemia, so remodeling strains computed between those states are always zero. Yet in our experiments, we found remodeling strains on the order of 10% during acute ischemia, and additional remodeling of similar magnitude after applying the patch. Because these strains are nearly as large as the strains associated with systolic shortening in normal myocardium and systolic bulging in ischemic myocardium, we would argue that any model wishing to accurately capture the effects of an intervention designed to alter regional mechanics in the infarct must first account for this diastolic remodeling.

One other detail of our approach may be of interest to other groups building finite-element models of the heart. Rather than coupling our finite-element model to a model of the circulatory system, we simulated *in vivo* loading conditions by applying measured LV pressure vs. time curves to the model and iteratively adjusting a function that specified the time course of myocardial contractility (e(t) in Equation 3.5) until the model matched measured LV volume vs. time curves. This is conceptually similar to the approach used by Guccione and co-workers [33], [34] to estimate post-infarction regional contractility following infarction from regional strains. Stress generation in surviving myocardium might normally be expected to change following myocardial infarction due to sympathetic activation and related changes in calcium handling. However, our experimental data came from animals in which drugs were employed to block these responses. Thus, changes in regional stress generation in those animals could occur only through the Frank-Starling mechanism (increased force generation at longer sarcomere lengths). To the degree that our active contraction model accurately captures this length-dependent behavior, we should be able to fit pressure and volume data from the different runs with the same normalized contractility curve. This was only partially true in our simulations: the optimized contractility curves for the acute ischemia and longitudinal patch models were virtually identical, but peaked at a value about 50% greater than in the baseline model (Figure 3.3C). Given that EDP was lower at baseline, this may suggest that our active contraction model underestimates the magnitude of the Frank-Starling effect.

Our results may help influence design of new chronic reinforcement experiments, by identifying the design goal of redistributing transmural end-diastolic fiber stretch and maintaining an initially more spherical geometry. Our surgical approach to longitudinal reinforcement ultimately failed in a chronic animal trial, because the functional benefits faded progressively as scar compaction unloaded the patch [19]. However, other localized strategies, such as injection or epicardial delivery of biomaterials, [35]–[40] might be adapted to produce selective longitudinal reinforcement, or achieve a similar redistribution of fiber stresses through alternate mechanisms.

LIMITATIONS

Despite the close match between the models presented here and the corresponding experimental data, several limitations of our models should be acknowledged. First, we captured the diastolic remodeling observed during acute ischemia by reducing the passive stiffness of the ischemic myocardium. However, the exact mechanism by which the ischemic region appears to soften is not well understood. Loss of pressurization of the coronary vessels may reduce passive stiffness directly [23], but loss of coronary perfusion also leads to an immediate thinning of the wall and thus higher stresses and stretches at matched EDP [22], an effect that was not explicitly modeled here. Our model also differed from the experiments in the way we simulated patch reinforcement. While in the experiments the patch was sewn on the surface of the infarcted region, in our model we defined the epicardial elements of this region as the patch material. Lastly, our simulations of full cardiac cycles required optimizing distinct normalized contractility curves for each of our conditions in order to match the observed pressure-volume behavior. This approach is faster and simpler, but it is not as realistic as coupling the ventricular model to a model of the circulation [41]; as a result, the models generated here will not necessarily produce physiologically plausible pressure-volume behavior when loaded with different pressure vs. time curves.

CONCLUSION

In conclusion, we present here a new finite-element model of local anisotropic reinforcement of the canine left ventricle acutely post-infarction. Our model captures both local mechanics and global functional behavior in the average non-infarcted baseline, acutely ischemic, and patch reinforced dog throughout the cardiac cycle. Our model shows that longitudinal reinforcement of the ischemic region reduces peak fiber stretch and stress in surviving myocardium and redistributes diastolic fiber stretch and systolic fiber stress transmurally. Longitudinal reinforcement and functional improvement result in part from a reshaping of the heart towards a more spherical geometry.

REFERENCES

[1] E. J. Benjamin *et al.*, *Heart Disease and Stroke Statistics—2018 Update: A Report From the American Heart Association*. 2018.

[2] S. A. Clarke, R. K. Ghanta, G. Ailawadi, and J. W. Holmes, "Cardiac Restraint and Support Following Myocardial Infarction," Springer, Berlin, Heidelberg, 2013, pp. 169–206.

[3] R. C. Gorman, B. M. Jackson, J. A. Burdick, and J. H. Gorman, "Infarct Restraint to Limit Adverse Ventricular Remodeling," *J. Cardiovasc. Transl. Res.*, vol. 4, no. 1, pp. 73–81, Feb. 2011.

[4] A. A. Rane and K. L. Christman, "Biomaterials for the Treatment of Myocardial Infarction," *J. Am. Coll. Cardiol.*, vol. 58, no. 25, pp. 2615–2629, Dec. 2011.

[5] M. N. Hirt, A. Hansen, and T. Eschenhagen, "Cardiac Tissue Engineering," *Circ. Res.*, vol. 114, no. 2, pp. 354–367, Jan. 2014.

[6] M. C. Oz *et al.*, "Global surgical experience with the Acorn cardiac support device.," *J. Thorac. Cardiovasc. Surg.*, vol. 126, no. 4, pp. 983–91, Oct. 2003.

[7] J. M. Power *et al.*, "Passive ventricular constraint amends the course of heart failure: a study in an ovine model of dilated cardiomyopathy.," *Cardiovasc. Res.*, vol. 44, no. 3, pp. 549–55, Dec. 1999.

[8] P. A. Chaudhry *et al.*, "Passive epicardial containment prevents ventricular remodeling in heart failure.," *Ann. Thorac. Surg.*, vol. 70, no. 4, pp. 1275–80, Oct. 2000.

[9] J. J. Pilla *et al.*, "Early Postinfarction Ventricular Restraint Improves Borderzone Wall Thickening Dynamics During Remodeling," *Ann. Thorac. Surg.*, vol. 80, no. 6, pp. 2257–2262, Dec. 2005.

[10] A. S. Blom *et al.*, "Cardiac Support Device Modifies Left Ventricular Geometry and Myocardial Structure After Myocardial Infarction," *Circulation*, vol. 112, no. 9, pp. 1274–1283, Aug. 2005.

[11] A. S. Blom *et al.*, "Ventricular Restraint Prevents Infarct Expansion and Improves Borderzone Function After Myocardial Infarction: A Study Using Magnetic Resonance Imaging, Three-Dimensional Surface Modeling, and Myocardial Tagging," *Ann. Thorac. Surg.*, vol. 84, no. 6, pp. 2004–2010, Dec. 2007.

[12] S. T. Kelley *et al.*, "Restraining infarct expansion preserves left ventricular

geometry and function after acute anteroapical infarction.," *Circulation*, vol. 99, no. 1, pp. 135–42.

[13] S. L. Moainie *et al.*, "Infarct restraint attenuates remodeling and reduces chronic ischemic mitral regurgitation after postero-lateral infarction.," *Ann. Thorac. Surg.*, vol. 74, no. 2, pp. 444–9; discussion 449, Aug. 2002.

[14] W. J. Richardson, S. A. Clarke, T. A. Quinn, and J. W. Holmes, "Physiological Implications of Myocardial Scar Structure," in *Comprehensive Physiology*, Hoboken, NJ, USA: John Wiley & Sons, Inc., 2015, pp. 1877–1909.

[15] G. M. Fomovsky, S. A. Clark, K. M. Parker, G. Ailawadi, and J. W. Holmes, "Anisotropic reinforcement of acute anteroapical infarcts improves pump function," *Circ. Hear. Fail.*, vol. 5, no. 4, pp. 515–522, 2012.

[16] G. M. Fomovsky, J. R. MacAdangdang, G. Ailawadi, and J. W. Holmes, "Model-based design of mechanical therapies for myocardial infarction," *J. Cardiovasc. Transl. Res.*, vol. 4, no. 1, pp. 82–91, 2011.

[17] D. K. Bogen, S. A. Rabinowitz, A. Needleman, T. A. McMahon, and W. H. Abelmannj, "An analysis of the mechanical disadvantage of myocardial infarction in the canine left ventricle," *Circ Res*, vol. 47, no. 5, pp. 728–741, 1980.

[18] S. T. Wall, J. C. Walker, K. E. Healy, M. B. Ratcliffe, and J. M. Guccione, "Theoretical impact of the injection of material into the myocardium: A finite element model simulation," *Circulation*, vol. 114, no. 24, pp. 2627–2635, 2006.

[19] S. A. Clarke, N. C. Goodman, G. Ailawadi, and J. W. Holmes, "Effect of Scar Compaction on the Therapeutic Efficacy of Anisotropic Reinforcement Following Myocardial Infarction in the Dog," *J. Cardiovasc. Transl. Res.*, vol. 8, no. 6, pp. 353–361, 2015.

[20] S. L. Herz, C. M. Ingrassia, S. Homma, K. D. Costa, and J. W. Holmes, "Parameterization of left ventricular wall motion for detection of regional ischemia," *Ann. Biomed. Eng.*, vol. 33, no. 7, pp. 912–919, 2005.

[21] D. D. Streeter and W. T. Hanna, "Engineering mechanics for successive states in canine left ventricular myocardium. II. Fiber angle and sarcomere length," *Circ. Res.*, vol. 33, no. 6, pp. 656–664, 1973.

[22] J. W. Holmes, T. K. Borg, and J. W. Covell, "Structure and Mechanics of Healing Myocardial Infarcts," *Annu. Rev. Biomed. Eng.*, vol. 7, no. 1, pp. 223–253, 2005.

[23] K. May-Newman, J. H. Omens, R. S. Pavelec, and A. D. McCulloch, “Three-dimensional transmural mechanical interaction between the coronary vasculature and passive myocardium in the dog,” *Circ. Res.*, vol. 74, no. 6, pp. 1166–1178, 1994.

[24] J. D. Humphrey, R. K. Strumpf, and F. C. P. Yin, “Determination of a constitutive relation for passive myocardium: I. A new functional form,” *J. Biomech. Eng.*, vol. 112, no. 3, pp. 333–339, 1990.

[25] G. A. Holzapfel and R. W. Ogden, “Constitutive modelling of passive myocardium: A structurally based framework for material characterization,” *Philos. Trans. R. Soc. A Math. Phys. Eng. Sci.*, vol. 367, no. 1902, pp. 3445–3475, Sep. 2009.

[26] J. M. Guccione, L. K. Waldman, and A. D. McCulloch, “Mechanics of Active Contraction in Cardiac Muscle: Part II—Cylindrical Models of the Systolic Left Ventricle,” *J. Biomech. Eng.*, vol. 115, no. 1, pp. 82–90, Feb. 1993.

[27] P. J. Hunter, A. D. McCulloch, and H. E. ter Keurs, “Modelling the mechanical properties of cardiac muscle.,” *Prog. Biophys. Mol. Biol.*, vol. 69, no. 2–3, pp. 289–331, 1998.

[28] J. Ross, “Myocardial perfusion-contraction matching. Implications for coronary heart disease and hibernation.,” *Circulation*, vol. 83, no. 3, pp. 1076–83, Mar. 1991.

[29] G. A. Lamas, D. E. Vaughan, A. F. Parisi, and M. A. Pfeffer, “Effects of left Ventricular Shape and Captopril Therapy on Exercise Capacity After Anterior Wall Acute Myocardial Infarction,” *Am. J. Cardiol.*, vol. 63, no. 17, pp. 1167–1173, 1989.

[30] G. F. Mitchell, G. A. Lamas, D. E. Vaughan, and M. A. Pfeffer, “Left ventricular remodeling in the year after first anterior myocardial infarction: A quantitative analysis of contractile segment lengths and ventricular shape,” *J. Am. Coll. Cardiol.*, vol. 19, no. 6, pp. 1136–1144, 1992.

[31] S. P. Wong *et al.*, “Relation of left ventricular sphericity to 10-year survival after acute myocardial infarction,” *Am. J. Cardiol.*, vol. 94, no. 10, pp. 1270–1275, 2004.

[32] M. A. Pfeffer and E. Braunwald, “Ventricular Remodeling After Myocardial Infarction Experimental Observations and Clinical Implications,” *Circulation*, vol. 81, no. 4, pp. 1161–1172, 1990.

[33] K. Sun *et al.*, “A Computationally Efficient Formal Optimization of

Regional Myocardial Contractility in a Sheep With Left Ventricular Aneurysm," *J. Biomech. Eng.*, vol. 131, no. 11, p. 111001, Oct. 2009.

[34] J. F. Wenk *et al.*, "Regional Left Ventricular Myocardial Contractility and Stress in a Finite Element Model of Posterobasal Myocardial Infarction," *J. Biomech. Eng.*, vol. 133, no. 4, p. 044501, Apr. 2011.

[35] J. L. Ifkovits *et al.*, "Injectable hydrogel properties influence infarct expansion and extent of postinfarction left ventricular remodeling in an ovine model," *Proc. Natl. Acad. Sci.*, vol. 107, no. 25, pp. 11507–11512, 2010.

[36] R. Mukherjee *et al.*, "Targeted Myocardial Microinjections of a Biocomposite Material Reduces Infarct Expansion in Pigs," *Ann. Thorac. Surg.*, vol. 86, no. 4, pp. 1268–1276, 2008.

[37] K. L. Fujimoto *et al.*, "Synthesis, characterization and therapeutic efficacy of a biodegradable, thermoresponsive hydrogel designed for application in chronic infarcted myocardium," *Biomaterials*, vol. 30, no. 26, pp. 4357–4368, 2009.

[38] J. Leor *et al.*, "Intracoronary Injection of In Situ Forming Alginate Hydrogel Reverses Left Ventricular Remodeling After Myocardial Infarction in Swine," *J. Am. Coll. Cardiol.*, vol. 54, no. 11, pp. 1014–1023, 2009.

[39] J. R. Garcia *et al.*, "A Minimally Invasive, Translational Method to Deliver Hydrogels to the Heart Through the Pericardial Space," *JACC Basic to Transl. Sci.*, vol. 2, no. 5, pp. 601–609, 2017.

[40] W. Whyte *et al.*, "Sustained release of targeted cardiac therapy with a replenishable implanted epicardial reservoir," *Nat. Biomed. Eng.*, vol. 2, no. 6, pp. 416–428, 2018.

[41] R. C. P. Kerckhoffs, M. L. Neal, Q. Gu, J. B. Bassingthwaighte, J. H. Omens, and A. D. McCulloch, "Coupling of a 3D finite element model of cardiac ventricular mechanics to lumped systems models of the systemic and pulmonic circulation.," *Ann. Biomed. Eng.*, vol. 35, no. 1, pp. 1–18, Jan. 2007.

CHAPTER 4:

MULTISCALE COMPUTATIONAL MODELING OF CARDIAC CONCENTRIC HYPERTROPHY

INTRODUCTION

Left ventricular hypertrophy is complex in nature and involves an array of mechanical and hormonal changes that stimulate growth and remodeling of the heart. In particular, both aortic stenosis and hypertension lead to an increase in afterload and subsequent left ventricular concentric hypertrophy, a thickening of the walls that increases the contractile ability of the heart and reduces wall stress [1], [2]. However, development of left ventricular hypertrophy is also associated with increased risk of further cardiovascular disease, heart failure, and mortality [3]–[6]. Current treatment options for aortic stenosis and hypertension involve management of afterload and ideally a reduction in hypertrophy. For example, aortic stenosis is treated through surgical repair or replacement of the stenotic valves, which can lead to improved cardiac function and even reversal of hypertrophy. However, clinical decisions for aortic stenosis are not always straightforward, because the benefit of these interventions must be weighed against the risk of surgical complications on a patient-by-patient basis [7]–[10]. In the case of hypertension, current treatment options for most patients include lifestyle changes and drugs, such as β-blockers, angiotensin-converting enzyme (ACE) inhibitors, and angiotensin receptor blockers (ARBs), but given the prevalence of the disease there is still a need for identifying new therapies to treat or prevent the associated hypertrophy. The long-term goal of the work described here is to develop computational models that predict the progression of hypertrophy in the setting of increased afterload, altered hormonal levels, and the presence of pharmacological interventions, in order to better understand the underlying processes, develop new treatment strategies, and guide clinical decision making.

Several experimental methods, pharmacological and mechanical, are used to induce concentric hypertrophy in animals; here, we use data from two models to construct and validate growth models. Infusion of isoproterenol, an FDA-approved β-adrenergic receptor agonist normally used to treat bradycardia and heart block, induces cardiac hypertrophy and fibrosis through activation of the β-1 adrenergic receptor and subsequent increases in G-protein signaling and cAMP [11], [12]. Because it is not present as an endogenous hormone, isoproterenol infusion provides a straightforward way to study the development of cardiac hypertrophy and specific interventions that can attenuate growth. By contrast, in transverse aortic constriction (TAC), a pressure overload is created by tying a suture around the aorta that constricts the vessel. The pressure overload caused by TAC induces concentric hypertrophy both directly through mechanical stimulation and indirectly through increases in circulating hormones such as endothelin-1 (ET-1) and norepinephrine (NE) and activation of the renin-angiotensin system, which leads to elevated levels of angiotensin II (Ang II) and atrial natriuretic peptide (ANP) [1], [13], [22], [23], [14]–[21]. These hormones in turn activate pro-hypertrophic pathways in cardiomyocytes and further exacerbate the growth experienced by the heart. While TAC remains artificial in terms of its sudden onset, it recreates features of the complex hormonal and mechanical stimulation associated with diseases such as aortic stenosis and hypertension.

Computational growth modeling is an evolving area of biomechanics aimed at predicting the growth of biological tissues in response to their mechanical environment. Most computational growth models of the heart use phenomenologic equations to predict growth based on mechanical stimuli such as stretch and stress, and some of those models have proven successful at predicting the different patterns of myocyte thickening and lengthening that occur in response to both experimental volume overload and pressure overload [24]–[26]. However, the main limitation of phenomenologic growth laws based on mechanical stimuli is that they are unable to predict how hormones and pharmacologic interventions will influence the amount of growth experienced by the heart. This limitation is especially problematic for models that aim to predict clinical outcomes, because nearly all patients with clinically significant cardiac disease receive drugs such as β-blockers, ACE inhibitors, and ARBs that can alter hypertrophic signaling. However, techniques from the field of systems biology now offer the possibility to model large signaling networks within a cell and predict how cell growth and gene expression are altered by specific perturbations. Ryall et al. [27] published a model of hypertrophic signaling within a single cardiomyocyte and used it to predict increases in cell area in response to both mechanical stretch and hormonal agonists and to identify key intracellular signaling hubs for this process. A more recent version, published by Frank et al. [28], further refined and validated the network model against *in vivo* data from 52 transgenic mouse models.

The purpose of the current study was to construct a multiscale model of cardiac hypertrophy that connects a finite-element model (FEM) representing the mechanics of the growing left ventricle to the cell-level hypertrophy signaling network model. In the present work, we test the ability of the multiscale model to predict *in vivo* growth due to isoproterenol infusion (hormones only), TAC (mechanical overload and hormones), and different genetic and pharmacologic interventions that attenuate hypertrophy in TAC (mechanical overload, hormones, and hormonal perturbations).

METHODS

Finite-element model simulations

We used a previously published finite-element model of the left ventricle as the basis for our multiscale model of hypertrophy [29]. Briefly, the finite-element model was constructed from average endocardial and epicardial surface contours obtained by segmenting and averaging magnetic resonance (MRI) scans of a set of canine left ventricles from a previous study [30]. The mesh consisted of 9680 nodes and 7840 linear elements, including rigid-body rings of elements at the base and apex. The finite-element model had five transmural layers, with a fiber distribution of -60° to 60° from epicardium to endocardium. For this study the model used the compressible transversely isotropic Mooney-Rivlin (TIMR) material in FEBio 2.6.4 (febio.org), with growth capabilities added in a custom plugin, described below. We simulated full cardiac cycles by prescribing the applied internal cavity pressure and a time-varying activation curve that represents the rise and fall of active tension generation in the myocardium due to calcium cycling [29]. The basal rigid body ring was fixed in all directions, the basal-most nodes were fixed in the base-apex direction, and all other elements were allowed to move freely during the simulation. We defined the baseline and acute pressure overload conditions by using a previously published cardiac compartmental model [31] to calculate the cavity pressure-vs-time and activation curves. The end-diastolic and end-systolic pressure-volume relationships from the finite-element model served as inputs to the compartmental model, which then calculated a baseline pressure-volume (PV) loop and a pressure overloaded PV loop. In the isoproterenol simulations, we used the baseline PV loop throughout the simulation, consistent with a previous study [32] showing little difference in the pressure vs. time curves of sham and isoproterenol-induced mice at doses shown to result in hypertrophy. For all TAC simulations we instead used the pressure overloaded PV loop. Changes to the hormonal activation during isoproterenol infusion and TAC were represented as global changes present throughout the simulation. All finite-element model simulations were run using the Pardiso solver in FEBio 2.6.4.

Growth implementation

To allow growth in the finite-element framework, we implemented the kinematic growth framework proposed by Rodriguez et al. [33] using a custom FEBio plugin that redefined the stress in the material to depend on the elastic rather than total deformation. The plugin added a user-defined diagonal growth deformation tensor ($\mathbf{F}_{\text{growth}}$) with fiber, cross-fiber, and radial components (Equation 4.1) and a user-defined radial direction vector in addition to the fiber direction already defined in the TIMR material. Using a multiplicative decomposition, we calculated the elastic deformation ($\mathbf{F}_{\text{elastic}}$) within the plugin from the total deformation ($\mathbf{F}_{\text{total}}$) applied to the model and the user-defined growth deformation tensor (Equation 4.2). We used the compressible TIMR material as the template for our growth plugin, and within its FEBio material file, we redefined the matrix, fiber, and dilatational components of the stress (Equation 4.3) to depend on our calculated elastic deformation. Thus, stress became a function of the elastic deformation rather than the total deformation. The growth framework and plugin implementation are discussed in more detail in Chapter 2.

$$\boldsymbol{F}_{growth} = \begin{bmatrix} F_{growth,ff} & 0 & 0 \\ 0 & F_{growth,cc} & 0 \\ 0 & 0 & F_{growth,rr} \end{bmatrix} \tag{4.1}$$

$$\boldsymbol{F}_{elastic} = \boldsymbol{F}_{growth}^{-1}\boldsymbol{F}_{total} \tag{4.2}$$

$$\boldsymbol{\sigma}_{Matrix} = \frac{2}{J_{elastic}}\Big(\boldsymbol{B}_{elastic}(c_1 + I_{elastic1}c_2) - \boldsymbol{B}_{elastic}{}^2 c_2 - \boldsymbol{I}(c_1 + 2c_2)\Big)$$

$$\boldsymbol{\sigma}_{Fiber} = \boldsymbol{A}_{elastic}\frac{1}{J_{elastic}}c_3\left(e^{c_4(\lambda_{elastic}-1)} - 1\right) \tag{4.3}$$

$$\boldsymbol{\sigma}_{Dilatational} = K\frac{\ln(J_{elastic})}{J_{elastic}}\boldsymbol{I}$$

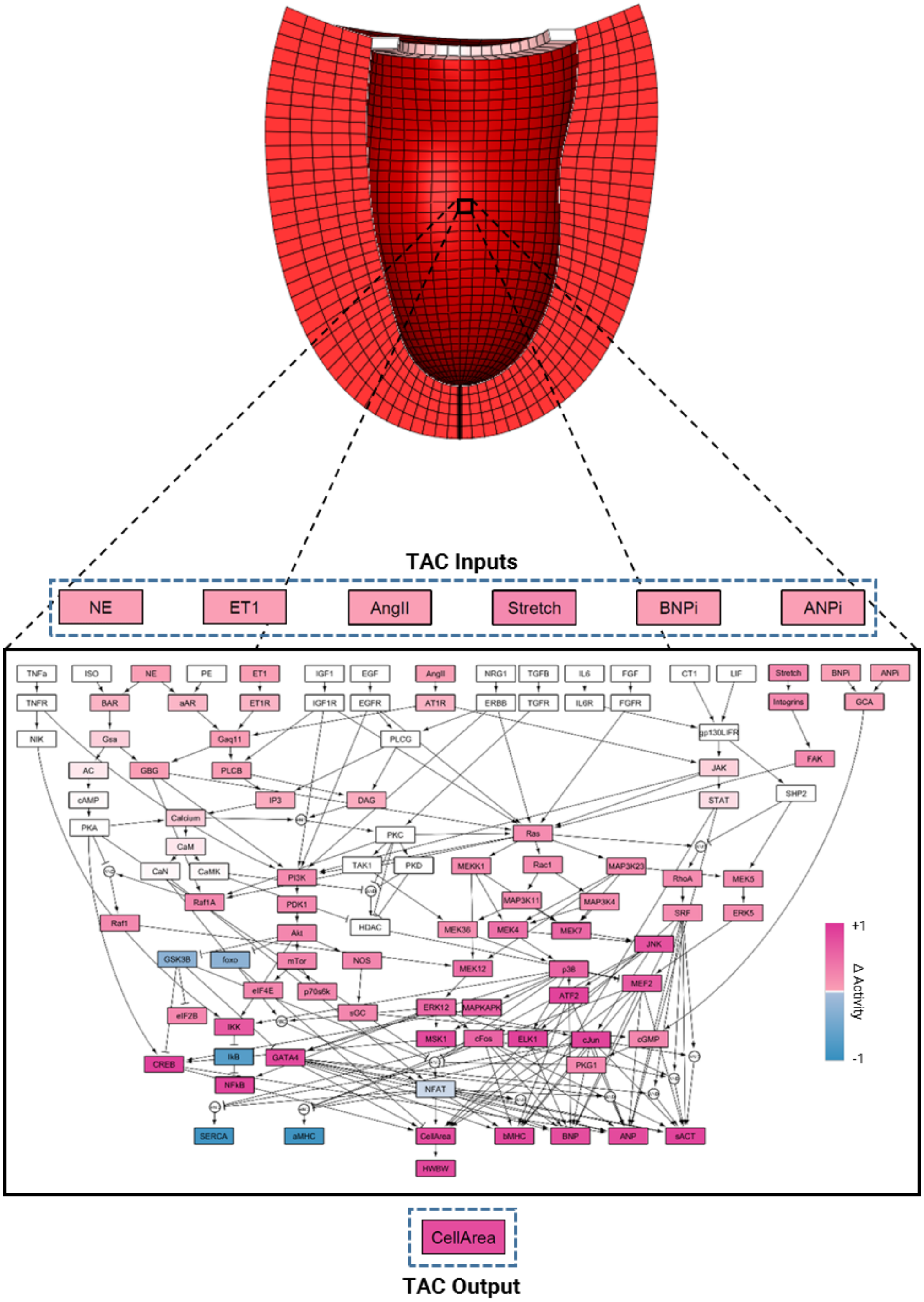

Figure 4.1 Schematic of the multiscale model of hypertrophy. A finite-element model of the left ventricle is coupled to a network model of intracellular hypertrophy signaling in cardiomyocytes. The network model shows the change in activation of each node in response to simulated transverse aortic constriction (TAC) compared to baseline activation. Increased activation is shown in pink and decreased activation is shown in blue.

Coupling the network and mechanical models

We built a multiscale model of hypertrophy by coupling an existing cardiomyocyte hypertrophy signaling network model to the finite-element model of the left ventricle, as shown in Figure 4.1, via MATLAB (R2014b, Mathworks). The hypertrophy signaling network model [27], [28] consisted of a system of normalized Hill-type ordinary differential equations with 107 species and 207 reactions that capture the intracellular signaling leading to increases in cell size and protein production necessary for hypertrophy. Examples of the differential equations for a model input node A and for an activated downstream node B are shown in Equation 4.4 and in Equations 4.5-4.8, respectively. In these equations, *W* corresponds to the weight of the reaction, a measure of the extent to which the reaction can activate or inhibit its downstream nodes, and y_{max} to the maximum activation possible for each particular node. By default, all nodes used $y_{max} = 1$ and Hill-function parameters $n = 1.4$ and $EC_{50} = 0.5$, as used previously [27], [28]. The model used a time constant $\tau = 0.1$ hrs for all nodes except for the outputs α-myosin heavy chain (aMHC), atrial natriuretic peptide (ANP), β-myosin heavy chain (bMHC), brain natriuretic peptide (BNP), skeletal α-actin (sACT), sarcoplasmic reticulum ATPase (SERCA), and Cell Area, all of which were initially set to 1 hr. Default node weights were set to 0.06 for all input nodes except isoproterenol, 0 for isoproterenol, and 1 for downstream nodes. All species in the network model had a value range of 0 to 1.

$$\frac{dA}{dt} = \frac{1}{\tau_A}(W_A y_{max,A} - A) \tag{4.4}$$

$$\frac{dB}{dt} = \frac{1}{\tau_B}(W_{AB} f_{act}(A) y_{max,B} - B) \tag{4.5}$$

$$f_{act}(X) = \frac{\beta X^n}{K^n + X^n} \tag{4.6}$$

$$\beta = \frac{EC_{50}^n - 1}{2EC_{50}^n - 1} \tag{4.7}$$

$$K = (\beta - 1)^{\frac{1}{n}} \tag{4.8}$$

For each growth step in the multiscale model, we ran the network model to simulate 5 hours of real time, sampled the cell area output, and used it to drive an increase in mass. Then, in the FEM, we applied the analogous growth deformation and calculated the corresponding elastic deformation. For the growth deformation, a value > 1 corresponds to positive growth or thickening, while values < 1 correspond to atrophy or thinning. For the concentric growth simulations presented here, we assumed that all growth would occur in the radial direction. We then sampled the elastic deformation from the FEM and used it to update the stretch input to the network model, then iterated to the next growth step. To account for the differences in value ranges when coupling the model inputs and outputs, we defined linear mapping functions as described in the following section. The multiscale model coupling process is summarized in Figure 4.2.

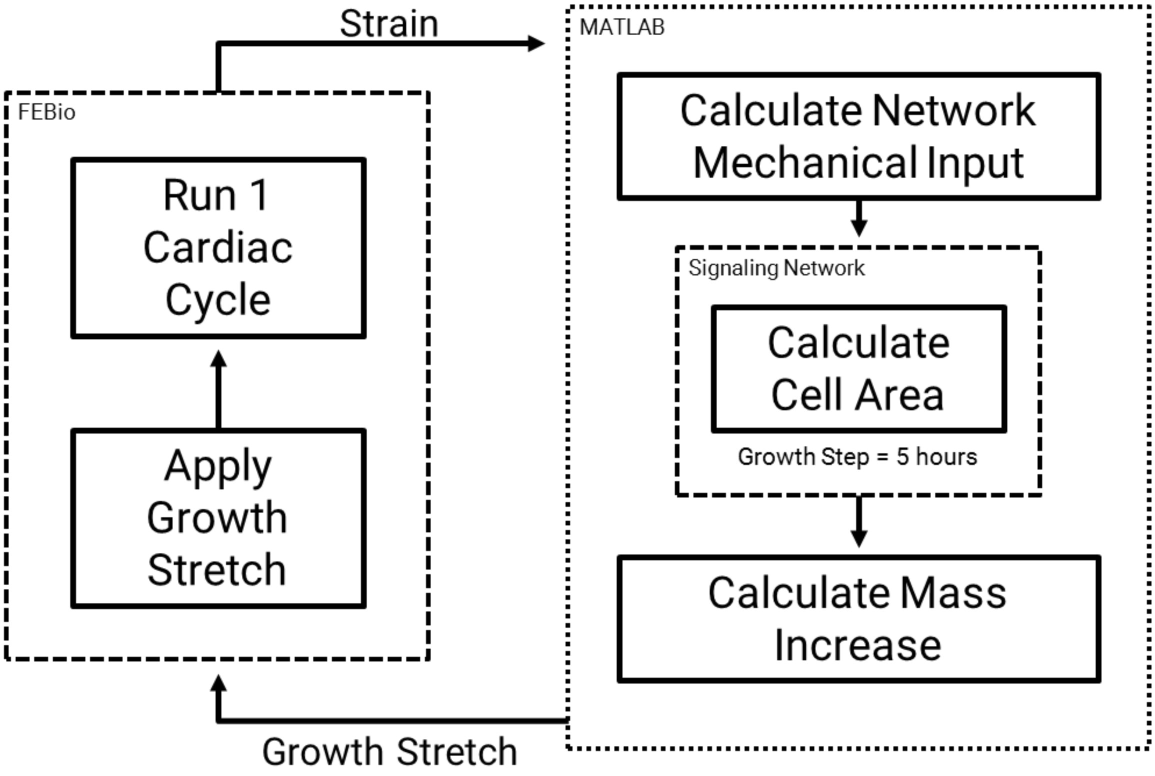

Figure 4.2 Multiscale model coupling process. We apply the growth stretch to the FEM in FEBio and run one cardiac cycle. We then parse the elastic deformation from the FEM in MATLAB and use it to calculate the network mechanical input. We run the network model for a simulated 5 hour growth step and sample the cell area, which we use to calculate the mass increase and growth stretch for the FEM.

Simulating isoproterenol infusion, TAC, and interventions

We simulated four types of conditions using the multiscale model: isoproterenol infusion, TAC, TAC in genetic knock-out animals, and TAC with pharmacologic interventions. All network input nodes had an initial baseline value of 0.06, corresponding to their node weight, with the exception of the isoproterenol input node (ISO), which was set to zero because it is not an endogenous ligand. For our mechanical stimulus, we used the minimum of the greatest principal cross-fiber strain (min($E_{cross,max}$)) during the cardiac cycle, a metric proposed by Kerckhoffs et al. [24] to drive thickening of the myocardium. We averaged the min($E_{cross,max}$) values across all finite elements in the FEM and mapped them to the normalized network model stretch input so that the min($E_{cross,max}$) in acute pressure overload would stimulate a half-maximal increase in cell area, while the baseline min($E_{cross,max}$) would correspond to the initial network model input of 0.06. This choice was motivated by the fact that the pressure gradients imposed in the studies modeled here fell in the middle of the range of severities of TAC known to induce graded hypertrophic responses [34]. The final stretch mapping function is shown in Equation 4.9.

$$Stretch_{Net} = 2.0250\left(min\left(E_{cross,max}\right)\right) - 0.0843 \tag{4.9}$$

The amount of growth predicted by the multiscale model is calculated using a linear mapping between the network cell area output and a mass fold change corresponding to the determinant of the growth deformation, J_{growth}. The value of J_{growth} is then applied as the growth in the radial direction, such that $F_{growth,rr}$ = Mass. We gathered mass increase data reported in the literature for both isoproterenol infusion and TAC [19], [23], [42]–[51], [32], [52], [35]–[41] and tuned our mapping based on these data. For the isoproterenol infusion simulations, we increased the activation level of the ISO input node only, with all other hormonal inputs and baseline stretch kept constant. We simulated TAC by increasing the stretch to the pressure overload level and uniformly increasing the levels of the hormonal inputs angiotensin II (AngII), endothelin-1 (ET1), norepinephrine (NE), atrial natriuretic peptide (ANPi), and brain natriuretic peptide (BNPi). We chose a level of hormonal activation of 0.09, which resulted in a cell area of 0.6383, approximately a half-maximal increase in cell area from baseline. We based this choice on data reporting additional increases in the hemodynamic response to β-adrenergic stimulation in TAC animals [47]. Using an analytic model to test hormone activation levels, we found that an activation level of at least 0.09 was necessary to capture a substantial attenuation of growth by TAC genetic knock-out interventions, described in the following section, while at higher activation levels the growth attenuation by a NE knock-out intervention is reduced (Figure 4.3). We then defined the average mass increase due to TAC at two weeks, 1.45, [19], [23], [52], [35], [45]–[51] to correspond to this cell area value. Based on data showing that even maximal doses of isoproterenol produce a lower steady-state mass increase than TAC in murine experiments (1.33) [32], [35], [44], [53], [36]–[43], we set the maximum activation (y_{max}) of ISO to 0.132 which results in a maximal cell area value of 0.5253. The final growth mapping function is presented in Equation 4.10. In order to capture the correct time course for both ISO and TAC simulations, we set the time constants τ = 50 hrs for the Cell Area node and τ = 1 hr for the ISO node. Based on the experimental data, we simulated two weeks of growth for both isoproterenol infusion and TAC.

$$Mass = 1.0744(CellArea) + 0.7642 \tag{4.10}$$

Finally, we simulated TAC-induced hypertrophy experiments in several genetically modified animals [19], [45] and with selected pharmacologic interventions [49]–[52]. To simulate an inhibition, a knock-out, or a blockade in the network model, we set the maximum activation (y_{max}) of the node of interest to zero, preventing any level of activation. We then repeated TAC simulations using the same mechanical and hormonal inputs. We chose to simulate a transgenic Gq-coupled receptor inhibitor overexpression, GqI, which would prevent activation of the Gαq11 network node [45]; an endogenous NE knock-out (NE KO), which would prevent the effect of the NE network node [19]; the angiotensin II receptor blocker losartan (ARB), which would block the AT1R network node [49]–[51]; and the β-blocker propranolol, which would block the βAR network node [52]. The GqI and NE KO interventions each used a version of the network model with their respective modifications to obtain initial steady-state network conditions, before TAC is induced, and continued to use the modified networks throughout the simulation. The ARB and β-blocker interventions instead used the baseline network, before interventions, to obtain initial steady-state conditions and then applied the appropriate modifications once TAC was induced. These choices were based on the idea that the genetic modifications would be present throughout the life of the mice, before TAC, while the pharmacologic perturbations would only be introduced as a therapy after TAC was induced.

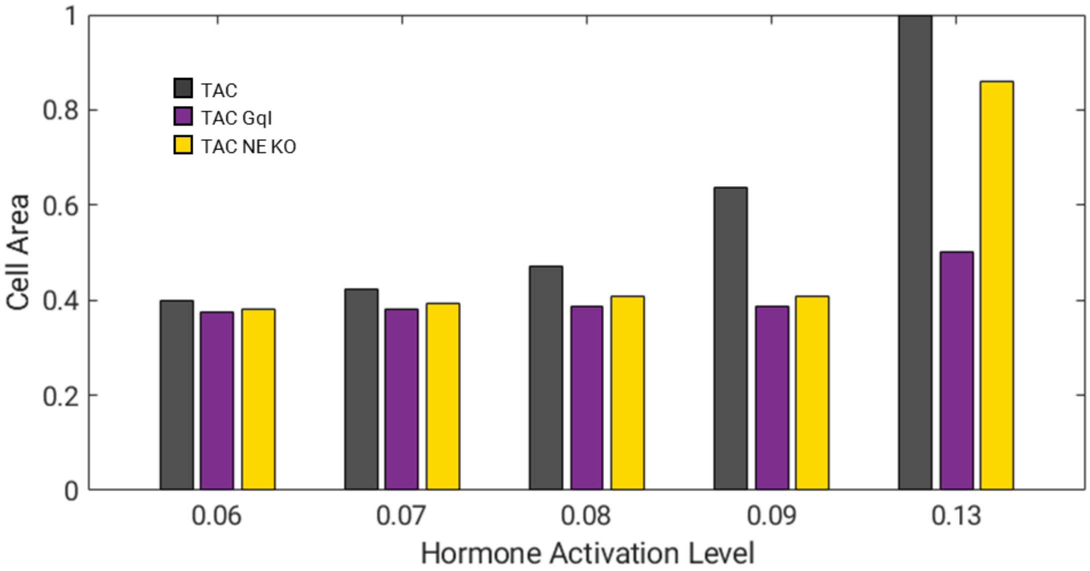

Figure 4.3 Effect of hormone activation level on final cell area due to TAC and two genetic interventions, GqI and NE KO, evaluated using an analytic model. An activation level of 0.09 was necessary to capture a substantial attenuation of growth by TAC genetic knock-out interventions, while an activation of 0.13, which induces a maximum cell area value, reduced the growth attenuation caused by the NE KO intervention.

RESULTS

Multiscale simulations of isoproterenol infusion and TAC

We simulated two weeks of isoproterenol infusion using the multiscale model. All network hormonal inputs aside from isoproterenol were kept at a constant baseline value of 0.06. The mechanical input started at a baseline level but was allowed to evolve in response to growth, and the isoproterenol input was maintained at the maximum value of 1 throughout the simulation. As seen in Figure 4.4A, the simulation predicted a steady-state mass increase of 1.33 fold with a time course consistent with published data from experimental studies of isoproterenol infusion in mice [32], [35], [44], [53], [36]–[43]. Figure 4.4B shows long-axis and short-axis cross-sections of the baseline left ventricle and the left ventricle after two weeks of isoproterenol infusion, both at end diastole. These cross-sections show the substantial thickening of the left-ventricular walls, consistent with the growth patterns in concentric hypertrophy.

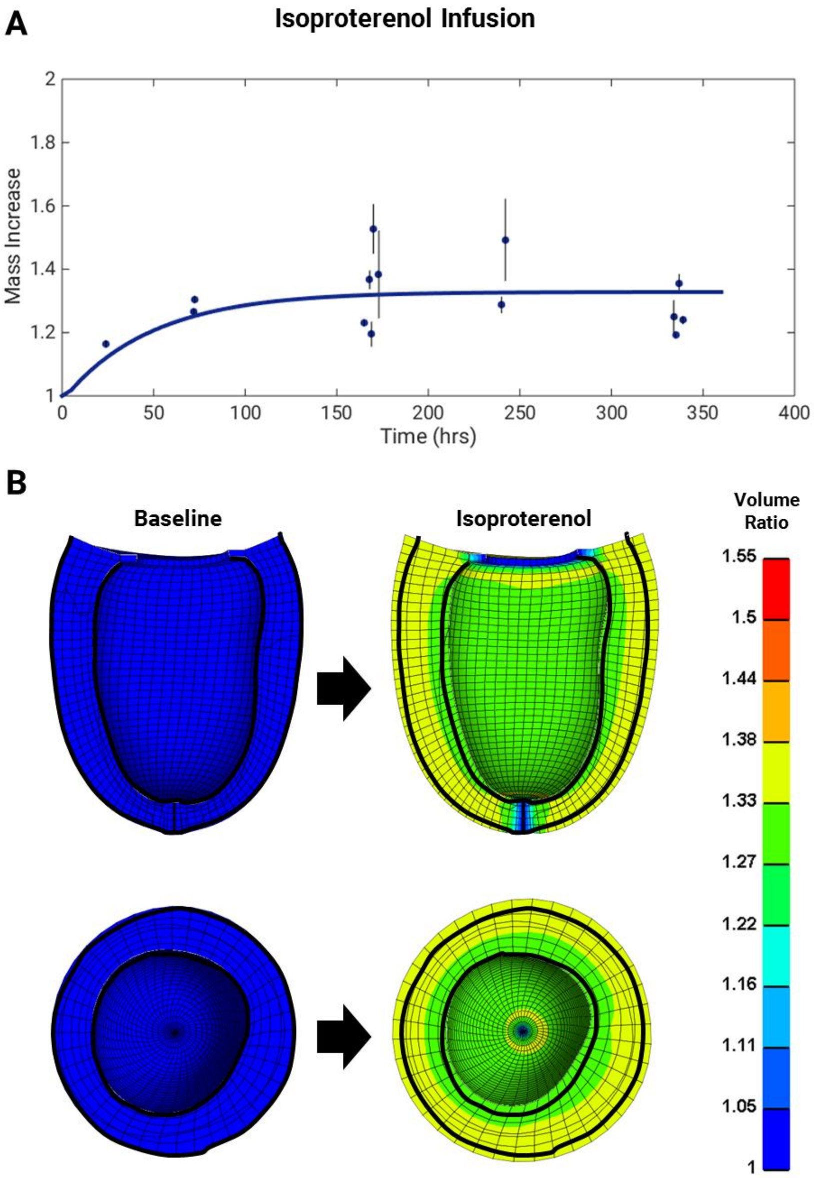

Figure 4. 4 Simulations of isoproterenol infusion for two weeks. A) The multiscale model predicts a growth time course consistent with experimental data of isoproterenol infusion in mice [32], [35], [44], [53], [36]–[43]. Data are shown as mass fold change ratio relative to control ± standard deviation of ratio. B) Finite-element model cross sections show volume ratios at end diastole for baseline (pre-growth) and after two weeks of isoproterenol infusion. Baseline outline is shown for clarity.

We simulated transverse aortic constriction in a similar fashion to isoproterenol infusion, except that the loading conditions correspond to an acute pressure overload, as calculated using a compartmental model of the heart and circulation [31]. The input levels of AngII, ET1, NE, ANPi, and BNPi were elevated to 0.09 for the duration of the simulation, while all other hormonal inputs were kept at their baseline levels. We first tested the consequences of our specific choice of stretch mapping by comparing the following set of simulations (Figure 4.5A): (a) TAC, with elevated hormones and a half-maximal initial network stretch input; (b) the network model alone, without mechanical coupling, using the maximum value within the functional range of the network stretch input but no elevated hormones; and (c) elevated stretch alone with mechanical coupling, using the maximum possible network stretch input (1) to capture the greatest mass increase without elevated hormones. The growth time course for each of these simulations (Figure 4.5B) showed that, despite starting with the maximum network stretch input, the stretch-only coupled model reached lower steady-state growth than TAC. Conversely, using the network alone to drive growth led to a greater amount of growth than TAC, demonstrating the effect of mechanical feedback within the multiscale model.

Figure 4.6A shows the mass increase in the left ventricle over two weeks in response to the combined mechanical and hormonal stimulation induced by TAC from both *in vivo* experiments and our multiscale model simulations. While there is substantial variability in the experimental data, our model predicts a 1.52 fold mass increase that falls near the average of the values reported in the literature [19], [23], [52], [35], [45]–[51]. Stimulation with mechanical overload alone and no elevated hormones, shown by the shaded range in Figure 4.6A, did not produce enough growth to capture the experimental data with the FEM-network mapping parameters and hormone levels employed in these simulations (see Discussion). The long-axis and short-axis cross-sections of the TAC model at end diastole (Figure 4.6B) show greater wall thickening than in the isoproterenol infusion model.

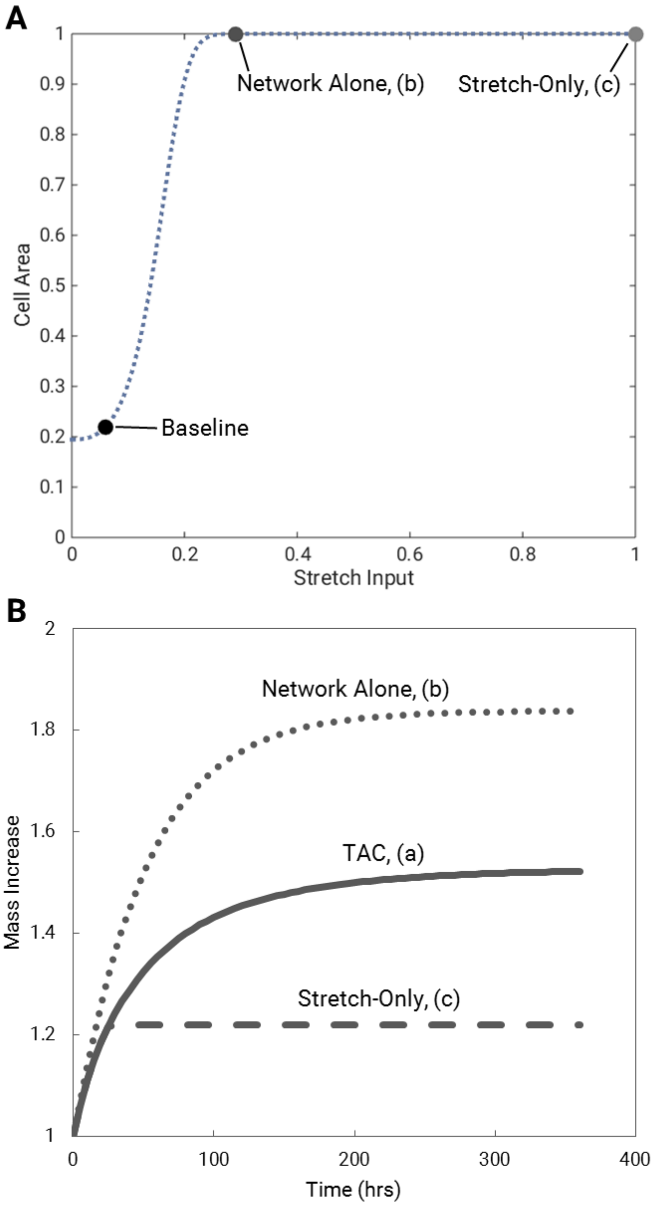

Figure 4.5 Testing the consequences of stretch mapping on growth. A) Relevant network stretch input values are shown on the cell area vs. stretch input steady-state curve. Baseline corresponds to the pre-growth state; (a) is the half-maximal input used to simulate TAC; (b) is the maximum value within the functional range of the network stretch input, used with the network model alone; and (c) is the maximum network stretch input (1), used in the coupled, stretch-only simulation. B) Time course of growth in the multiscale model for each simulation. Running the coupled model with stretch alone (dashed line) resulted in less growth than in TAC (solid line), despite the latter using a lower initial network stretch input. Driving growth using the network model only, on the other hand, led to greater amounts of growth than in TAC due to the lack of mechanical feedback in the model.

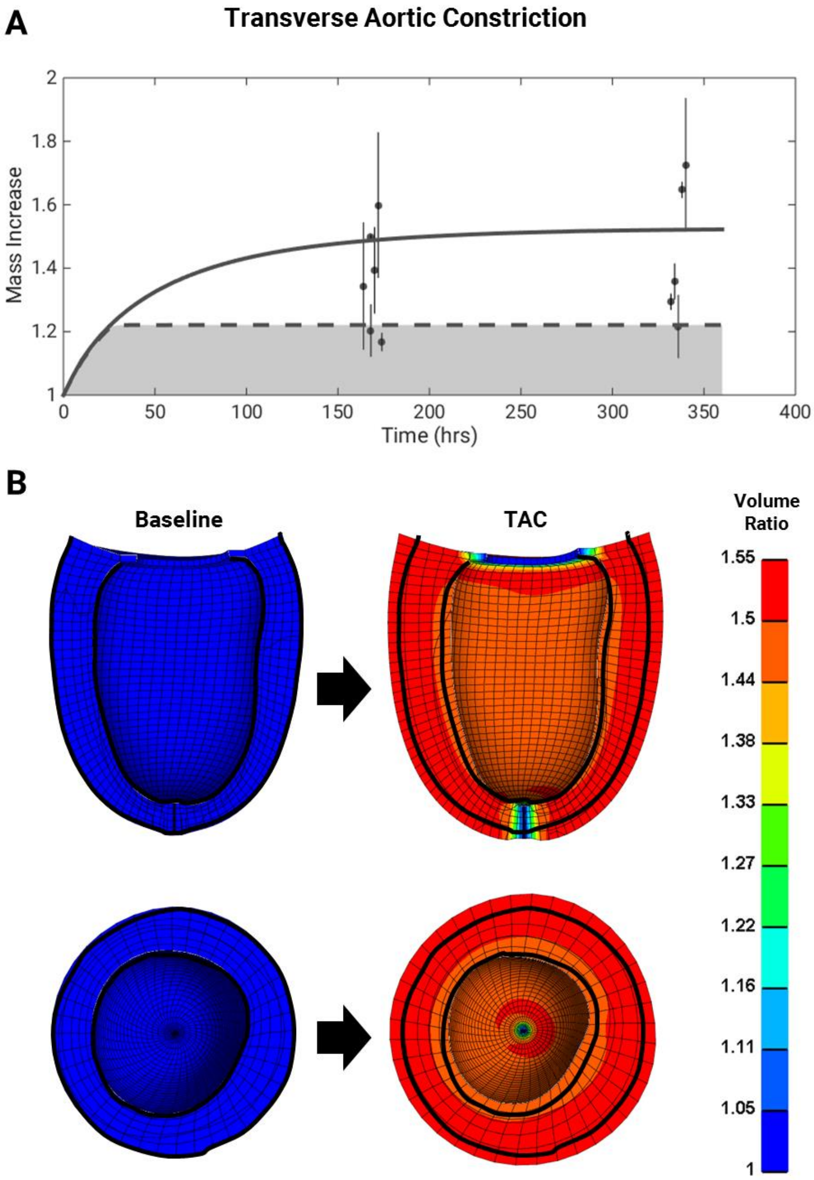

Figure 4.6 Simulations of transverse aortic constriction (TAC) for two weeks. A) When using both mechanical and hormonal stimulation (solid line), the multiscale model predicts a growth time course that follows experimental data trends of TAC in mice, from [19], [23], [52], [35], [45]–[51]. When stimulated using stretch alone, the multiscale model reaches a lower growth steady state than is seen in the TAC experimental data. The dashed line corresponds to the growth response obtained by stimulating the model with the maximum network stretch input (1), and the possible growth obtained when using the full range of network stretch inputs (0-1) is shown in the shaded region. Data are shown as mass fold change ratio relative to control ± standard deviation of ratio. B) Finite-element model cross sections show volume ratios at end diastole for baseline (pre-growth) and after two weeks of TAC. Baseline outline is shown for clarity.

Simulations of genetic and pharmacologic interventions for TAC

Finally, we simulated the effect of several interventions for attenuating the hypertrophy induced by TAC. We chose to simulate a transgenic Gq-coupled receptor inhibitor (GqI) overexpression model, an endogenous norepinephrine genetic KO (NE KO), an angiotensin receptor blocker (ARB), and a β-adrenergic receptor blocker (β-blocker). We ran each of the intervention models using the same mechanical loading conditions as TAC. As shown in Figure 4.7A-C, all interventions attenuated hypertrophy compared to TAC and to an extent that was broadly consistent with reported data [19], [45], [49]–[52]. After two weeks of growth, each intervention model had the following increases in mass: 1.07 fold for the GqI model; 1.16 fold for the NE KO model; 1.11 fold for the ARB model; and 1.40 for the β-blocker model. The difference in growth attenuation between each of the interventions can be attributed to the influence of each of the target nodes on the network. Removing activation of the Gαq11 node decreases the effect of the activation of inputs AngII, ET-1, and NE, while removing the NE node does not directly reduce the influence of the other hormonal inputs. Similarly, blocking the AT1R node prevents activation of JAK and Gαq11 by AngII. However, blocking the βAR node eliminates some but not all of the effect of NE activation, because NE also activates the αAR node, thus bypassing the block.

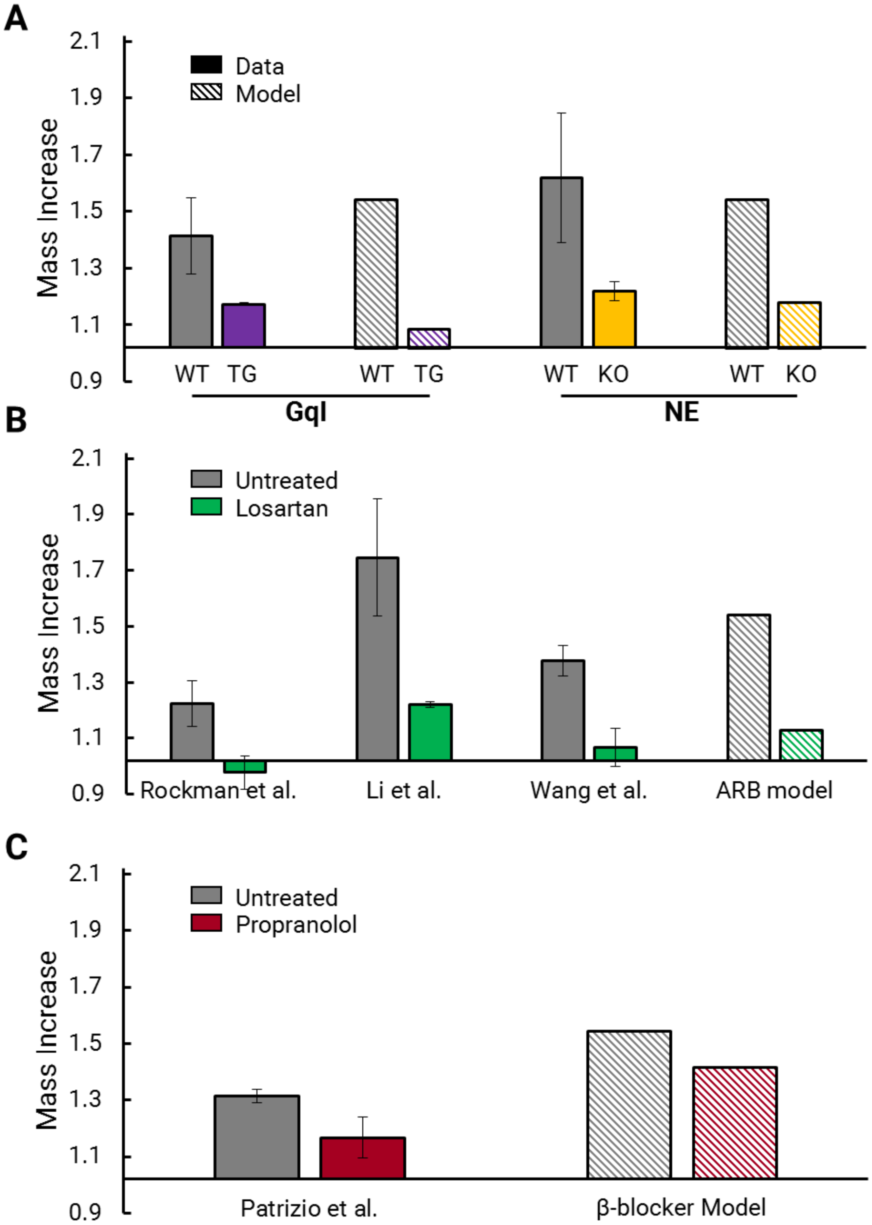

Figure 4.7 Simulations of transverse aortic constriction (TAC) interventions compared to experimental data. The multiscale model simulations of TAC interventions attenuate growth at two weeks in a manner consistent with experimental trends for A) genetic interventions GqI [45] and NE KO [19], B) ARB therapy [49]–[51] and C) β-blocker therapy [52], respectively. Data are shown as mass fold change ratio relative to control ± standard deviation of ratio.

DISCUSSION

We present here a multiscale model of cardiac hypertrophy that connects a detailed model of intracellular cardiomyocyte signaling with a finite-element model of organ-level mechanics. We simulated concentric growth due to isoproterenol infusion, transverse aortic constriction (TAC), and TAC plus genetic or pharmacologic intervention, and our model captured the experimental trends for all conditions reasonably well (Figures 4.4, 4.6, 4.7). The most striking finding from our study was that despite the fact that we attempted to simulate realistic levels of elevated stretch and hormonal stimulation associated with TAC, the hormonal inputs were responsible for the majority of the growth predicted by the multiscale model (Figure 4.6A).

In order to better understand this result, we explored the impact of each choice we made when constructing the model that could affect the relative impact of stretch vs. hormonal inputs. The most important choice was how to map variables such as stretch and circulating hormone levels into normalized (0-1) inputs in the signaling network model. We increased the level of several hormones as part of our simulation of TAC based on experimental data showing that they are elevated [1], [13], [22], [23], [14]–[21]. We chose to increase them to levels which would trigger a half-maximal hypertrophy response in the network model, based on data showing that even after TAC animals mount a significant additional hemodynamic response to agonists of some of these pathways [47]. We tested higher and lower levels of hormone activation but found that these activation levels failed to properly capture the growth attenuation of the TAC interventions considered here. If we wanted to more precisely match the intervention data shown here, or to match a wider array of experimental data, we could certainly tune each of the individual hormonal input levels further in our

TAC simulation, but given the high variability in the available experimental data on both hormone levels and growth following TAC, we did not feel that additional fine-tuning could be appropriately supported by data. With regard to stretch, we assumed that aortic constriction induced an initial stretch that – if maintained – would induce half-maximal hypertrophy, based on data showing that the TAC models used in most of the studies simulated here fell in the middle of the range of severities of TAC capable of induce graded hypertrophic responses [34]. However, due to the nature of the volumetric growth framework, as growth progressed, it reduced elastic stretches in the finite-element model, returning the stretch input transmitted to the network model to its baseline (homeostatic) value within the first 2-3 days of simulated time. To determine if this response depended on the specific choice of stretch mapping, we ran additional stretch-only simulations where aortic constriction induced the maximum possible network stretch input of 1 and found that this mapping only modestly increased the resulting growth. In Figure 4.6A, the shaded region of stretch-only simulations corresponds to the full range of possible network stretch inputs (0-1). As discussed further below, this aspect of the volumetric growth modeling approach may not be the best representation of the underlying biology, and the model could certainly be altered in various ways to prolong or accentuate the effects of mechanical stretch on growth. However, the fact that multiple interventions that disrupt hormonal signaling can nearly abolish TAC-induced hypertrophy experimentally (Figure 4.7) suggests that the balance between mechanically- and hormonally-driven hypertrophy in our multiscale model of TAC is reasonable.

Incorporating hormonal effects into a growth framework has significant advantages over using only a mechanically-driven phenomenologic growth law.

Our multiscale model separates the effects of mechanical overload from hormonal changes, and it uses a fundamentally different approach for predicting growth than traditional phenomenologic laws. In our model, the amount of growth that occurs depends on the signaling network intermediate nodes reaching new steady-state levels. In contrast, the phenomenologic laws drive growth based on the differences between a mechanical stimulus, such as stress or strain, and its homeostatic value, such that the growth will only increase until the homeostatic value is reached. Both approaches can be used to capture the growth due to an initial mechanical perturbation, such as pressure overload [24]–[26], [54], [55], and the phenomenologic laws can be parameterized to account for the elevated hormones. However, any subsequent changes to the hormone levels or addition of drugs would require re-fitting the phenomenologic laws. Accounting for hormones in addition to mechanics through their known signaling pathways extends the growth capabilities of the multiscale model. Incorporating hormonal and pharmacologic effects will likely be necessary for properly predicting cardiac hypertrophy in individual patients, who receive individualized drug regimens for their specific conditions. Additionally, our multiscale model may prove useful in identifying new therapeutic targets or intervention strategies for attenuating growth, be it for concentric hypertrophy more broadly or for patient-specific situations.

We simulated growth in our multiscale model using a volumetric growth framework. This choice assumes that the reference state for growth remains constant throughout the simulation and that the stress depends solely on the elastic deformation required to enforce compatibility in the entire grown material. In order to implement this framework in the multiscale model, we mapped the network cell area output – a single measure of mass increase – to the determinant of the growth deformation $\mathbf{F}_{\text{growth}}$, assuming that changes in cell area for the *in vivo* model correspond to changes in cell volume. However, other growth frameworks, such as the constrained mixture approach, could also be used to relate the predicted network hypertrophy to organ-level changes. Constrained mixture approaches implement growth via turnover of individual constituents within a single material, allowing for the reference state to evolve and accounting for differences in loading for each constituent [56]. The hypertrophy network model also outputs gene expression levels for specific proteins associated with sarcomere formation and contractile function: α-myosin heavy chain (aMHC) and β-myosin heavy chain (bMHC), which form the thick filaments of sarcomeres; sarcoplasmic reticulum ATPase (SERCA), a critical channel involved in calcium cycling; and skeletal α-actin (sACT), which contributes to thin filament formation. These outputs could be incorporated into a constrained mixture growth approach either directly or within a function that determines addition of new constituents.

While our multiscale model provides an exciting new method for predicting concentric growth, it currently has some limitations. First, the simulations included in this study assume spatially uniform concentric growth throughout the left ventricle. The multiscale model framework can be modified to incorporate different signaling networks with different signaling states for each individual finite element, but doing so would lead to substantially longer computation times. Second, the current network model cell area output can be interpreted as an increase in mass, but it does not account for directional differences in growth. Thus, the multiscale model presented here could not correctly capture both concentric growth as demonstrated here and eccentric growth patterns as observed during volume overload. More work is needed to understand the signaling events controlling myocyte shape and incorporate them into a multiscale model that can account for both thickening and lengthening of muscle fibers. Lastly, the model presented here mixes information across species: mechanical loading was simulated using an average canine left ventricle, the network model was constructed primarily from data on cultured neonatal rat ventricular myocytes, and comparison data comes from mouse experiments. While subsequent versions of the model could use a finite-element model based on a mouse left ventricle, the results from this study show that hormones are more important in reproducing observed growth following TAC than mechanics, indicating that the exact choice of geometry is probably not critical for matching qualitative trends such as whether an intervention will attenuate or accentuate hypertrophy. In spite of these limitations, our multiscale model demonstrates a promising strategy for predicting cardiac hypertrophy by integrating mechanics and biology.

REFERENCES

[1] B. H. Lorell and B. A. Carabello, "Left Ventricular Hypertrophy," *Circulation*, vol. 102, no. 4, pp. 470–479, Jul. 2000.

[2] W. Grossman, D. Jones, and L. P. McLaurin, "Wall stress and patterns of hypertrophy in the human left ventricle," *J. Clin. Invest.*, vol. 56, no. 1, pp. 56–64, 1975.

[3] E. J. Benjamin *et al.*, *Heart Disease and Stroke Statistics—2018 Update: A Report From the American Heart Association*. 2018.

[4] R. M. Bruno and S. Taddei, "Renal denervation and regression of left ventricular hypertrophy," *Eur. Heart J.*, vol. 35, no. 33, pp. 2205–2207, Sep. 2014.

[5] C. Cuspidi, A. Vaccarella, F. Negri, and C. Sala, "Resistant hypertension and left ventricular hypertrophy: an overview," *J. Am. Soc. Hypertens.*, vol. 4, no. 6, pp. 319–324, Nov. 2010.

[6] N. Kawel-Boehm *et al.*, "Left ventricular mass at MRI and long-term risk of cardiovascular events: The Multi-Ethnic Study of Atherosclerosis (MESA)," *Radiology*, vol. 293, no. 1, pp. 107–114, 2019.

[7] E. S. Monrad, O. M. Hess, T. Murakami, H. Nonogi, W. J. Corin, and H. P. Krayenbuehl, "Time course of regression of left ventricular hypertrophy after aortic valve replacement.," *Circulation*, vol. 77, no. 6, pp. 1345–55, Jun. 1988.

[8] S. Gelsomino *et al.*, "Time course of left ventricular remodeling after stentless aortic valve replacement," *Am. Heart J.*, vol. 142, no. 3, pp. 556–562, 2001.

[9] C. M. Otto, "Valvular Aortic Stenosis. Disease Severity and Timing of Intervention," *J. Am. Coll. Cardiol.*, vol. 47, no. 11, pp. 2141–2151, 2006.

[10] R. A. Nishimura *et al.*, "2014 AHA/ACC guideline for the management of patients with valvular heart disease: Executive summary: A report of the American college of cardiology/American heart association task force on practice guidelines," *J. Am. Coll. Cardiol.*, vol. 63, no. 22, pp. 2438–2488, 2014.

[11] Y. K. Xiang, "Compartmentalization of β-adrenergic signals in cardiomyocytes," *Circ. Res.*, vol. 109, no. 2, pp. 231–244, 2011.

[12] M. W. Szymanski and D. P. Singh, *Isoproterenol*. StatPearls Publishing, 2019.

[13] B. Swynghedauw, “Molecular mechanisms of myocardial remodeling,” *Physiol. Rev.*, vol. 79, no. 1, pp. 215–262, 1999.

[14] T. Yamazaki *et al.*, “Angiotensin II Partly Mediates Mechanical Stress–Induced Cardiac Hypertrophy,” *Circ. Res.*, vol. 77, no. 2, pp. 258–265, Aug. 1995.

[15] T. Yamazaki *et al.*, “Endothelin-1 is involved in mechanical stress-induced cardiomyocyte hypertrophy,” *J. Biol. Chem.*, vol. 271, no. 6, pp. 3221–3228, 1996.

[16] H. Schunkert, V. J. Dzau, S. S. Tang, A. T. Hirsch, C. S. Apstein, and B. H. Lorell, “Increased rat cardiac angiotensin converting enzyme activity and mRNA expression in pressure overload left ventricular hypertrophy: Effects on coronary resistance, contractility, and relaxation,” *J. Clin. Invest.*, vol. 86, no. 6, pp. 1913–1920, 1990.

[17] P. H. Sugden, “Signaling in myocardial hypertrophy: Life after calcineurin?,” *Circ. Res.*, vol. 84, no. 6, pp. 633–646, 1999.

[18] S. Izumo, B. Nadal-Ginard, and V. Mahdavi, “Protooncogene induction and reprogramming of cardiac gene expression produced by pressure overload.,” *Proc. Natl. Acad. Sci. U. S. A.*, vol. 85, no. 2, pp. 339–343, 1988.

[19] A. Rapacciuolo, G. Esposito, K. Caron, L. Mao, S. A. Thomas, and H. A. Rockman, “Important role of endogenous norepinephrine and epinephrine in the development of in vivo pressure-overload cardiac hypertrophy,” *J. Am. Coll. Cardiol.*, vol. 38, no. 3, pp. 876–882, 2001.

[20] K. Lindpaintner, D. D. Lund, and P. G. Schmid, “Effects of chronic progressive myocardial hypertrophy on indexes of cardiac autonomic innervation,” *Circ. Res.*, vol. 61, no. 1, pp. 55–62, 1987.

[21] Y. Yoshida *et al.*, “Journal of Molecular and Cellular Cardiology p53-Induced in fl ammation exacerbates cardiac dysfunction during pressure overload,” vol. 85, pp. 183–198, 2015.

[22] F. A. Kamal *et al.*, “Simultaneous adrenal and cardiac g-protein-coupled receptor-gβγ inhibition halts heart failure progression,” *J. Am. Coll. Cardiol.*, vol. 63, no. 23, pp. 2549–2557, 2014.

[23] Y. Liao *et al.*, “Activation of Adenosine A1 Receptor Attenuates Cardiac Hypertrophy and Prevents Heart Failure in Murine Left Ventricular Pressure-Overload Model,” *Circ. Res.*, vol. 93, no. 8, pp. 759–766, 2003.

[24] R. C. P. Kerckhoffs, J. H. Omens, and A. D. McCulloch, “A single strain-

based growth law predicts concentric and eccentric cardiac growth during pressure and volume overload," *Mech. Res. Commun.*, vol. 42, pp. 40–50, 2012.

[25] L. A. Taber, "Biomechanical growth laws for muscle tissue," *J. Theor. Biol.*, 1998.

[26] T. Arts, T. Delhaas, P. Bovendeerd, X. Verbeek, and F. W. Prinzen, "Adaptation to mechanical load determines shape and properties of heart and circulation: The CircAdapt model," *Am. J. Physiol. - Hear. Circ. Physiol.*, vol. 288, no. 4 57-4, Apr. 2005.

[27] K. A. Ryall, D. O. Holland, K. A. Delaney, M. J. Kraeutler, A. J. Parker, and J. J. Saucerman, "Network reconstruction and systems analysis of cardiac myocyte hypertrophy signaling.," *J. Biol. Chem.*, vol. 287, no. 50, pp. 42259–68, Dec. 2012.

[28] D. U. Frank, M. D. Sutcliffe, and J. J. Saucerman, "Network-based predictions of in vivo cardiac hypertrophy," *J. Mol. Cell. Cardiol.*, vol. 121, pp. 180–189, Aug. 2018.

[29] A. C. Estrada, K. Yoshida, S. A. Clarke, and J. W. Holmes, "Longitudinal Reinforcement of Acute Myocardial Infarcts Improves Function by Transmurally Redistributing Stretch and Stress," *J. Biomech. Eng.*, vol. 142, no. 2, Feb. 2020.

[30] S. A. Clarke, N. C. Goodman, G. Ailawadi, and J. W. Holmes, "Effect of Scar Compaction on the Therapeutic Efficacy of Anisotropic Reinforcement Following Myocardial Infarction in the Dog," *J. Cardiovasc. Transl. Res.*, vol. 8, no. 6, pp. 353–361, 2015.

[31] C. M. Witzenburg and J. W. Holmes, "Predicting the time course of ventricular dilation and thickening using a rapid compartmental model," *J. Cardiovasc. Transl. Res.*, vol. 11, no. 2, pp. 109–122, 2018.

[32] M. A. Allwood *et al.*, "Heme oxygenase-1 overexpression exacerbates heart failure with aging and pressure overload but is protective against isoproterenol-induced cardiomyopathy in mice.," *Cardiovasc. Pathol.*, vol. 23, no. 4, pp. 231–7, Jul. 2014.

[33] E. K. Rodriguez, a Hoger, and a D. McCulloch, "Stress-dependent finite-growth in soft elastic tissues," *J. Biomech.*, vol. 27, no. 4, pp. 455–467, 1994.

[34] D. A. Richards *et al.*, "Distinct Phenotypes Induced by Three Degrees of Transverse Aortic Constriction in Mice," *Sci. Rep.*, vol. 9, no. 1, pp. 1–15, Dec. 2019.

[35] L. J. De Windt *et al.*, “Targeted inhibition of calcineurin attenuates cardiac hypertrophy in vivo,” *Proc. Natl. Acad. Sci.*, vol. 98, no. 6, pp. 3322–3327, 2001.

[36] N. Tuerdi *et al.*, “Preventive effects of simvastatin nanoliposome on isoproterenol-induced cardiac remodeling in mice.,” *Nanomedicine*, vol. 12, no. 7, pp. 1899–1907, Oct. 2016.

[37] C. C. Sucharov, J. G. Hijmans, R. D. Sobus, W. F. A. Melhado, S. D. Miyamoto, and B. L. Stauffer, “β-Adrenergic receptor antagonism in mice: a model for pediatric heart disease.,” *J. Appl. Physiol.*, vol. 115, no. 7, pp. 979–87, Oct. 2013.

[38] O. Drews, O. Tsukamoto, D. Liem, J. Streicher, Y. Wang, and P. Ping, “Differential regulation of proteasome function in isoproterenol-induced cardiac hypertrophy.,” *Circ. Res.*, vol. 107, no. 9, pp. 1094–101, Oct. 2010.

[39] S. Tshori *et al.*, “Transcription factor MITF regulates cardiac growth and hypertrophy.,” *J. Clin. Invest.*, vol. 116, no. 10, pp. 2673–81, Oct. 2006.

[40] Y. Zhang *et al.*, “Hydrogen (H2) Inhibits Isoproterenol-Induced Cardiac Hypertrophy via Antioxidative Pathways,” *Front. Pharmacol.*, vol. 7, p. 392, Oct. 2016.

[41] S. B. Waters, D. M. Diak, M. Zuckermann, P. H. Goldspink, L. Leoni, and B. B. Roman, “Genetic background influences adaptation to cardiac hypertrophy and Ca2+ handling gene expression,” *Front. Physiol.*, vol. 4, p. 11, 2013.

[42] Y. Ryu *et al.*, “Gallic acid prevents isoproterenol-induced cardiac hypertrophy and fibrosis through regulation of JNK2 signaling and Smad3 binding activity.,” *Sci. Rep.*, vol. 6, no. 1, p. 34790, Dec. 2016.

[43] E. J. Jaehnig, A. B. Heidt, S. B. Greene, I. Cornelissen, and B. L. Black, “Increased susceptibility to isoproterenol-induced cardiac hypertrophy and impaired weight gain in mice lacking the histidine-rich calcium-binding protein.,” *Mol. Cell. Biol.*, vol. 26, no. 24, pp. 9315–26, Dec. 2006.

[44] C. L. Galindo *et al.*, “Transcriptional profile of isoproterenol-induced cardiomyopathy and comparison to exercise-induced cardiac hypertrophy and human cardiac failure.,” *BMC Physiol.*, vol. 9, no. 1, p. 23, Dec. 2009.

[45] S. A. Akhter, L. M. Luttrell, H. A. Rockman, G. Iaccarino, R. J. Lefkowitz, and W. J. Koch, “Targeting the receptor-G(q) interface to inhibit in vivo pressure overload myocardial hypertrophy,” *Science (80-.).*, vol. 280, no. 5363, pp. 574–577, 1998.

[46] J. M. Huss *et al.*, “The Nuclear Receptor ERRα Is Required for the Bioenergetic and Functional Adaptation to Cardiac Pressure Overload,” *Cell Metab.*, vol. 6, no. 1, pp. 25–37, 2007.

[47] D. J. Choi, W. J. Koch, J. J. Hunter, and H. A. Rockman, “Mechanism of β-adrenergic receptor desensitization in cardiac hypertrophy is increased β-adrenergic receptor kinase,” *J. Biol. Chem.*, vol. 272, no. 27, pp. 17223–17229, 1997.

[48] H. Ling *et al.*, “Requirement for Ca2+/calmodulin-dependent kinase II in the transition from pressure overload-induced cardiac hypertrophy to heart failure in mice,” *J. Clin. Invest.*, vol. 119, no. 5, pp. 1230–1240, 2009.

[49] H. A. Rockman, S. P. Wachhorst, L. Mao, and J. Ross, “ANG II receptor blockade prevents ventricular hypertrophy and ANF gene expression with pressure overload in mice.,” *Am. J. Physiol.*, vol. 266, no. 6 Pt 2, pp. H2468-75, Jun. 1994.

[50] L. Li *et al.*, “Comparison of angiotensin II type 1-receptor blockers to regress pressure overload-induced cardiac hypertrophy in mice,” *Hypertens. Res.*, vol. 33, no. 12, pp. 1289–1297, Dec. 2010.

[51] X. Wang *et al.*, “The effects of different angiotensin II type 1 receptor blockers on the regulation of the ACE-AngII-AT1 and ACE2-Ang(1–7)-Mas axes in pressure overload-induced cardiac remodeling in male mice,” *J. Mol. Cell. Cardiol.*, vol. 97, pp. 180–190, Aug. 2016.

[52] M. Patrizio *et al.*, “Propranolol causes a paradoxical enhancement of cardiomyocyte foetal gene response to hypertrophic stimuli,” *Br. J. Pharmacol.*, vol. 152, no. 2, pp. 216–222, 2007.

[53] W. W. Brooks and C. H. Conrad, “Isoproterenol-induced myocardial injury and diastolic dysfunction in mice: structural and functional correlates.,” *Comp. Med.*, vol. 59, no. 4, pp. 339–43, Aug. 2009.

[54] I. E. Lin and L. a Taber, “A model for stress-induced growth in the developing heart.,” *J. Biomech. Eng.*, vol. 117, no. 3, pp. 343–349, 1995.

[55] S. Göktepe, O. J. Abilez, K. K. Parker, and E. Kuhl, “A multiscale model for eccentric and concentric cardiac growth through sarcomerogenesis,” *J. Theor. Biol.*, vol. 265, no. 3, pp. 433–442, 2010.

[56] J. D. Humphrey and K. R. Rajagopal, “A constrained mixture model for growth and remodeling in soft tissues,” *Math. Model. Methods Appl. Sci.*, vol. 12, no. 3, pp. 407–430, 2002.

CHAPTER 5:

FUTURE DIRECTIONS IN COMPUTATIONAL MODELING OF CARDIAC HYPERTROPHY, INJURY, AND THERAPY

NEW COMPUTATIONAL MODELS OF CARDIAC HYPERTROPHY

In this dissertation, we introduced computational models of the heart in the settings of injury and therapy. In Chapter 3, we used a finite-element model to understand how local anisotropic reinforcement of an infarct can lead to acute improvements in function. Then, in Chapter 4, we built a multiscale model of cardiac hypertrophy to predict the time course of concentric hypertrophy due to changes in hormones and mechanics, and then used it to simulate how different genetic and pharmacologic interventions can attenuate this hypertrophy. Both of these are useful applications of computational modeling, but their use can be extended to other conditions and therapies.

Models of chronic post-MI mechanical reinforcement

A first extension to the models shown here is building a finite-element model of chronic patch reinforcement. This model can start from the finite-element model presented in Chapter 3, but with a few key modifications. First, the surviving myocardium would use the growth plugin to simulate hypertrophy, and a phenomenologic growth law could be used to predict the amount of hypertrophy. The growth could also be driven by the hypertrophy network model, although the additional requirements for this model are described in a subsequent section. Such a model will also require incorporating scar shrinkage, as this is an important aspect of healing [1], [2] and is the primary reason for the failure of the patch in chronic experiments [2]. Lastly, connecting the model to a simulated circulation will allow us to account for changes in hemodynamic compensation following infarction, similar to the approach taken by Witzenburg et al. [3] using a fast compartmental model. Using these modifications, the model should be able to predict post-MI hypertrophy in the absence of interventions and with mechanical reinforcement. This new model can allow us to test a full range of reinforcement directions and optimize the patch configuration that best attenuates post-MI eccentric hypertrophy. Alternatively, we can also use the model to understand at which point during scar shrinking the patch loses tension and effectiveness.

A second application of the post-MI hypertrophy model is using it to understand how different reinforcement methods alter hypertrophy. As discussed in Chapters 1 and 3, a variety of mechanical reinforcement methods have been developed to slow down or prevent post-MI hypertrophy. Global reinforcement methods effectively limit hypertrophy by physically limiting expansion of the heart, but they do so at the cost of impaired filling. We can use our new computational model to better understand the tradeoff between limiting hypertrophy and restricting filling in global reinforcement. By using a strain-based law and an end-diastolic stretch stimulus, we can first model the hypertrophy seen experimentally and then test if varying the stiffness of the global reinforcement method can balance the positive and negative effects of these methods.

In contrast to global restraint, local reinforcement methods have had mixed results regarding their effectiveness in functional improvement and reduction of hypertrophy. Local reinforcement methods vary in their strategies – we’ve shown anisotropic reinforcement with a stiff patch, but we can also model injection of hydrogels, as shown by Wenk et al. [4], and flexible meshes to understand how these different methods alter mechanics post-MI. We can then use the chronic post-MI model to predict the hypertrophy that occurs with different local reinforcement methods and then use these results to understand how local changes in mechanics in the remote region lead to differences in eccentric hypertrophy. By comparing the local reinforcement results to those of global methods, we can begin to design a reinforcement strategy that optimizes reduction in hypertrophy and improvements in function.

Multiscale models of eccentric hypertrophy

The multiscale model of hypertrophy presented in Chapter 4 predicts concentric hypertrophy induced by changes in both mechanics and hormones. The model assumes that increases in cell area from the network model correspond to increases in cell volume and fiber thickening. However, in order to simulate conditions that induce eccentric hypertrophy, such as volume overload or MI, we need a different method of interpreting changes in the network cell area. Currently, the cell area accounts for changes in mass but offers no directional information; additionally, a single stretch input cannot directly account for mechanical stimuli in different directions. We need to develop a function that determines the direction of growth given particular mechanical stimuli but with the amount of mass increase defined by the network cell area. For example, the directionality function could use the difference or the ratio between the end-diastolic strain and the end-systolic strain to determine lengthening versus thickening of the fibers. However, determining which mechanical feature corresponds to the network stretch input remains a challenge with this approach. Another strategy would be to expand the network model and incorporate the directional information directly, but this approach depends on the availability of directional hypertrophy data in cardiomyocytes [5], [6]. The multiscale model with a directionality function can be validated against pressure overload data from transverse aortic constriction and aortic stenosis for concentric hypertrophy, as done in Chapter 4, and then against volume overload data from mitral regurgitation studies for eccentric hypertrophy.

Once validated against both pressure overload and volume overload, a new multiscale model of hypertrophy could be used to predict the time course of post-MI growth and the effect of different therapies, similar to what was proposed for the chronic reinforcement model in the previous section. This model would also incorporate scar shrinkage and coupling to the circulation, but the growth would be driven by the network rather than by a phenomenologic growth law. While both of these hypertrophy models would be tuned to experimental data, the contribution of mechanics to growth in the multiscale model would provide insight into the inherent differences between these methods of growth modeling. The biggest advantage of the multiscale model is the ability to incorporate the effect of hormones and drugs, so we could test the effect of beta-blockers and ACE-inhibitors on the development of hypertrophy post-MI. Finally, this model of pharmacologic intervention post-MI can be applied to the case of chronic mechanical reinforcement, better predicting how these therapies would attenuate hypertrophy in a clinical setting and in a more patient-specific manner.

Modeling the contribution of metabolism to hypertrophy

At the core of cardiac diseases, particularly MI and heart failure, is a change in organ- and cell-level energetics. Pressure-volume behavior is a measure of cardiac work and oxygen consumption [7], [8], and it is affected by ischemia, loading, and hypertrophy. Increases in contractility help compensate for changes in loading but require higher ATP consumption and more oxygen and nutrients for cardiomyocytes. Injury to the heart, such as infarction and ischemia-reperfusion, induce damaging changes to cardiomyocyte energetics [9]. Numerous experimental studies have shown that altered cardiac metabolism contributes to the development of heart failure – the heart essentially runs out of fuel and begins to fail [10]–[13]. Other studies have also shown that altered metabolism is seen in hypertrophied hearts [14], [15]. Some computational models of hypertrophy have incorporated metabolic changes [16], [17], but additional work can be done to use metabolic data as a driver of hypertrophy and heart failure.

Multiscale computational models of hypertrophy can be built to better understand how changes in metabolism can induce growth. These models can use oxygen consumption changes and mechanical work at the organ level either to directly stimulate growth or to inform the necessary adaptations in cell-level energetics that lead to increases in mass. Network model outputs like gene expression of sarcomere proteins can be used to account for the changes in contractility and oxygen demand, but ideally a model of metabolism at the mitochondrial level will be incorporated to account for changes in oxidative phosphorylation. Using the mitochondrial model, changes in metabolism from switching between fatty acid oxidation and glycolysis, as seen in HF, can be incorporated, and the effect of using different fatty acids or carbon sources can serve as an additional method of understanding the underlying development of hypertrophy. This new multiscale model can also be applied to better understanding non-pathologic hypertrophy in endurance athletes and the impact of obesity and diabetes on cardiac function [18], [19]. Finally, the metabolic multiscale model of hypertrophy can then be used to identify new therapeutic targets or strategies that directly affect metabolic effects, further increasing the available strategies for treating hypertrophy in cardiovascular disease.

CONCLUSION

As shown in this dissertation, computational models are a versatile tool for understanding cardiac function and hypertrophy and for developing therapeutic strategies in cardiovascular disease. While this dissertation presented two specific applications of computational models and other groups have shown their use for a variety of conditions, these models continue to have great potential and will only continue to become more useful in the field of cardiac biomechanics.

REFERENCES

[1] W. J. Richardson and J. W. Holmes, “Why Is Infarct Expansion Such an Elusive Therapeutic Target?,” *Journal of Cardiovascular Translational Research*, vol. 8, no. 7. Springer New York LLC, pp. 421–430, 21-Sep-2015.

[2] S. A. Clarke, N. C. Goodman, G. Ailawadi, and J. W. Holmes, “Effect of Scar Compaction on the Therapeutic Efficacy of Anisotropic Reinforcement Following Myocardial Infarction in the Dog,” *J. Cardiovasc. Transl. Res.*, vol. 8, no. 6, pp. 353–361, 2015.

[3] C. M. Witzenburg and J. W. Holmes, “Predicting the time course of ventricular dilation and thickening using a rapid compartmental model,” *J. Cardiovasc. Transl. Res.*, vol. 11, no. 2, pp. 109–122, 2018.

[4] J. F. Wenk *et al.*, “Regional Left Ventricular Myocardial Contractility and Stress in a Finite Element Model of Posterobasal Myocardial Infarction,” *J. Biomech. Eng.*, vol. 133, no. 4, p. 044501, Apr. 2011.

[5] I. Kehat and J. D. Molkentin, “Molecular pathways underlying cardiac remodeling during pathophysiological stimulation,” *Circulation*, vol. 122, no. 25, pp. 2727–2735, Dec. 2010.

[6] R. L. Nicol, N. Frey, G. Pearson, M. Cobb, J. Richardson, and E. N. Olson, “Activated MEK5 induces serial assembly of sarcomeres and eccentric cardiac hypertrophy,” *EMBO J.*, vol. 20, no. 11, pp. 2757–2767, Jun. 2001.

[7] H. Suga, “Total mechanical energy of a ventricle model and cardiac oxygen consumption.,” *Am. J. Physiol.*, vol. 236, no. 3, Mar. 1979.

[8] F. Khalafbeigui, H. Suga, and K. Sagawa, “Left ventricular systolic pressure-volume area correlates with oxygen consumption.,” *Am. J. Physiol.*, vol. 237, no. 5, pp. H566-9, Nov. 1979.

[9] A. Frank, M. Bonney, S. Bonney, L. Weitzel, M. Koeppen, and T. Eckle, “Myocardial ischemia reperfusion injury: from basic science to clinical bedside.,” *Semin. Cardiothorac. Vasc. Anesth.*, vol. 16, no. 3, pp. 123–32, Sep. 2012.

[10] H. Ardehali *et al.*, “Targeting myocardial substrate metabolism in heart failure: potential for new therapies,” *Eur. J. Heart Fail.*, vol. 14, no. 2, pp. 120–129, Feb. 2012.

[11] S. Neubauer, “The Failing Heart — An Engine Out of Fuel,” *N. Engl. J. Med.*, vol. 356, no. 11, pp. 1140–1151, Mar. 2007.

[12] R. Ventura-Clapier, A. Garnier, V. Veksler, and F. Joubert, “Bioenergetics of the failing heart,” *Biochim. Biophys. Acta - Mol. Cell Res.*, vol. 1813, no. 7, pp. 1360–1372, Jul. 2011.

[13] J. S. Ingwall, “Energy metabolism in heart failure and remodelling,” *Cardiovasc. Res.*, vol. 81, no. 3, pp. 412–419, Oct. 2008.

[14] S. Rimbaud *et al.*, “Stimulus specific changes of energy metabolism in hypertrophied heart,” *J. Mol. Cell. Cardiol.*, vol. 46, no. 6, pp. 952–959, Jun. 2009.

[15] N. Sambandam, G. D. Lopaschuk, R. W. Brownsey, and M. F. Allard, “Energy metabolism in the hypertrophied heart,” *Heart Failure Reviews*, vol. 7, no. 2. pp. 161–173, 2002.

[16] S. G. Tewari, S. M. Bugenhagen, K. C. Vinnakota, J. J. Rice, P. M. L. Janssen, and D. A. Beard, “Influence of metabolic dysfunction on cardiac mechanics in decompensated hypertrophy and heart failure,” *J. Mol. Cell. Cardiol.*, vol. 94, pp. 162–175, May 2016.

[17] F. Wu, J. Zhang, and D. A. Beard, “Experimentally observed phenomena on cardiac energetics in heart failure emerge from simulations of cardiac metabolism,” *Proc. Natl. Acad. Sci.*, vol. 106, no. 17, pp. 7143–7148, Apr. 2009.

[18] G. D. Lopaschuk, J. R. Ussher, C. D. L. Folmes, J. S. Jaswal, and W. C. Stanley, “Myocardial fatty acid metabolism in health and disease,” *Physiological Reviews*, vol. 90, no. 1. pp. 207–258, 2010.

[19] N. Fillmore, C. S. Wagg, L. Zhang, A. Fukushima, and G. D. Lopaschuk, “Cardiac branched-chain amino acid oxidation is reduced during insulin resistance in the heart,” *Am. J. Physiol. Metab.*, vol. 315, no. 5, pp. E1046–E1052, Nov. 2018.